INVESTIGATION OF ROBOTIC FACE GRINDING PROCESS

A Dissertation
Presented to
The Academic Faculty

by

KEDAR JOSHI

In Partial Fulfillment
of the Requirements for the Degree
Master of Science in the
School of Mechanical Engineering

Georgia Institute of Technology
August 2019

INVESTIGATION OF ROBOTIC FACE GRINDING PROCESS

Approved by:

Dr. Shreyes Melkote, Advisor
School of Mechanical Engineering
Georgia Institute of Technology

Dr. Steven Liang
School of Mechanical Engineering
Georgia Institute of Technology

Mr. Rahul Chaudhuri
Sr. Manager, R&D
The Timken Company

Date Approved: [July 18, 2019]

ACKNOWLEDGEMENTS

I would like to greatly thank the students and faculty of the PMRC for help with their support. I would like to thank greatly Steven Sheffield and Nathan Mauldin for their aid in fabricating parts. In addition, I would like to thank Kyle French, Anh Nguyen, and Andrew Keller of the ME Electronics shop for their electrical expertise. I would like to thank The Timken Company for providing feedback and funding for this project. I would like to thank Dr. Melkote for his guidance as an advisor. I would also like to thank Dr. Liang and Rahul Chaudhari (R&D Manager, Timken) for their time to be on my committee. I would like to thank my family and many friends for making sure I never forget the value of being a good person.

TABLE OF CONTENTS

LIST OF TABLES

LIST OF FIGURES

NOMENCLATURE

X, Y, Z	Coordinate frame attached to the robot end-effector
X_G, Y_G, Z_G	Coordinate frame attached to the robot base (global)
X_g, Y_g, Z_g	Coordinate frame attached to the robot flexible gripper
A	Bearing ring annular face area
a_i	Length of i^{th} link of the robot manipulator (DH parameter)
α_i	Twist of i^{th} link of the robot manipulator (DH parameter)
C	Cartesian compliance at the robot end-effector
d_x	Input displacement to the ring in X_g-direction (FEM simulation)
d_y	Input displacement to the ring in Y_g-direction (FEM simulation)
d_z	Input displacement to the ring in Z_g-direction (FEM simulation)
f	Robot infeed rate
F_n	Normal grinding force
G_r	Grinding wheel wear
h_1, h_2	Gripper design dimensions
$H(\omega)$	Robotic system transfer function
J	Kinematic Jacobian transform matrix
K_θ	Robot joint torsional stiffness
K_1, K_2, K_{eq}	Robot Cartesian stiffness, Gripper stiffness and Equivalent system stiffness
K_R	Cartesian robot stiffness
K_g	Grinding stiffness
MRR	Material removal rate
λ_w	Material removal parameter

R^2	Coefficient of determination
S_a, S_q, S_z	Surface roughness parameters
τ	System time constant
t_1	Time instant at which the feed is stopped (Robot grinding process cycle)
U_1	Robot infeed rate
v_s	Grinding wheel speed
x_{act}, x_{com}	Actual and commanded robot static displacement
$\dot{x}_{act}$	Actual robot infeed rate
Δr	Width of ring to be ground
T	Total grinding cycle time

SUMMARY

The production of bearing rings involves face grinding of the ring faces on highly specialized and dedicated precision grinding machines. While such machines are ideal for high volume production of precision bearings, the associated capital cost and setup times are high, and the machines cannot be easily reconfigured for other applications. In contrast, articulated arm robots (6-axis) are less expensive, have high reliability and reduced work space requirement compared to bulky grinding machines, and they can be readily reconfigured for a variety of production tasks. Although robots are widely used in industry for operations such as welding, painting, and deburring, their use in high precision material removal processes is comparatively limited. The compliance of such robots poses a challenge in high precision operations. This thesis addresses the feasibility of robotic face grinding of hardened steel rings through experiments designed to understand the effects of robot compliance on the face grinding process cycle time and part quality. An experimental setup for the robotic face grinding was built using a 6-axis articulated arm manipulator. The vibration characteristics of the robot were studied to identify the natural resonant modes through modal impact hammer tests. The effect of robot compliance on the grinding process cycle time was studied through experiments and process modeling. In addition, a novel flexible gripper was designed to compensate for part-wheel misalignment and vibration induced part quality errors. Experimental evaluation of the optimized flexible gripper showed that part quality errors arising from part-wheel misalignment and vibrations were significantly reduced. In order to identify the robot configuration that can yield the lowest grinding cycle time, the robot posture optimization study was conducted to

understand the effect of robot pose on the Cartesian stiffness at the end-effector and to identify the robot pose that yields the highest Cartesian stiffness.

CHAPTER 1. INTRODUCTION

1.1 Introduction and Problem Statement

The production of inner and outer bearing rings involves face grinding of the ring faces on highly specialized and dedicated precision grinding machines. While such machines are ideal for high volume production of precision bearings, the associated capital cost and setup times are high, and the machines cannot be easily reconfigured for other applications [2]. In contrast, robots – Cartesian or 6-axis articulated arm type – are considerably less expensive, have high reliability and reduced work space requirement, and can be readily reconfigured for a variety of production tasks. Although robots are widely used in industry for operations such as welding, painting, and deburring, their use in high precision material removal processes is comparatively limited [3, 4, 5, 6].

Key technical challenges in using robots for high precision grinding operations stem from the relatively low static/dynamic stiffness [7, 8, 9, 10] compared to a precision grinding machine and, for an articulated arm serial link robot, from the variation in stiffness with arm configuration. Successful use of robots for machining in industrial applications requires careful design and analysis of the robotic system with attention given to the static and dynamic compliance of the robot in the presence of time-varying machining process induced forces. Forces generated during grinding can cause elastic deformations (deflections) of the robot, the grinding wheel, and the workpiece. Grinding force-induced deflections can lead to geometrical inaccuracies in the components being ground [11]. Since part dimensions in face grinding have very tight tolerances, it is important to

understand the effect of robot compliance on the grinding cycle. Elastic deflections of the robot structure can cause the actual material removal to be less than the commanded infeed of the robot. This essentially increases the total grinding cycle time. However, the influence of the face grinding process parameters on cycle time when using a compliant machine such as a 6-axis articulated arm robot is not well understood. Therefore, a process model is required to select the appropriate process parameters.

Another limitation in robotic machining is structural vibrations, which can result in poor surface quality of the part, reduction in wheel life, and limited production rates [12]. Any irregularities in the process can cause variations in the grinding forces that can dynamically excite the structure. As with other machine tools, robot vibrations are classified into two types: forced vibrations and self-excited vibrations [13]. Forced vibrations are caused by periodic disturbances external to the grinding process such as from an unbalanced wheel or spindle, electric motors, bearings etc. The resulting associated vibration frequency corresponds to that of the excitation source. A great deal of research has also been devoted to understanding self-excited vibrations in robotic machining [14, 15, 16, 17]. Self-excited vibrations are of two types, regenerative and mode-coupling. Mode-coupling vibrations are associated with natural frequency modes of the structure, in this case, the robot. It occurs when vibration in the thrust force direction generates vibration in the cutting force direction and vice versa. Regenerative chatter is caused by the regeneration of waviness on the workpiece surface. Face grinding of bearing rings involves producing parts with stringent requirements of face parallelism (< 15 μm) and flatness (< 5 μm) [18]. Structural vibrations can be a limitation when trying to achieve the stringent

flatness and parallelism tolerances. It is thus important to understand the type of vibration that affects the robotic face grinding operation to improve the resulting part quality.

Traditional methods employed for vibration mitigation in robotic machining involve passive and active strategies. Passive methods involve choosing a robot configuration with the maximum Cartesian stiffness at the end effector or modifying the system structure through the use of passive vibration absorbers. The Cartesian stiffness of the robot changes with different configurations of the robot arm and hence vibration can be reduced by selecting the optimal robot configuration [19]. Active vibration suppression strategy involves altering the system dynamics via the use of piezoelectric or electrostrictive actuators and using vibrations sensors mounted on the spindle [20, 21, 22, 23, 24]. On the other hand, active or semi-active vibration absorbers such as Adaptive Tuned Vibration Absorbers (ATVA) and magnetorheological elastomers have been used to absorb vibration [25, 26, 27]. Both are capable of adjusting their natural frequency by actively varying the stiffness and hence they have the ability to control vibrations under variable process conditions. Active vibration suppression strategies are costly and difficult to implement because additional hardware is required along with precise measurements of the machining process conditions. On the other hand, there is scope for further research passive vibration mitigation strategies, especially since robotic face grinding requires compensation of displacements at the part-wheel contact and of the angular misalignment between the bearing face and the wheel surface, as well as suppression of vibrations resulting from external sources.

To summarize, the need for research into process development, dimensional accuracy and surface finish improvement in robotic face grinding of bearing rings serves as the motivation for the research described in this thesis.

1.2 Research Objectives

In light of the problems and motivations discussed in the previous section, this thesis analyzes the influence of robot compliance on the face grinding process cycle time and part accuracy. It also investigates passive vibration mitigation and error compensation methods to enhance the part quality obtained in robotic face grinding. The specific objectives of this research are to:

1. Investigate the effect of robot compliance on the face grinding cycle time and part quality.
2. Identify the robotic face grinding process conditions necessary to optimize the grinding cycle time.
3. Investigate methods to improve the part quality in robotic face grinding with a focus on the effects of part-wheel angular misalignment errors and process induced vibrations.
4. Analyze the effect of robot configuration on the face grinding process cycle time.

The research objectives of this thesis are achieved through a comprehensive literature review of prior work followed by development of the robotic face grinding experimental setup, robot vibration mode characterization, robotic face grinding cycle process modeling, experimental validation of the model, and design and optimization of a novel flexible gripper to improve part quality.

1.3 Proposed Approach

A basis for understanding and characterizing the robotic face grinding process cycle is developed through a simplified analysis that accounts for the difference between the robot infeed rate and the actual material removal rate. An experimental setup for validating the process model is built by integrating a 6-axis articulated arm robot with a high speed spindle, a coolant supply system, a fixture for holding the rotary chuck at the robot end effector. The robotic face grinding system is characterized through modal impact hammer tests to determine the natural vibration modes of the system for a select configuration of the robot. The robotic face grinding cycle process model developed in the thesis relates the grinding force and the material removal rate with various process parameters including the grinding wheel speed, chuck rotational speed, grinding wheel type, and the Cartesian stiffness of the robot end effector. The model provides an estimate of the total grinding cycle time from the initial part-wheel contact to the end of the spark-out phase. The grinding process experiments involve running a complete grinding cycle for different sets of commanded robot feed rate and grinding wheel speeds for two different wheel grades. the grinding forces, the instantaneous displacements of the end effector and the frequency content of the displacements of the robot end-effector. Based on the process model, an optimum set of grinding process parameters that will meet the required dimensional accuracy and grinding process cycle time is determined. The ground samples are measured to characterize their flatness, parallelism and surface roughness. The flatness depends on various factors such as the initial alignment of the workpiece relative to the wheel surface, wheel type, and vibrations of the robot end-effector. The thesis also investigates the design and optimization of a novel flexible gripper to improve part quality by compensating for

robot alignment errors and vibration. Finally, a robot configuration (pose) optimization study is conducted to determine the best pose that results in the maximum Cartesian stiffness of the robot in the part feed direction, which also minimizes vibrations during the grinding cycle.

1.4 Thesis Outline

The remainder of this thesis is organized as follows. Chapter 2 presents a comprehensive review of the relevant prior work in robotic grinding. Chapter 3 describes the experimental test bed utilized in this work. Further, it includes characterization of the robot vibration modes, its Cartesian stiffness at the end effector, and damping for a selected arm configuration. Chapter 4 presents a static grinding process model for the face grinding process. It relates the process grinding forces and the material removal rates through various parameters like the grinding wheel type, grinding wheel speed, and the commanded robot infeed rate. The model permits determination of an optimal grinding strategy to achieve the minimum grinding cycle time and improved part quality. Chapter 5 presents the results of ground part quality (surface flatness, parallelism, and surface finish) measurements. A novel flexible gripper that compensates for part quality errors introduced by the part-wheel surface angular misalignment and resulting vibrations s designed and evaluated. Chapter 6 presents a robot pose optimization study to determine the best pose that results in the maximum Cartesian stiffness of the robot in the part feed direction while minimizing the vibrations. Finally, the major conclusions of this thesis and recommendations for future work are given in Chapter 7.

CHAPTER 2. LITERATURE REVIEW

A critical review of the relevant work available in the literature is presented in this Chapter. The review is divided into four areas: 1) prior work in grinding, especially face grinding, 2) robotic machining, 3) robotic grinding, 4) challenges in robotic machining, especially vibrations, 4) vibration mitigation strategies in robotic machining, and 5) robot pose optimization.

2.1 Face Grinding

Grinding is an important finishing process with broad industrial application. Grinding processes commonly consist of abrasive rotating tools that produce fine surface finish on the workpiece. Conventional grinding can be classified as: 1) Surface grinding, 2) Cylindrical grinding, 3) Internal grinding, and 4) Centerless grinding [28]. Face grinding is another surface finishing method, especially for producing plane-parallel workpieces such as end faces of components like connecting rods, piston rings, and bearing rings [29]. The face grinding process involves contact between the face of a workpiece (e.g. bearing ring) and the grinding wheel as shown in Figure 1. The objective is to grind the face of the part to achieve a given reduction in the height of the part while achieving the required part quality metrics. The advantages of face grinding are the high parallelism, surface flatness, and fine surface finish it is capable of generating. Face grinding can be classified into one-sided and double-sided face grinding.

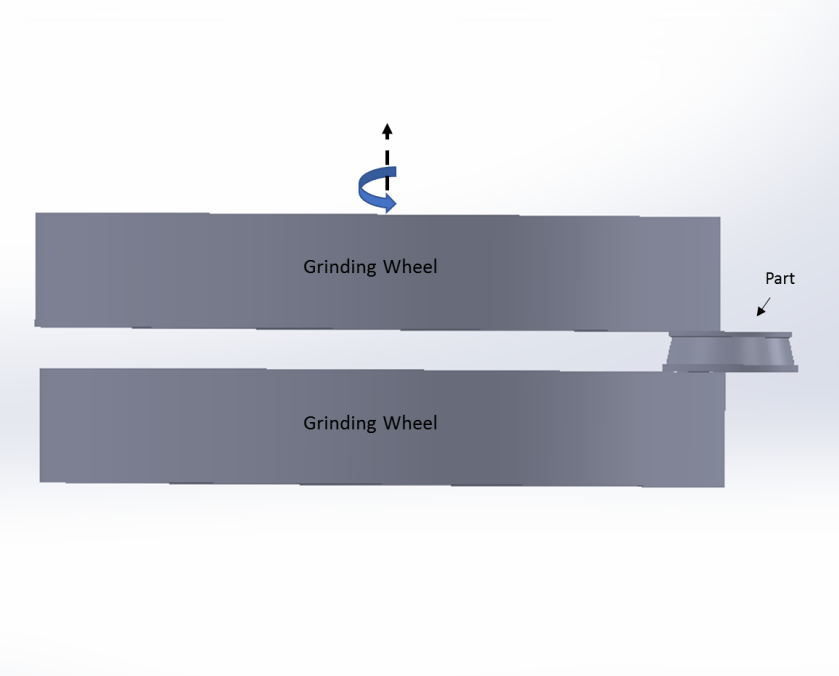

Figure 1: Face grinding operation.

Since this thesis concerns the face grinding process for bearing rings, the manufacturing process for bearing rings consist of the following major steps [30]: 1) steel in the form of bars, tubes or sheets is used as the raw material, 2) the stock material is pressed and cut out into steel rings, 3) the rings are turned on a lathe, and 4) the rings are finished using face grinding, centerless grinding, outside diameter and inside diameter grinding, and superfinishing. Bearing rings have stringent part quality requirements, especially surface flatness, parallelism, and surface finish. Conventional face grinding machines are traditionally used for this process but industries are exploring ways to utilize lower cost and more flexible machines such as robots to perform precision grinding or machining operations.

2.2 Grinding Process Modeling

Grinding process performance is intimately affected by the workpiece material properties, grinding wheel specifications, and machine stiffness. The kinematics of chip formation, the undeformed chip thickness, and the number of cutting points are known to affect the performance of grinding processes as discussed in earlier studies[31, 32, 33]. In the first of a series of pioneering papers, Hahn and Lindsay [34] established empirical relationships between the process forces and material removal rate for the cylindrical grinding process. In a second paper, Hahn and Lindsay [35] discussed the wheel wear characteristics and the wear ratio obtained in the cylindrical grinding process. They also analyzed the vibrations, chatter, and the resulting surface finish. Lindsay [36], and Hahn and Lindsay [37] derived an empirical relationship between the cylindrical grinding material removal rate and the normal grinding force, and the effect of wheel dressing parameters on the surface finish and the work surface profile. The material removal rate was found to be directly proportional to the normal grinding force. The constant of proportionality was defined as the material removal parameter. Kannappan and Malkin [38] found that the specific cutting and plowing energies in surface grinding decrease with increase in the table speed and feed rate and that the specific chip forming energy is independent of both. The wear flat area was found to be larger for higher table speeds and feed rates. Work on grinding force and grinding power modeling in surface grinding [39, 40, 41, 42] proposed a probabilistic chip thickness-based model to predict the power, tangential force, and normal forces in surface grinding. Lal [43, 44] studied the mechanics of chip formation and wheel wear in vertical surface grinding, where the wheel is tilted by

a small amount such that only the grains at the wheel periphery make contact with the workpiece during material removal as shown in Figure 2 below.

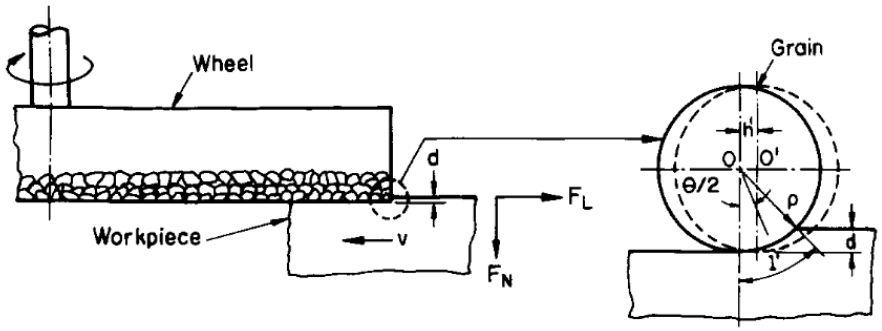

Figure 2: Schematic diagram of vertical surface grinding [43].

Their work showed experimentally that the normal grinding force increases with the table speed, depth of cut and material removal rate, as shown in Figure 3 below. The specific cutting energy was found to decrease with the material removal rate.

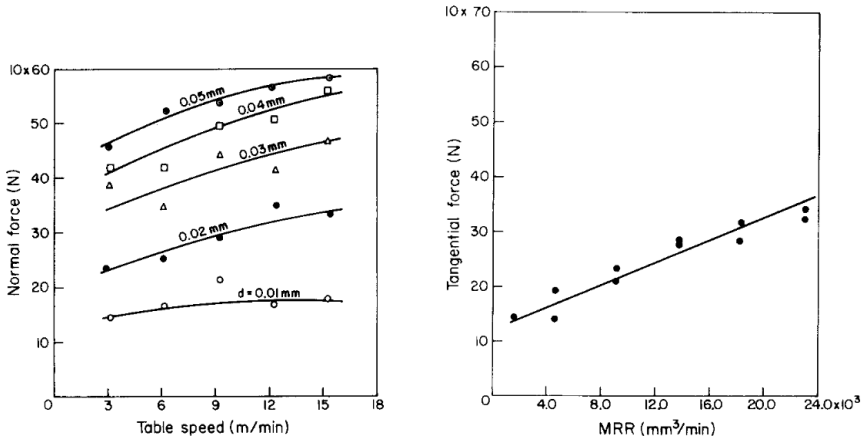

Figure 3: Variation of normal force with table speed (left figure) and variation of tangential force with material removal rate (right figure) [43].

Grinding forces cause deflections of the wheel, workpiece holder, and the machine, which produce geometric errors in the part and therefore limit the production rate. In order

to understand the role of deflections in grinding and its effects on the grinding process cycle time, Malkin [11] presented a continuous infeed analysis of the grinding cycle while considering the effects of machine stiffness, work speed, and grinding wheel grade on the overall grinding process cycle time. Optimization of the grinding process cycle time through the use of infeed rate control for accelerated spark-out is discussed in Malkin's work [45]. The strategy optimizes the grinding and dressing parameters for maximum removal rate subject to constraints on the surface finish.

It should be noted that the above research works on grinding are for cylindrical plunge grinding, centerless grinding, and internal cylindrical grinding. In particular, there is no reported work that addresses the process grinding force and material removal rate relationship for face grinding process.

2.3 Vibrations in Grinding

Machine compliance also causes problems related to grinding vibrations. Part quality and production rate can be affected by the vibrations produced during the grinding process. In case of machine tools, as discussed by Inasaki et al. [46], the vibrations are classified as self-excited vibrations and forced vibrations, as shown in Figure 4 below.

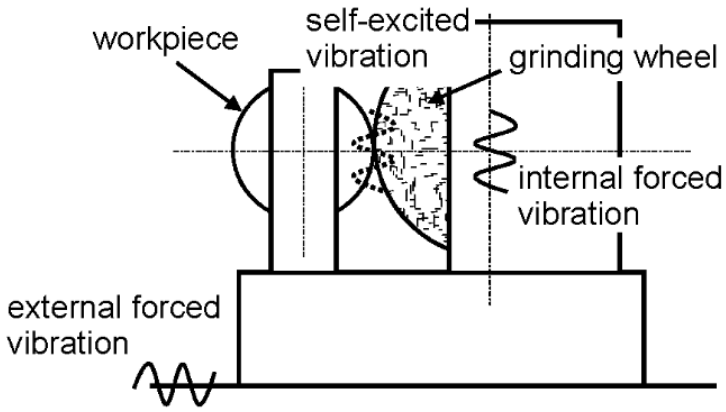

Figure 4: Vibrations in cylindrical grinding process [46].

Self-excited vibrations can be classified further into mode-coupling and regenerative vibrations. Mode-coupling vibrations are associated with the natural vibration frequencies of the machine structure. Regenerative vibration is caused by cutting through waviness on the surface of the workpiece produced in a previous pass. On the hand forced vibration is caused by sources of excitation external to the system such as an unbalanced wheel, motors, or bearings. Several researches have explored the effects of forced vibration on the grinding system performance, particularly the surface finish [47, 46, 48, 49]. Similarly, a great deal of research on understanding the effects of regenerative chatter in cylindrical grinding on the surface finish and production rate have been reported [50, 51, 52, 53, 54]. The effects of workpiece-wheel contact stiffness on machine vibrations have also been studied [55, 56, 57]. Much of these works have focused on understanding the effects of wave regeneration on the machine dynamics through experimentally derived stability criterion for vibration amplitude growth as a function of the machine stiffness, wheel-workpiece contact stiffness, and wheel and part speeds, etc. Also, their effects on the surface finish were analyzed. It

should be noted that all of the mentioned research is either for cylindrical plunge grinding or surface grinding. There are no reported works that address the influence of machine or robot stiffness on the vibration characteristics in the face grinding process.

Vibration mitigation strategies in grinding include either eliminating or isolating the vibration source. The other ways are through reduction of the wheel-workpiece contact stiffness and/or cutting stiffness and increasing the structural damping through addition of external dampers. Several researchers have analyzed vibration suppression strategies in grinding [46, 58, 59]. These studies analyzed the existence of process stability zones as a function of the wheel speed, grinding stiffness, contact stiffness, machine stiffness, and the wheel type. For example, Inasaki et al. [46] monitored chatter vibrations in cylindrical grinding due to the regenerative effect and analyzed the effects of varying the wheel/workpiece speed on chatter stability. In general, process parameters are selected so that the system stays within the vibration stability limits. Bzymek et al. [60], for example, focused on designing a flexible wheel for cylindrical grinding to reduce chatter through a reduction of the effective stiffness of the machine and the grinding wheel.

2.4 Robotic Grinding

Recently, following advancements in the robotic machining domain such as robotic milling [13, 61, 7, 62], work on robotic grinding has attracted the attention of researchers. Industrial applications that involve finishing steps in the manufacture of faucets, turbine blades, camshafts, blisks in aero engines, etc., which have been traditionally done using five-axis CNC machines, are quite expensive. Industrial robots have been proven to be an

economical solution where the robot can be programmed to machine complex geometries with the only exception of having problems with geometric accuracy due to the robot's low structural stiffness. Due to the geometric complexity of the surfaces of blisks, the finishing step after milling is typically done by skilled workers, which is intensive and time consuming. Automating the finishing process using industrial robots has turned out to be invaluable in terms of cost and time savings. Robotic grinding has also turned out to be a valuable method for finishing of turbine blades. It has relieved humans from working in dirty and noisy environments, and resulted in improved product quality and lower production costs [63, 64].

Many robotic grinding applications involve grinding using abrasive belts, which involves mounting a workpiece at the end of a robot arm and feeding it into the moving abrasive belt as shown in Figure 5 below.

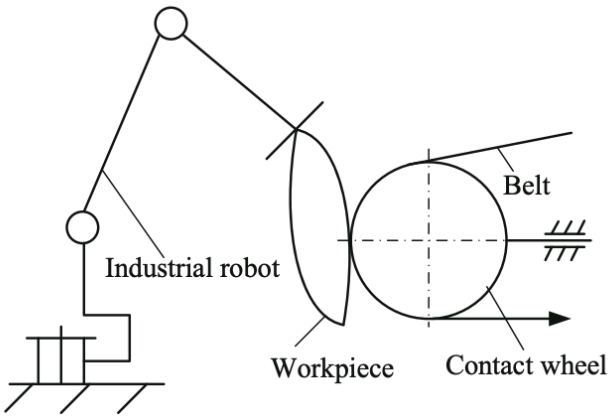

Figure 5: Robotic belt grinding setup [65].

Wang et al. [65] analyzed the depth of cut on robotic belt grinding contact wheel deformation due to belt tension using analytical local stress and material removal model

and validated the models through FEM simulation and grinding tests. Zhu et al. [66] found that the specific cutting energy in robotic belt grinding is independent of the ideal depth of cut but is dependent on the depth of grain penetration. They also found that the sliding specific energy is dominant compared to ploughing and chip formation energies. Ren et al. [67] developed simulation models for the robotic belt grinding process to estimate the material removal rate. Through their work, it is possible to improve path planning and reduce potential geometrical inaccuracy issues. Yixu et al. [68] worked on tracking time varying process response in robotic belt grinding, like belt wear, through statistical machine learning to accurately predict the material removal rate. To mitigate the problem of poor accuracy in robotic belt grinding, Xie et al. [69] designed a fuzzy controller to achieve a force-position hybrid control to improve positional accuracy. Work by Sun et al. [70] focused on in-process path calibration using a linear displacement sensor. The pose of the displacement sensor was calibrated using a spherical surface and the calibrated sensor was used to calibrate the relative pose of the robot's tool frame. A force control strategy was implemented using the error between the commanded and real positions.

Similarly, in the case of robotic grinding of turbine blades and blisks, Huang et al.'s work [71] focused on controlling and optimizing the path of the belt grinder, installed on the six-axis robot, to compensate for belt wear and to control the pressure between the wheel and the workpiece surface. Thomessen et al. worked [72] on robotic grinding of large turbines with a focus on force control using active feedback from the force sensor attached to the robot end-effector. The control algorithm essentially ensures high productivity and good grinding performance. Dai et al. [73] developed a process model for the robotic disk grinding process using experimental data that relate the depth of cut to

the grinding forces. Using the model, adaptive pole placement method was used to control the normal grinding force.

Based on the foregoing review of prior work on robotic grinding, it is evident that there is no relevant work on the robotic face grinding process that focuses particularly on the grinding cycle behavior and part quality aspects, that are key to achieving the desired productivity and part quality requirements for high precision components such as bearing rings.

2.5 Vibration in Robotic Machining and Mitigation Strategies

As discussed in the earlier section, the vibrations in robotic machining can be classified similar to vibrations in conventional machine tools, namely, forced vibrations and self-excited vibrations. Pan et al. [13] claimed that mode coupling chatter is the dominant chatter vibration mechanism in the robotic milling process. Iglesias et al. [7], Chen and Dong [74], Mousavi et al. [62] and Pandremenos et al. [75] reviewed the vibration issues in robotic machining processes. The stability lobe diagram is commonly employed to select machining process parameters (e.g. spindle speed and depth of cut) to avoid regenerative chatter, as discussed by Tlusty et al. [76]. The process parameters can be chosen from the diagram based on the stability limits. Work by Mousavi et al. [62] and Wang et al. [77] suggests that feed rate and depth of cut are the two most important process parameters that influence robotic machining stability. Instead of selecting machining parameters to make the system stay within the stability limits, another strategy for avoiding regenerative chatter is to employ external devices that absorb the vibration energy to make the system stable. Miguelez et al. [78] developed a dynamic vibration absorber for a boring

bar that essentially acts like a spring plus damper system to absorb the vibration. Tarng et al. [79] used a piezoelectric actuator as a tuned vibration absorber to improve the stability limits of the turning process, which could potentially be adapted to mitigating chatter vibrations in robotic machining and grinding. Silva et al. [80] designed embedded piezoelectric patches in the tool-holder in the turning process to act like a vibration damper in the form of a passive shunt circuit. Another active method was proposed by Chen et al. [81] who designed a magnetic actuator that acts like an active damper for boring bars. The boring bar is instrumented with an actuator to counter the vibrations by increasing the dynamic stiffness of the boring bar, which results in an increase in the chatter-free depth of cut. An H_∞ optimal controller was designed for active damping of the boring bar.

Mode coupling chatter in robotic machining is caused by the 1) low Cartesian stiffness of the robot, 2) principal stiffnesses of the robot being very close to each other and hence, a forcing function in one direction excites the vibration mode in the direction and vice-versa. Passive strategies to mitigate mode-coupling chatter include identifying the robot's Cartesian stiffness in the workspace and selecting a robot pose with the maximum stiffness [82, 83, 84]. Pan et al. [13] suggested selecting the tool path and feed direction such that the Cartesian stiffness of the robot in that direction is maximized. Other techniques include the use of a dynamic vibration absorber attached to the end-effector of a milling robot to reduce vibration [85]. Active strategies for reducing mode-coupling chatter include the force control strategy developed by Pan and Zhang [14]. Wang et al. [86] and Xie and Sun [69] developed active force feedback control to maintain process stability during robotic milling and robotic grinding, respectively. Yuan et al. [87] used a

magnetorheological elastomer (MRE) as an active tuned vibration absorber material to suppress chatter vibrations in robotic milling as shown in Figure 6Figure 7 below.

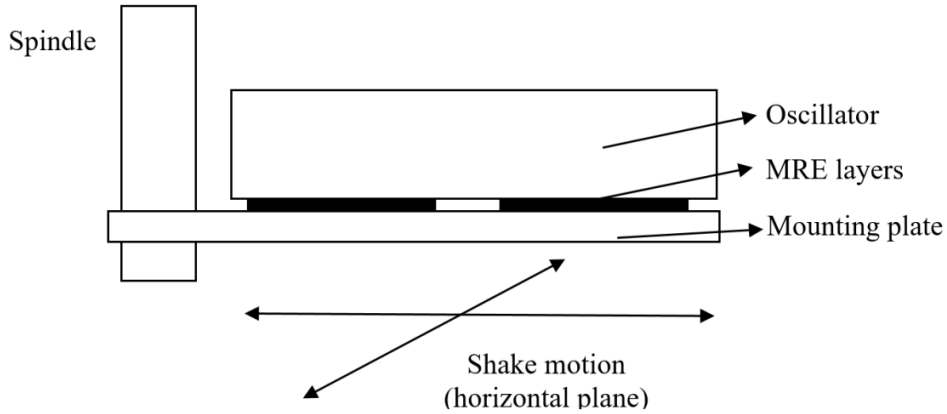

Figure 6: MRE (Magnetorheological Elastomer) layers acting as vibration dampers [87].

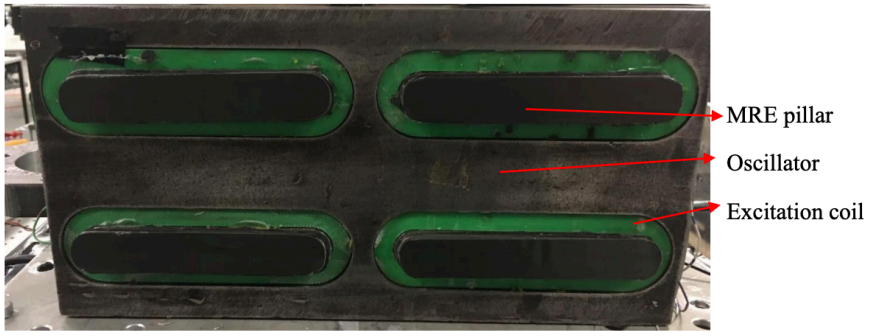

Figure 7: MRE (Magnetorheological Elastomer) absorbers [87].

The stiffness and damping of the MRE is controlled by varying the magnetic field. This is particularly helpful for absorbing the vibration energy in mode-coupling chatter producing in robotic milling. Chen [88] developed eddy current dampers for vibration suppression in robotic milling process, as shown in Figure 8 below. The performance of the eddy current damper is verified by showing (through experiments) that the peaks of the

end-effector FRF (frequency response function) are damped significantly compared to the case without using the dampers.

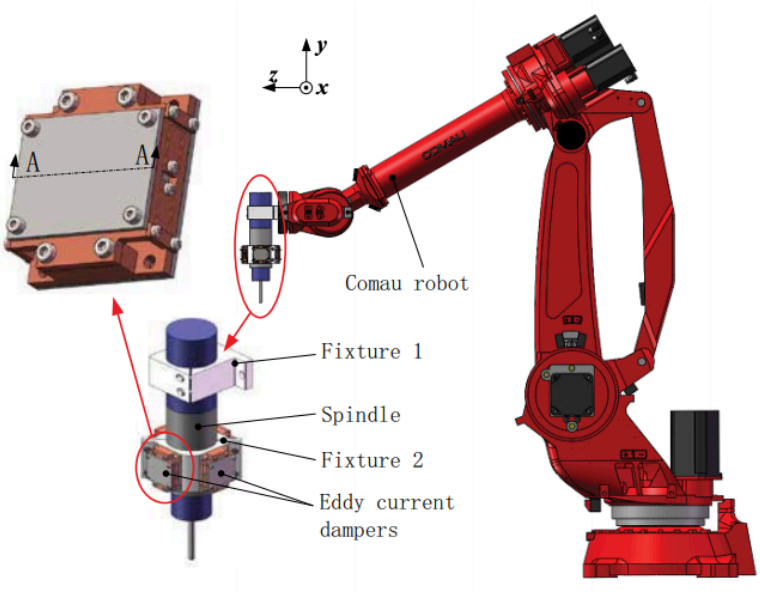

Figure 8: Eddy current damper for vibration suppression in robotic milling [88].

The aforementioned methods focus on maximizing the robot stiffness, force control, or absorption of chatter vibration through increased system damping or tuned vibration absorbers. The chatter avoidance stability limits that are often governed by robot speed and forces, limit productivity. The active strategies discussed earlier require the use of sensors and feedback control loops, which necessitate sophisticated hardware that are difficult to implement and are costly. Face grinding of bearing rings involves the contact of the workpiece ring face with a grinding wheel. The bearing ring surface needs to be in uniform contact with the wheel to avoid the generation of time varying forces that can produce vibrations resulting in poor surface finish. Thus, there is a need to develop strategies for vibration mitigation that are inexpensive and easy to implement in the face grinding process.

2.6 Robot Pose Optimization

As explained earlier, the main advantage that robots offer in machining and grinding applications are that they are flexible, occupy less space, and are generally less expensive than CNC machine tools, especially for aerospace applications and for high precision applications such as in the bearing industry. However, because of their low structural stiffness, the positioning accuracy of industrial robots is poor, which results in low part dimensional accuracy. In addition, in processes characterized by time-varying process forces, excessive structural vibrations can result, which in turn yields poor surface finish. In robotic face grinding, it is important to study how the Cartesian stiffness of the robot end effector in the grinding infeed direction affects the grinding process cycle time. Since the industrial robot is an articulated multi-dof structure, the Cartesian stiffness of the robot changes with joint configuration or pose. By optimizing the robot pose, the Cartesian stiffness of the robot end effector can be improved, thereby reducing the deflections of the robot and its effect on part dimensional accuracy.

Salisbury [89] developed a stiffness model to establish a relation between deflection at the end-effector and joint deflection. This model is utilized in the current study to derive the Jacobian transformation from the robot's joint frame to the Cartesian frame. Chen et al. [90] derived a complementary stiffness model that accounts for varying stiffness due to a force at the end-effector. Abele et al. [91] derived a compliance model that can take care of the singularity poses of the robot. He proved that calculation of the inverse Jacobian introduces estimation errors in the stiffness models. This fact was considered in the current study by estimating the Cartesian compliance matrix and then taking its inverse to get the stiffness matrix, since directly estimating the stiffness matrix involves taking inverse of the

Jacobian transformation matrix. Guo et al. [92] devised a stiffness performance index that when maximized ensures an optimum robot posture. Lin et al. [93] proposed a global posture optimization strategy based on a kinematic performance evaluation index. Zargarbashi et al. [94] worked on a novel concept of robot transmission ratio as an optimization strategy for trajectory planning of machining robots.

It should be noted that although robot pose optimization is a well-explored research topic, this thesis leverages the existing theory to address robot pose optimization in robotic face grinding.

2.7 Summary

It can be deduced from the literature survey presented here that although significant research has been done in grinding and robotic machining, there is relatively very little scientific knowledge of the robotic face grinding process. Specifically, knowledge of the effect of robotic face grinding process parameters on the process performance measured in terms of the grinding process cycle time and part quality is required to successfully develop and implement an effective robotic face grinding solution for high precision components such as bearing rings. In addition, knowledge of the vibrational characteristics of robotic face grinding is necessary to obtain high quality parts.
The existing methods for vibration mitigation suffer from the following drawbacks: 1) they are costly and difficult to implement because of the hardware required, and 2) methods suitable for robotic face grinding are not available. These drawbacks motivate the work on a novel flexible workpiece gripper insert presented in this thesis.

CHAPTER 3. EXPERIMENTAL SETUP AND CHARACTERIZATION

This chapter discusses the experimental setup and vibration characterization of the 6-axis articulated arm industrial robot utilized in the current work. As discussed in later chapters, it is important to understand the natural resonant modes (frequencies) of vibration of the robot in order to determine if any of these modes are excited during the grinding process, causing undesirable vibrations that negatively impact part quality. Characterization of the resonant vibration modes of the robotic face grinding experimental setup is carried out using modal impact hammer tests, which has been used by other researchers in the robotic machining domain [95, 96, 97].

3.1 Experimental Setup

The robot used in the face grinding process setup is a Staubli RX 170, which is a 6-axis robot. The robot is installed inside a robotic work cell bounded by industrial safety fencing as shown in Figure 9.

Figure 9: Robot workcell.

The spindle used for the grinding wheel is a Weiss GMBH 175369 spindle controlled by a Siemens 611 U controller and water cooled by a chiller. Figure 10 shows the grinding spindle and the chiller unit for the spindle.

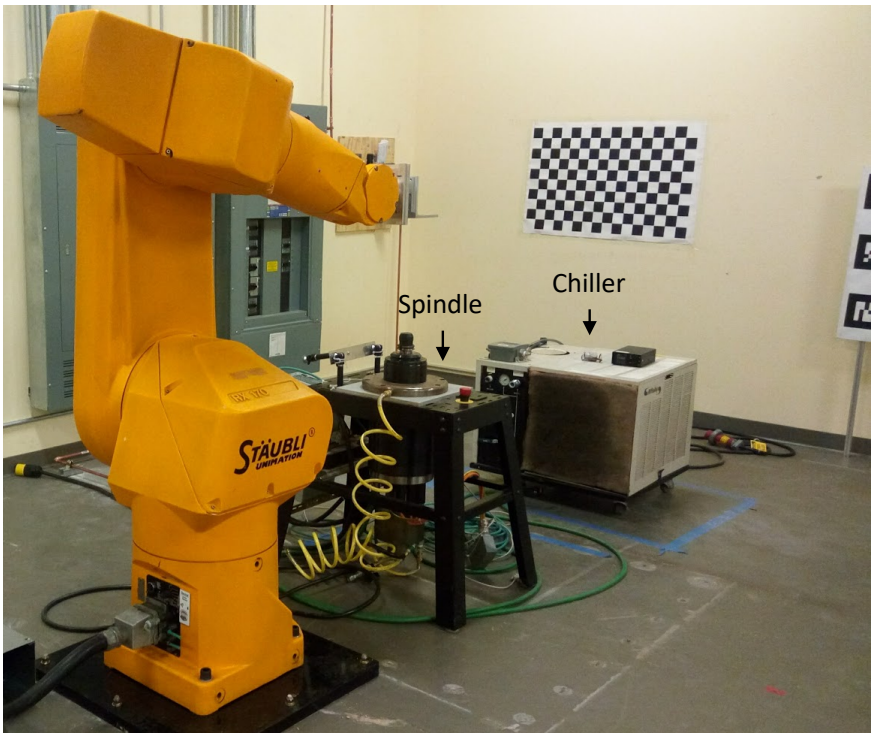

Figure 10: Grinding wheel spindle and chiller unit.

An L-bracket is used to hold the 3-jaw chuck motor, which grips and rotates the workpiece, on the robot end-effector, as shown in Figure 11. The six-axis force/torque sensor (ATI Omega 85) is sandwiched between the L-bracket and the robot end effector.

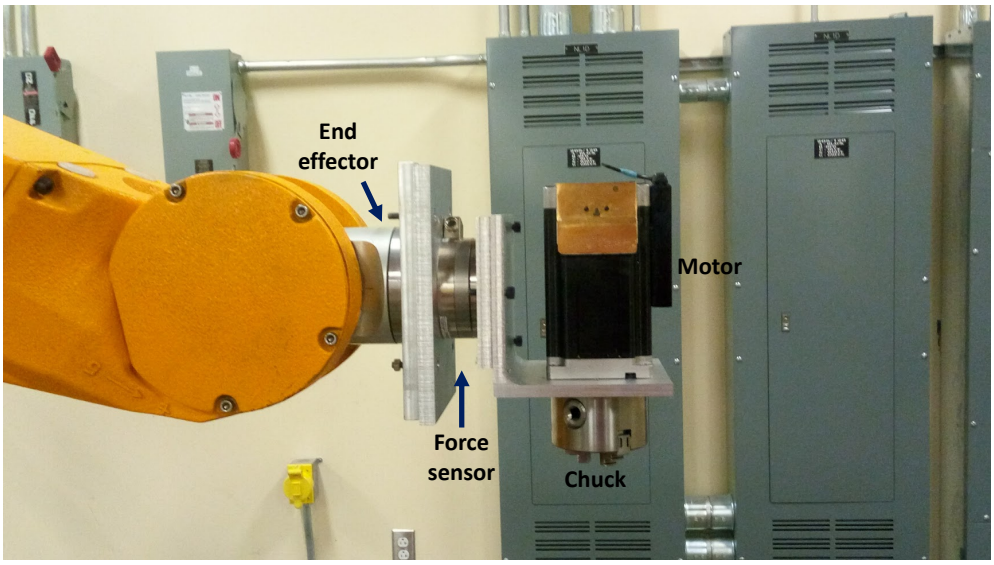

Figure 11: Robot end-effector assembly.

Since grinding operations require coolant supply, a sheet metal coolant collection tank was fabricated and installed on top of the wheel spindle, as shown in Figure 12.

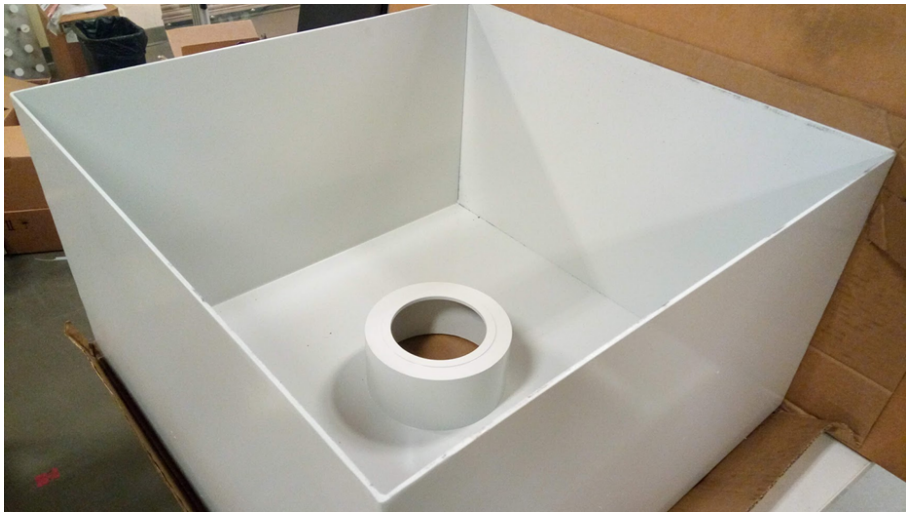

Figure 12: Robotic grinding coolant collection tank.

The grinding wheel was attached to the spindle via a custom-designed adaptor plate that connects the wheel to the SK 40 interface in the spindle, as shown in Figure 13.

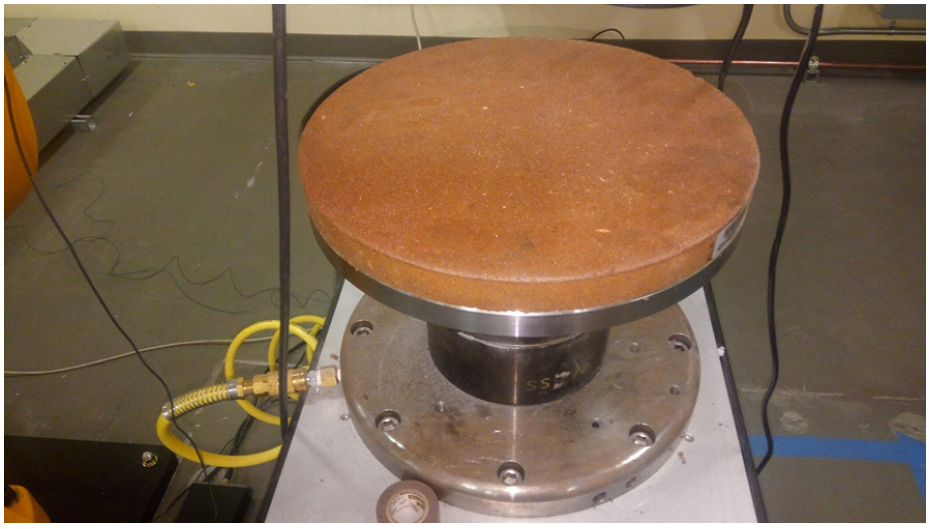

Figure 13: Grinding wheel mounted on spindle via adaptor.

A coolant supply system for grinding was integrated into the setup, as shown in Figure 14.

Figure 14: Grinding coolant supply tank [98].

To measure the displacement of the end effector relative to the grinding wheel surface during the face grinding process, a 1-D Keyence laser displacement sensor (LK-G3000) was fixed to the L-bracket with the laser directly pointing at the wheel surface. A tri-axial accelerometer (PCB SN-163555) was attached to the robot end effector, as shown in Figure 15. The X_G, Y_G, Z_G is the global frame attached to the robot base.

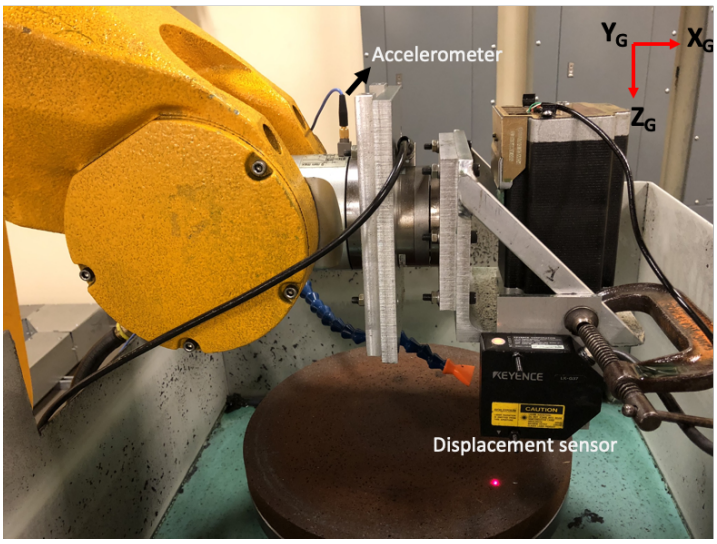

Figure 15: Laser displacement sensor and accelerometer.

3.2 Modal Characterization of Robot

It is important to understand the factors that lead to vibrations during face grinding. There are two types of vibrations relevant to grinding and machining operations in general: forced vibration and self-excited vibration. Forced vibrations are produced when the machine structure is excited by a time-varying external forcing function (e.g. due to periodic forces generated in the process), which causes it to vibrate at the frequency of the forcing function. In the context of robotic machining, self-excited vibrations are generally

due to coupling between the principal stiffness directions of the structure when excited by a time-varying external forcing function (e.g. mode coupling chatter) [15]. Experimental modal analysis is an experimental technique for understanding the robot's natural resonant modes using modal impact tests. Following the procedure described by Schwarz et al. [99], the modal impact test consists of exciting the mechanical structure with an instrumented impact hammer and measuring the resulting vibrations of the structure with an accelerometer. The measured impact force signal and the acceleration signal are used to compute the frequency response function (FRF) of the structure, which is a measure of the displacement at a point of measurement per unit excitation force at a particular forcing frequency. Figure 16 and the following equation summarize the FRF determination process.

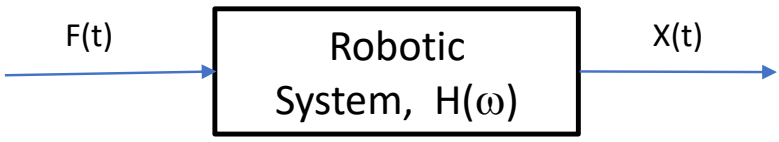

Figure 16: FRF block diagram.

Or, in the frequency domain,

$$H(\omega) = \frac{X(\omega)}{F(\omega)} \tag{1}$$

The accelerometer is mounted at a location on the structure where the vibration response is to be measured, as shown in Figure 17-Figure 19. In the present study, the impact hammer is used to excite the structure by impacting the workpiece, which is held in the 3-jaw chuck motor.

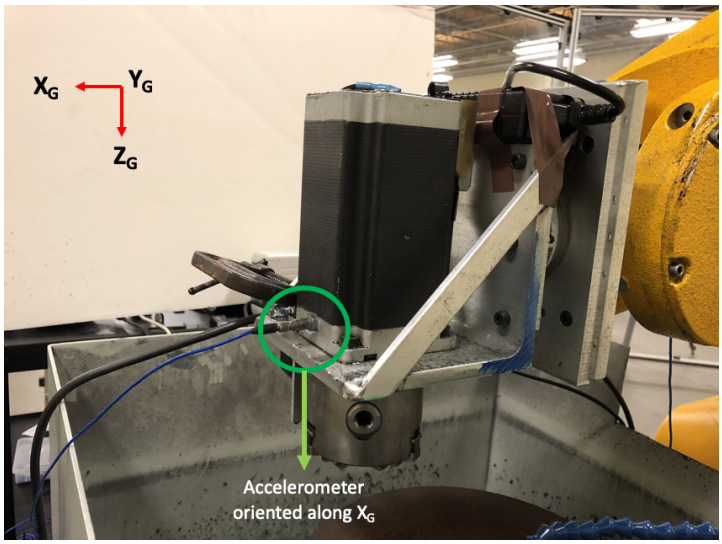

Figure 17: Uniaxial accelerometer mounting for measurement of FRF along X_G (axes shown is the global frame attached to robot base).

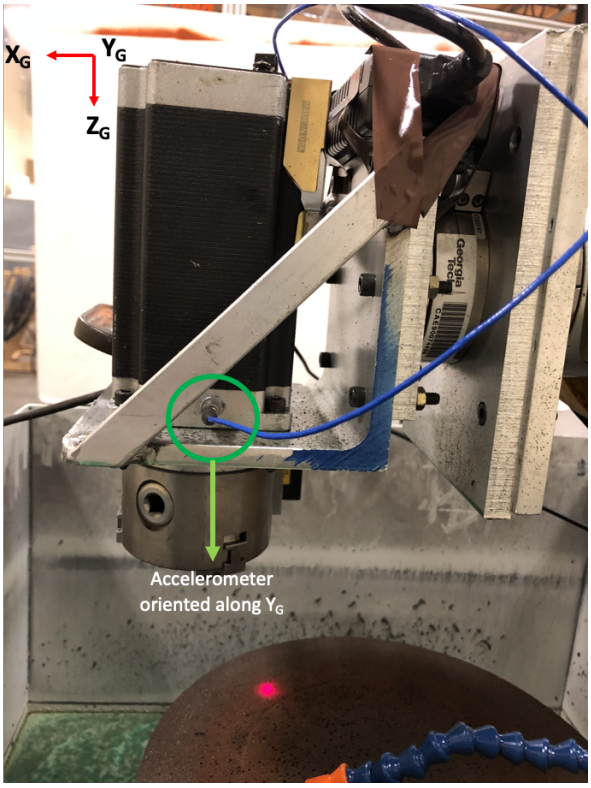

Figure 18: Uniaxial accelerometer mounting for measurement of FRF along Y_G (axes shown is the global frame attached to robot base).

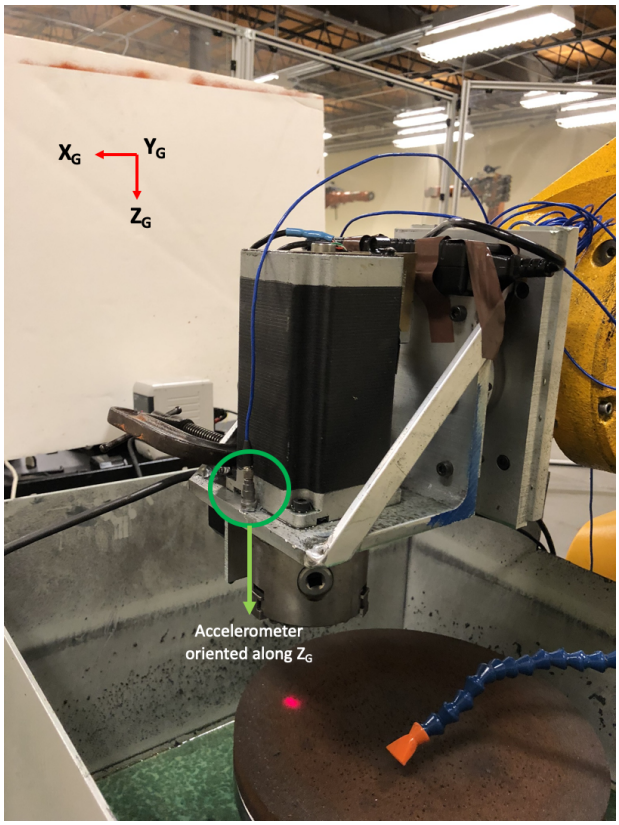

Figure 19: Uniaxial accelerometer mounting for measurement of FRF along Z_G (axes shown is the global frame attached to robot base).

The FRFs of the robotic face grinding setup when excited in each of the three orthogonal directions in the robot's global frame of reference are shown in Figure 20-Figure 22.

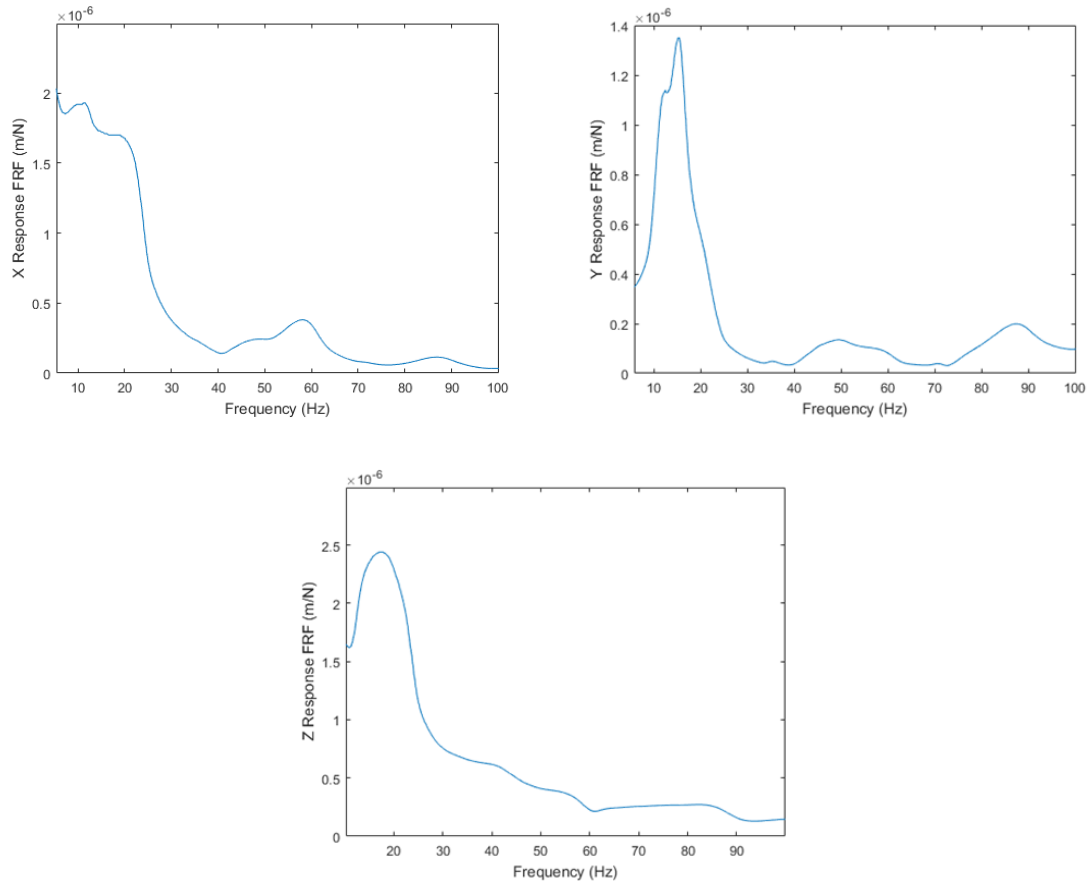

Figure 20: Responses in X_G, Y_G, Z_G directions when impacted in the X_G-direction.

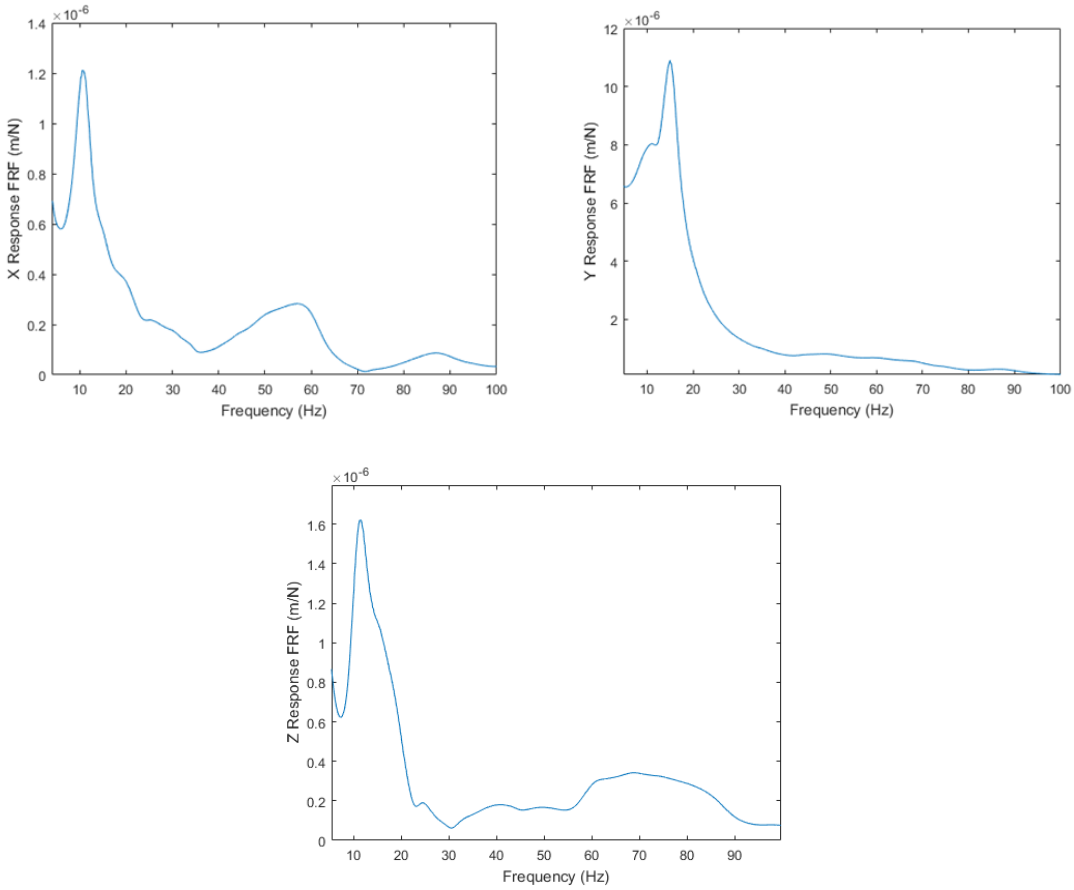

Figure 21: Responses in X_G, Y_G, Z_G directions when impacted in the Y_G-direction.

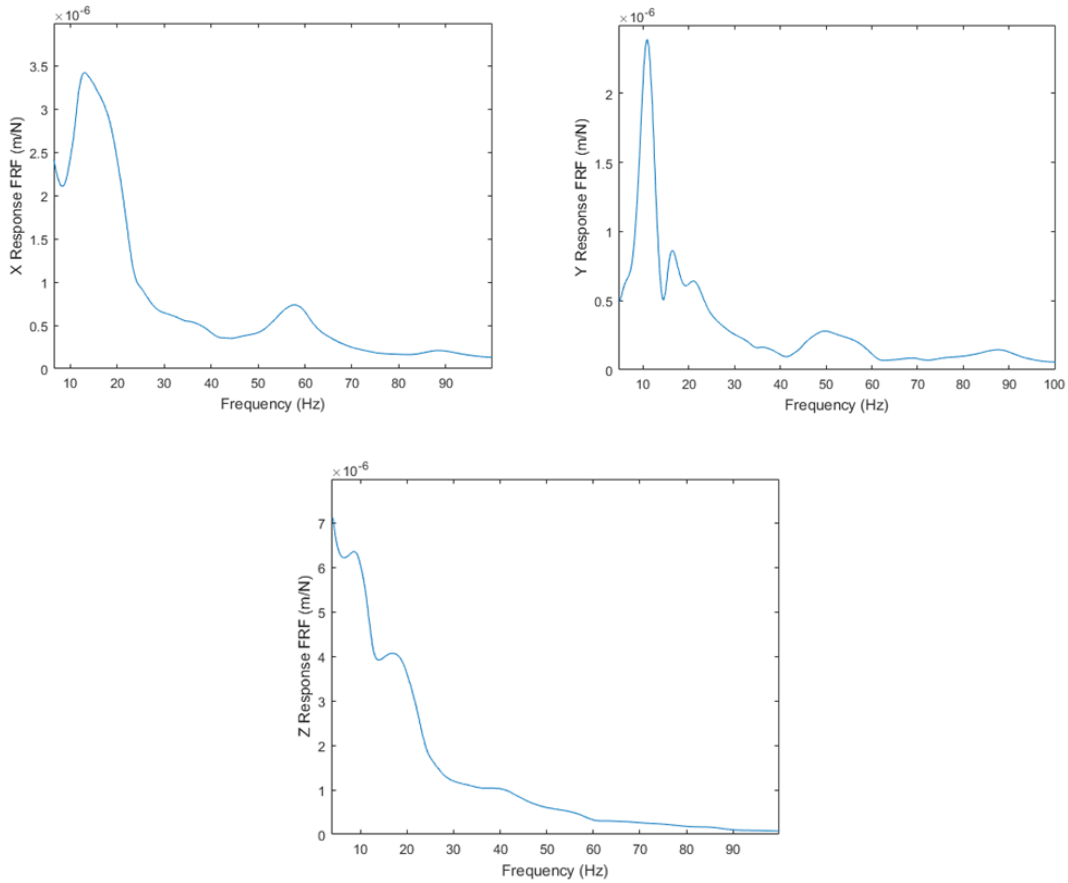

Figure 22: Responses in X_G, Y_G, Z_G directions when impacted in the Z_G-direction.

The dominant natural resonant vibration modes of the robotic face grinding setup in the different directions are summarized in Table 1.

Table 1: FRF results for the robotic face grinding setup.

Impact Direction	Response Direction	Peak Frequency (Hz)	Response Magnitude (x 10^{-6} m/N)
X_G	X_G	11	1.93
X_G	Y_G	15	1.35
X_G	Z_G	18	2.56
Y_G	X_G	11	1.21
Y_G	Y_G	15	11.0
Y_G	Z_G	11.4	1.62
Z_G	X_G	12.4	2.42
Z_G	Y_G	11	2.39
Z_G	Z_G	9	6.36

In analyzing the FRF results, only the most dominant peaks in the FRFs are considered. It can be seen from Table 1 that the robotic face grinding setup has resonant frequencies that range from 9 Hz to 18 Hz, which is typical for industrial robots. For impact in the Z_G-direction, the compliance in the Z_G-direction is highest with a magnitude of 6 x 10^{-6} m/N, compared to the other directions. The two highest peaks appear very close to each other in the response. This means vibration will dominated by the highest frequency peak along with some contribution from the closest peak. Also, a comparison of the Z_G-direction compliances for different impact directions shows that the compliances associated with the largest peaks are higher in Z_G than in the two other orthogonal directions, which is expected since the impact in a particular direction should generate the

highest response along that direction. For the system compliance in the Y_G-direction, the peak response magnitude for impact in the Y_G-direction is larger than the responses due to impact in the other two orthogonal directions. However, of the nine FRFs, the Y_G-direction response due to impact in the same direction is approximately ten orders of magnitude larger than the other eight responses. This is probably because the robot end-effector is least stiff in the Y_G-direction for the pose considered and is therefore more prone to resonance when excited at its natural frequency in this direction. Similarly, for impact in the X_G-direction, the response in the Z_G- and X_G-directions are comparable. Also, if the X_G-responses for different impact directions are compared, the peak Z_G-impact and X_G-impact responses are comparable. Thus, it can be concluded that the X_G-direction response is significantly coupled with the Z_G-direction response. This is important because the grinding force is a three-dimensional vector, and the robotic system can vibrate in multiple directions depending on the frequency content of the force vector components.

3.3 Summary

The experimental setup for the robotic face grinding process was described in this chapter. The vibration characteristics of the experimental setup were characterized through modal impact hammer experiments. Specifically, the FRFs of the robotic setup were determined through modal impact tests to establish the dominant natural frequencies of the robotic setup, which will be utilized in later chapters to determine if the face grinding conditions cause any of the natural resonance modes of the robot end-effector assembly to be excited.

CHAPTER 4. ROBOTIC GRINDING PROCESS MODEL

4.1 Introduction

In this chapter, the effects of time-varying grinding forces on the instantaneous static deflections of the articulated 6-axis robot and their effect on the overall grinding cycle are analyzed. The objectives in precision grinding of bearing rings are to achieve a tight tolerance on the width dimension, the desired flatness and parallelism of the ring faces, and the desired surface finish of the ring faces. During the face grinding operation, the actual infeed of the robot end-effector, which holds the bearing ring, does not match the commanded infeed. This is because the robot elastically deforms under the influence of the forces generated at wheel-workpiece interface. It is therefore necessary to study the deflections of the robot end-effector to determine the actual material removal rate. Note that only the robot static deflections and their effect on the material removal rate are analyzed in this chapter. The frequency content of the grinding forces and the robot end-effector acceleration (in lieu of displacements) will be analyzed in the next chapter to determine whether the grinding forces excite the natural vibration modes of the robot and whether these modes have any impact on the part surface finish.

The static displacement model of the robot end-effector leverages prior work by Hahn and Lindsay [100, 36, 37] on plunge cylindrical grinding where they developed a relationship between the material removal rate and the system compliance, wheel speed, and the commanded infeed. In a similar vein, the robotic face grinding cycle is modeled and analyzed in this chapter by adapting Malkin's [11] work on cylindrical grinding to understand the effect of the aforementioned parameters on the cycle time and the system

time constant. In the following sections of this chapter, the overall methodology and approach are described, followed by experimental validation, discussion of results, and key findings.

4.2 Robotic Face Grinding Process

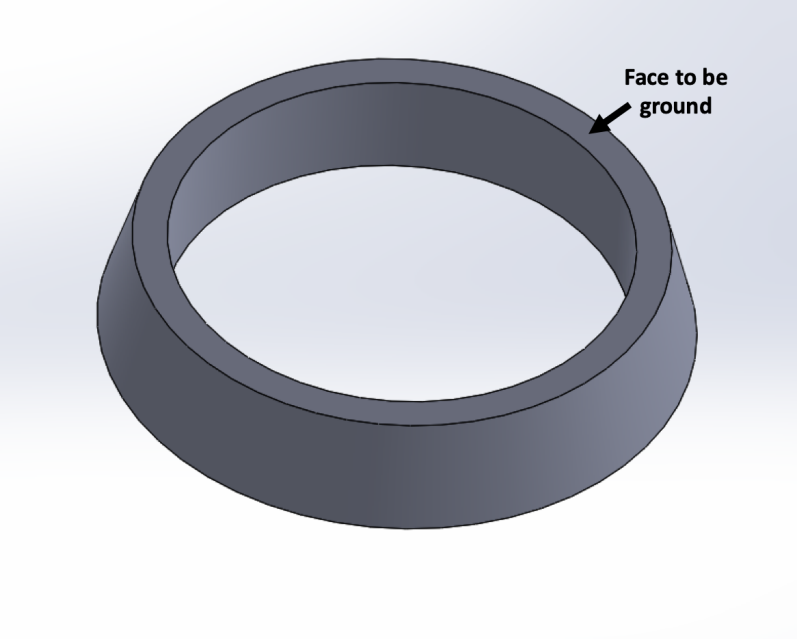

Figure 23: Hardened bearing ring face.

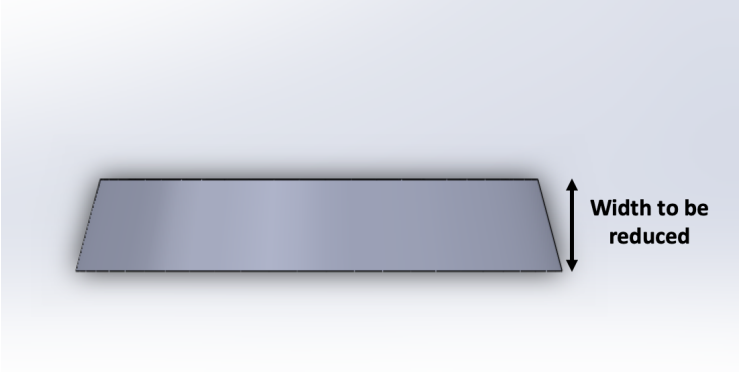

Figure 24: Inner bearing ring width dimension.

Figure 23 shows a representative internal bearing ring. The objective is to grind the face of the ring in order to reduce the width of the ring while meeting the flatness, parallelism, and surface finish requirements. Figure 24 shows the width dimension that must be ground. As shown in Figure 25, the ring is held in a rotating chuck mounted to the robot's end effector, which is fed toward the periphery of the grinding wheel surface where the wheel speed is maximum. The face grinding process involves contact between the rotating face of the bearing ring and the rotating grinding wheel as shown in Figure 25. The grinding force generated during material removal produces static deflection of the robot, which manifests as a difference between the commanded infeed and the actual infeed.

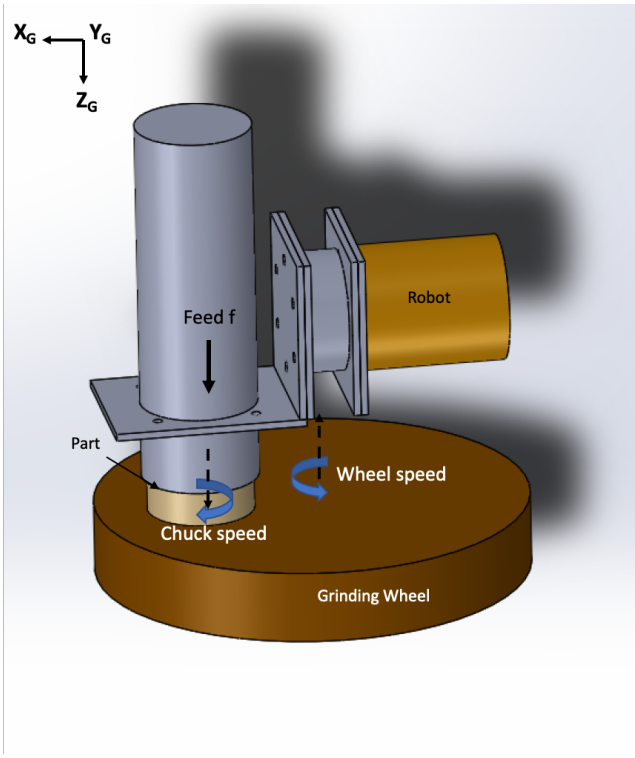

Figure 25: Process configuration and nomenclature.

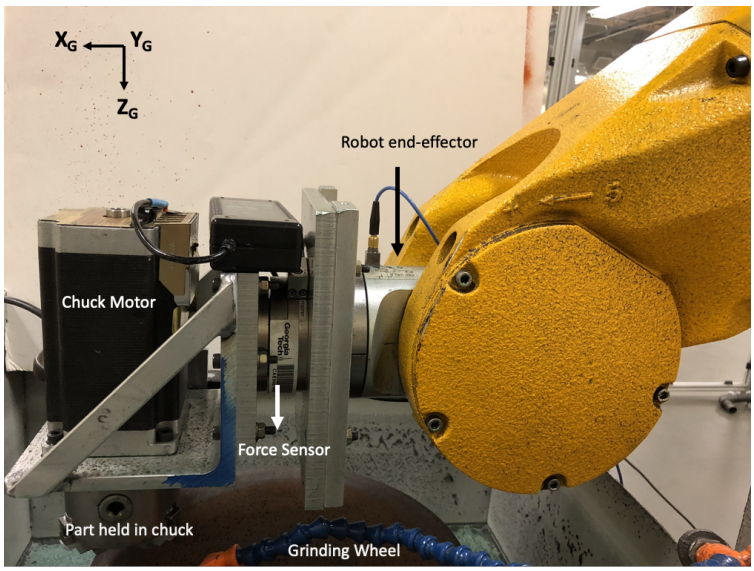

Figure 26: Robot end effector.

4.3 Process Modeling

As mentioned previously, the face grinding operation involves feeding the rotating bearing ring face into the wheel surface at a fixed infeed rate. Figure 25 illustrates the process configuration and the associated nomenclature.

The rate at which the part feeds into the wheel is denoted as f and the surface area of the ring is denoted as A. The material removal rate can thus be written simply as:

$$MRR = f\ A \tag{2}$$

Prior work on precision cylindrical plunge grinding by Hahn and Lindsay [37] has shown that the material removal rate is linearly proportional to the normal force intensity (defined as the force per unit width of the wheel-part contact) generated between the ring face and the wheel. The relationship has been illustrated in Figure 27 along with the grinding conditions.

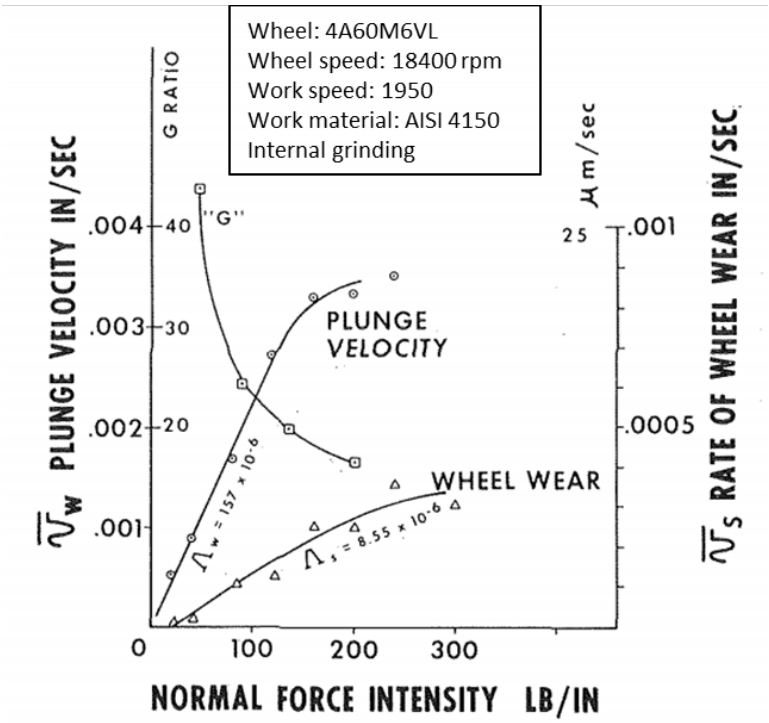

Figure 27: Plunge grinding velocity versus the normal force intensity [37]

Based on Hahn and Lindsay's work, the following equation can be written,

$$k_g \, MRR = \, F_n \tag{3}$$

where k_g is the grinding stiffness constant, which relates the normal grinding force F_n to the material removal rate (MRR).

Substituting for MRR from Eq. (2) into Eq. (3) yields,

$$k_g \, f \, A = \, F_n \tag{4}$$

Hahn and Lindsay considered the material removal rate per unit width to be proportional to the normal force intensity through a proportionality constant they termed the metal removal parameter (λ_w), which is inverse of the grinding stiffness k_g. Therefore, we can rewrite the above equation in terms of the material removal parameter as,

$$f\ A = \lambda_w\ F_n \tag{5}$$

As will be discussed shortly, the material removal parameter depends on the process conditions such as the wheel speed, chuck speed, wheel hardness, cooling condition, etc. Another important result from the work of Hahn and Lindsay [37] is that the material removal parameter is directly proportional to the rotational speed of the workpiece relative to the wheel speed. However, since the wheel speed is much greater than the work speed, it is approximated as the wheel speed. An example of this fact can be seen in Figure 28 where the material removal parameter is plotted against the wheel speed in internal grinding of roller bearing cups. Understanding the effect of wheel speed is important since it affects the surface finish, material removal rate, deflection of the robot, and spark-out time.

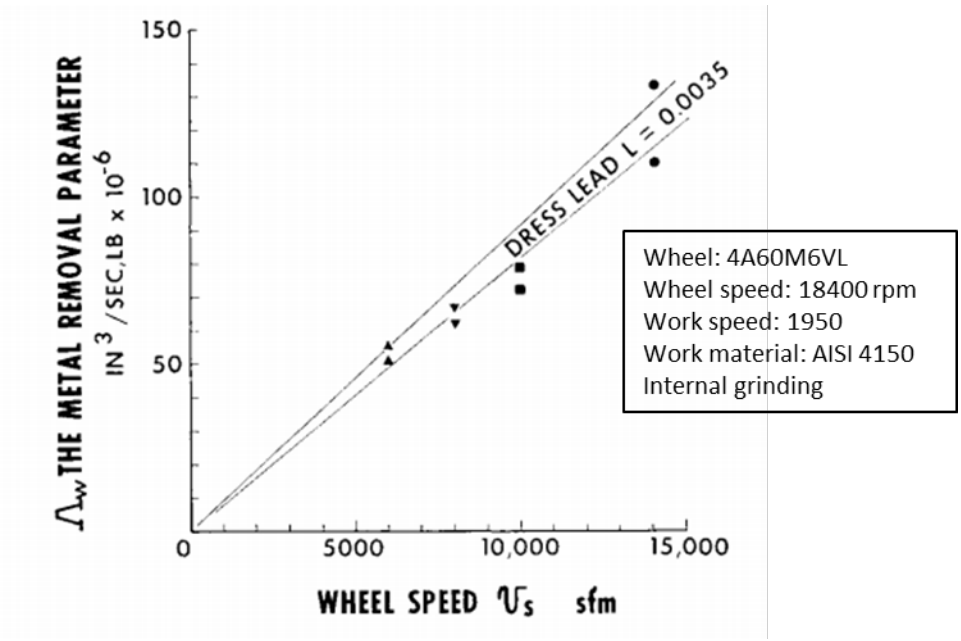

Figure 28: Material removal parameter versus the wheel speed [37].

The next section discusses how the material removal rate is related to the robot Cartesian stiffness in the normal (infeed) direction and analyzes its effect on the total grinding cycle time and the system time constant.

4.4 Robotic Grinding Process Cycle

Since the objectives of this work are to understand the effect of robot compliance on the grinding process cycle and to identify the process and machine parameters that minimize the process cycle time, it is necessary to study the robotic grinding cycle in first place. As shown schematically in Figure 29, the grinding cycle consists of an initial

roughing phase ($t < t_1$) at a constant commanded infeed rate followed by a spark-out phase ($t > t_1$) with no infeed.

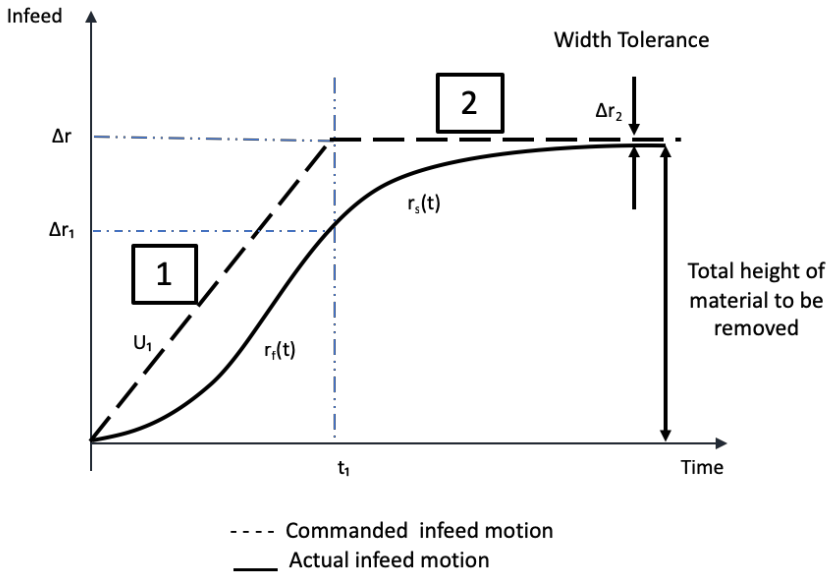

Figure 29: Robotic grinding process cycle.

In the above figure, the difference between the commanded infeed motion and the actual infeed motion is a result of the static deflection of the robot end effector under influence of the normal grinding force. If we assume that the Cartesian stiffness of the end effector in the infeed direction for a particular robot configuration is given by K_R, the static normal force acting on the robot can be written as,

$$F_n = K_R\,(x_{com} - x_{act}) \tag{6}$$

where x_{com} and x_{act} are the commanded and the actual robot end effector positions at any instant. The wheel part-contact is assumed to be rigid. When the part initially makes contact with the rigid wheel the robot deflects elastically to generate a force. Note that although x_{act} is defined as the actual robot end effector position, it is also equal to the height of material removed from the part after initiation of the grinding cycle. Substituting Eq. 6 into Eq. 5 gives,

$$\lambda_w \, K_R \, (x_{com} - x_{act}) = f \, A \tag{7}$$

But since infeed rate, f, is the time derivative of the actual position of the robot or the rate at which the height of the ring is reduced, we can rewrite the above equation as,

$$\lambda_w \, K_R \, (x_{com} - x_{act}) = \dot{x}_{act} \, A \tag{8}$$

The face grinding cycle in Figure 29 is divided into two parts. The first part consists of a constant infeed and while the second has zero infeed and corresponds to the spark-out phase of the grinding cycle. Denoting the initial constant infeed to be U_1, which is the slope of the commanded infeed motion, we can write,

$$x_{com} = U_1 \, t \tag{9}$$

$$\lambda_w \, K_R \, (U_1 t - x_{act}) = \dot{x}_{act} \, A \tag{10}$$

Solving for x_{act} yields the robot's position and the actual height of material removed as a function of time during the first part of the grinding cycle as,

$$x_{act} = U_1(t + \tau\, e^{-\frac{t}{\tau}} - \tau) \tag{11}$$

where,

$$\tau = \frac{A}{\lambda_w\, K_R} \tag{12}$$

Equation 11 describes the path of the robot in the first phase of the grinding cycle i.e. for $t < t_1$. The infeed rate is therefore constant from $t = 0$ to $t = t_1$ and then the commanded infeed is set to zero during the spark-out phase.

The commanded robot position during the spark-out phase ($t > t_1$) can be written as,

$$x_{com} = U_1\, t_1 \tag{13}$$

The initial condition for the spark-out phase can be written as,

$$x_{act}\,(t_1) = U_1\left(t_1 + \tau\, e^{-\frac{t_1}{\tau}} - \tau\right) \tag{14}$$

Integrating Eq. 10 with the above initial condition gives the actual robot end effector position during the spark-out phase of the grinding cycle as,

$$x_{act} = U_1 t_1 - U_1 \tau e^{-\frac{t-t_1}{\tau}}(1 - e^{-\frac{t_1}{\tau}}) \tag{15}$$

The constant τ represents the time constant of the system. The time constant is a key factor in determining the overall cycle time of the process. It also represents the time lag in a first order system, in this case between the actual and commanded positions of the robot end effector. The greater the lag, the more time it takes for the system to settle to a steady state and hence larger the grinding process cycle time. Using the two equations that describe robot's actual trajectory (Eq. 11 and 15), the analytical equation for the process cycle time (T) can be derived as a function of the process parameters as follows,

$$T = t_1 - \tau \ln \frac{\Delta r_2}{U_1 \tau (1 - e^{-\frac{t_1}{\tau}})} \tag{16}$$

Δr_2 in the above equation denotes the width tolerance of the part. The spark-out phase is deemed completed when the actual part width is within the tolerance limit, i.e. Δr_2 is equal to the width tolerance of the part (50 μm).

As discussed in the next chapter, a potential challenge in robotic grinding is the occurrence of robot vibrations due to external forced excitations that can result from part-wheel angular misalignment arising from, for instance, improper dressing. The misalignment of the work-wheel axes causes a time-varying force that in turn can induce vibrations. The grinding wheel thus needs to be chosen to minimize the amount of wear. It is also important to understand the effect of grinding wheel grade on the grinding cycle time and part dimensional accuracy since it affects the material removal parameter and therefore the system time constant and the overall cycle time. Since wheel wear increases with robot infeed, there is a limit on the operating feed rate. Wheel wear is characterized by the grinding ratio, G_r, which is defined as the ratio of the material removal rate and the

wheel wear rate. If the desired grinding cycle time requires operating at a higher infeed rate, then a grinding wheel grade that yields a high G_r ratio must be selected.

The next section discusses the experimental results of the robotic face grinding process. The grinding cycle process model derived in this section is used to estimate the material removal rate and the system time constant. In addition, the effect of the grinding process conditions on the system time constant is analyzed.

4.5 Experimental Results

The experimental setup was described in Chapter 3. The process variables to be studied include the wheel type, wheel speed, and the commanded infeed rate. A fixed configuration of the robot was chosen for all the experiments described here. Two-wheel types – varying in their hardness grades – were selected for investigation and their specifications have been covered in Chapter 3. One is a soft wheel with a hardness grade G while the second wheel is of a harder grade I. The range of wheel speeds were chosen based on safety considerations since the grinding wheel spindle is not fully enclosed. The wheel speed was varied in the range of 1000 to 2600 rpm in increments of 400 rpm. The infeed rate was varied from 10 μm/s to 30 μm/s in steps of 10 μm/s. The workpiece rotation speed is set to 360 rpm. As explained in Chapter 3, the axial payload limit of the rotary chuck holding the bearing ring is approximately 70 N. Although data for higher infeed rates is not reported in this thesis, preliminary experiments revealed that the normal force exceeded the payload limit at infeeds greater than 35 μm/s. The spark-out phase was deemed to be complete when the force magnitude decreased below 5 N at which point the robot end-effector holding the bearing ring was retracted from the grinding wheel surface.

The analog signals from the laser displacement sensor, triaxial accelerometer, and the force/torque sensor were sampled at a rate of 1000 Hz. The frequency contents of the normal grinding force and the triaxial accelerometer signals were analyzed using Fast Fourier Transformation (FFT). The influence of process forces on the vibration characteristics of the robot structure is discussed in Chapter 5. A moving window average of the force data (window size of 0.003 seconds) is used to analyze the quasi-static behavior of the normal force signal during the grinding cycle.

The experimental normal force data is compared with the normal force calculated from the laser displacement data. Equation 6 is used to calculate the normal force profile since the laser sensor tracks the actual displacement of the robot end-effector during the operation and the difference between the commanded infeed and the actual infeed is what gives rise to the normal force. Note that the commanded infeed is known in all cases.

The robot Cartesian stiffness K_R is determined by comparing the measured force data with the force magnitudes calculated using Equation 6. This is repeated for all the experiments and the average K_R value (1.45×10^5 N/m) is used as the static Cartesian robot stiffness to estimate the grinding cycle process parameters, as discussed in the following section. The material removal parameter (λ_w) is estimated from the best fit of the theoretical curve (Equations 11 and 15) to the measured displacement curve. The variation of the material removal parameter with the wheel speed, infeed rate, and wheel grades is analyzed. The system time constant is then derived using the material removal parameter from Equation 12.

Table 2 lists the set of experimental conditions that were selected to study the effect of grinding process parameters.

Table 2: Robotic grinding experimental conditions.

Ring material	Hardened Chrome Steel
Ring dimensions	50 mm bore dia/ 60 mm OD 20 mm width
Coolant type	Trim Sol cutting fluid
Grinding wheel grades	G and I
Wheel rotation speed (RPM)	1000, 1400. 1800, 2200, 2600
Part rotation speed (RPM)	360 ± 15 (5%)
Robot infeed rate (μm/s)	10, 20, 30

The dashed curve in Figure 29 shows the commanded displacement of the robot end effector in the infeed direction while the solid curve shows the measured displacement. The desired amount of bearing ring width to be ground is fixed in each case to be 1 mm. The robot controller is programmed to feed the bearing ring into the grinding wheel along a ramp input corresponding to the nominal travel distance required to achieve the desired

width reduction followed by a spark-out phase where the robot infeed is stopped. The spark-out phase removes material not removed during the ramp input phase because of elastic deformation of the system. The dashed curve in Figure 29 shows the time instant the infeed is stopped and the spark-out phase starts. It can be seen from the measured displacement signal that the system behaves like a first order system in that a ramp input produces a steady state after a fixed lag, which represents the time constant of the system. Once the infeed is stopped, the system exponentially converges to the target value. The time constant thus affects both the actual infeed (roughing) and the spark-out (finishing) phases. The normal force curve can be explained using the theoretical law derived earlier. The difference between the commanded displacement trajectory (dashed curve) and the actual trajectory (solid curve) represents the elastic deformation of the robot system. Since the robot is treated as a linear spring, the normal force in Equation 6 is what the force sensor measures. We can clearly see that as time progresses, the time lag initially starts increasing and causes the force to rise. As the system tries to attain steady state, the slope of the actual displacement profile approaches the slope of the commanded profile. At the time instant the robot infeed is stopped, the lag between the actual and commanded displacement profiles starts to decrease, which is why the force also starts to decrease after reaching a maximum. The data acquisition was stopped once the force magnitude reached the threshold defined earlier (5 N).

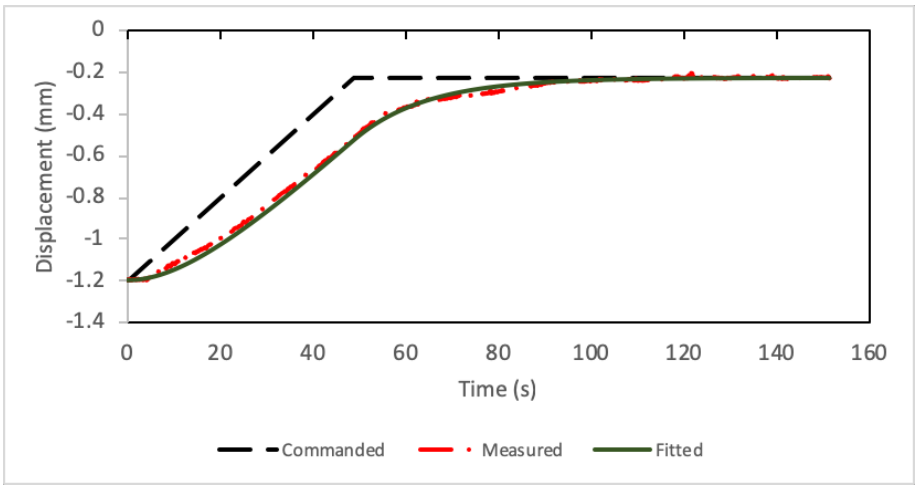

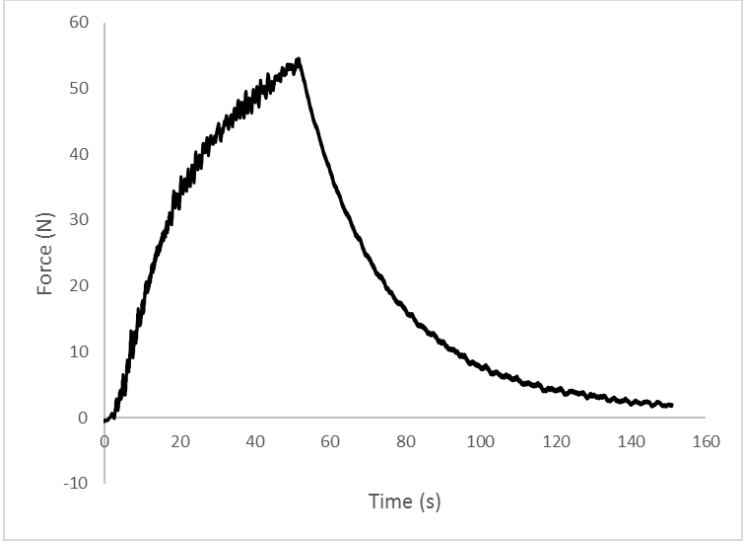

Figure 30: Robot end effector displacement and normal force plots for feed = 20 µm/s, wheel speed = 1000 rpm, workpiece speed = 360 rpm, wheel grade = I.

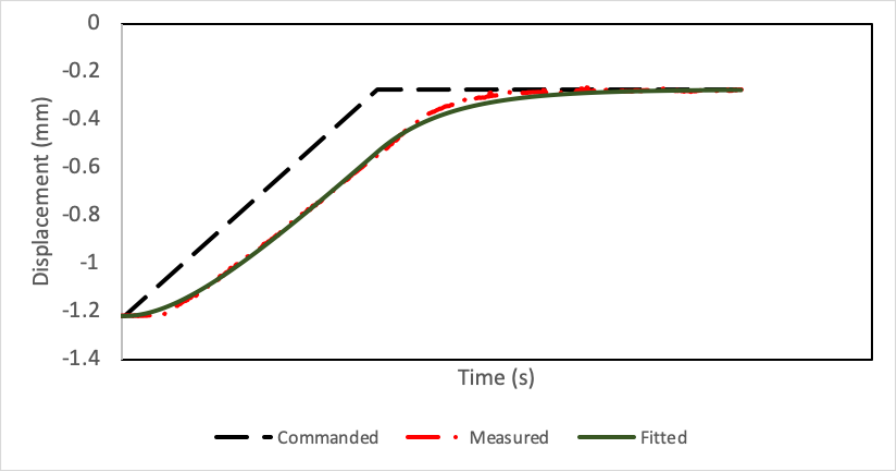

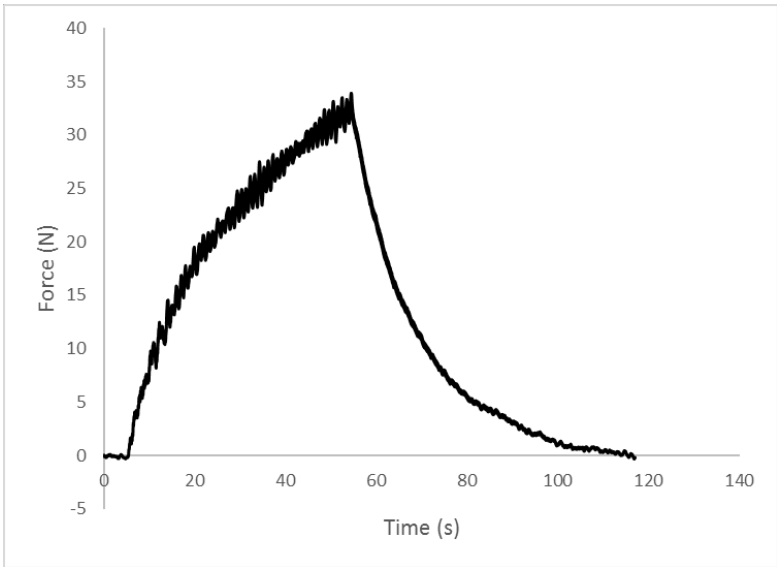

Figure 31: Robot end effector displacement and normal force plots for feed = 20 µm/s, wheel speed = 2200 rpm, workpiece speed = 360 rpm, wheel grade = I.

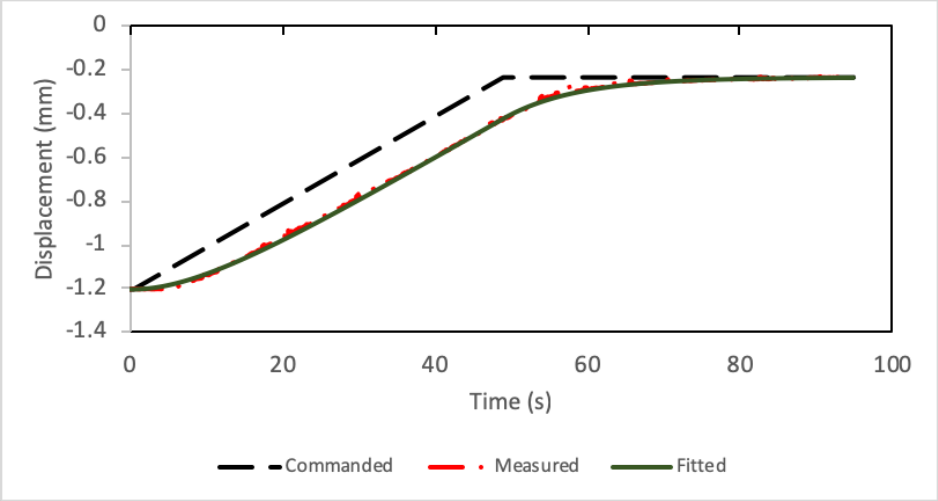

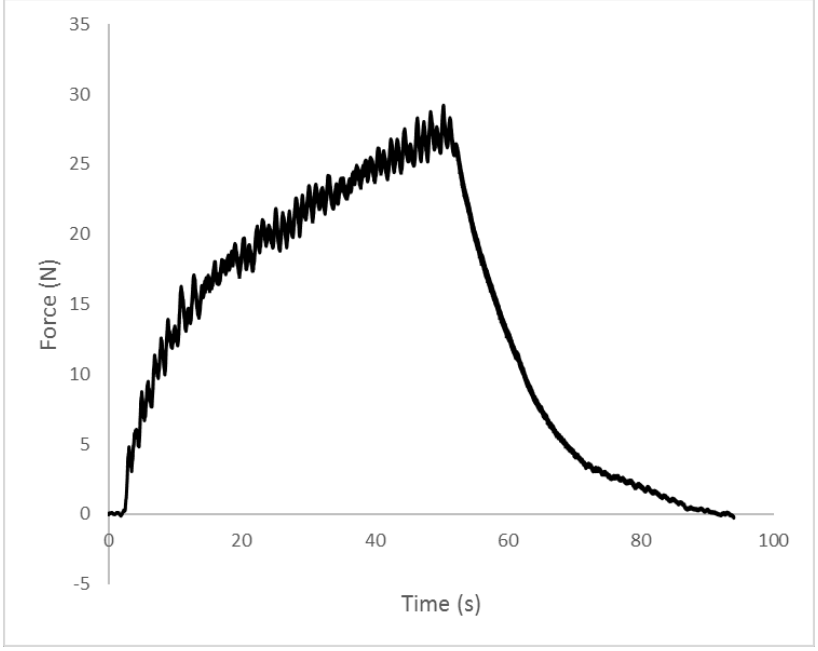

Figure 32: Robot end effector displacement and normal force plots for feed = 20 µm/s, wheel speed = 2600 rpm, workpiece speed = 360 rpm, wheel grade = I.

4.6 Discussion

This section discusses the useful insights obtained from the analysis of the experimental results. The following quantities are derived from the experimental data and the effects of process conditions on these quantities are analyzed:

1. Material removal parameter
2. Total cycle time
3. System time constant

The fitted robot displacement profiles (solid curve) in Figure 30, Figure 31, and Figure 32 are derived using values of the material removal parameter that best fit the theoretical models (Equations 11 and 15) to the measured displacement data. The goodness of fit estimated using the 'coefficient of determination' or R^2 values for each of the 30 experiments is plotted in Figure 33. In each case R^2 values greater than 0.98 were obtained.

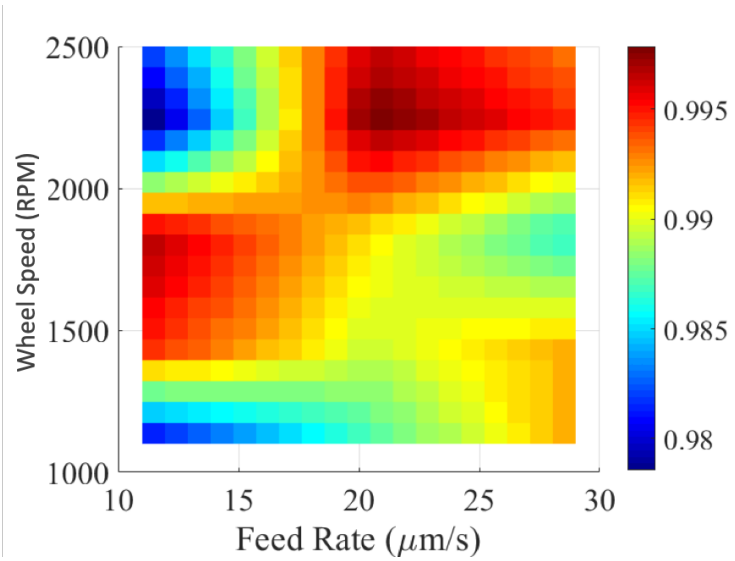

Figure 33: R^2 values for the model fits.

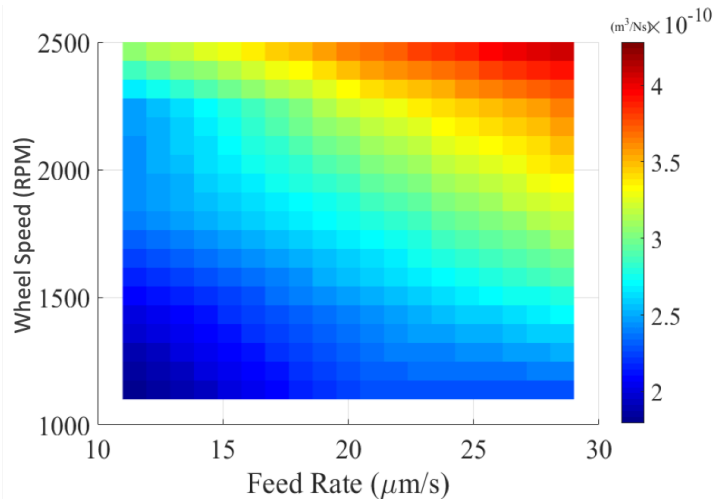

Figure 34: Material Removal Parameter (λ_w) for different infeeds and wheel speeds.

As seen in Figure 34, the material removal parameter is found to increase with the wheel speed and infeed rate. As discussed earlier, Hahn and Lindsay [37] also showed a

similar behavior of the material removal parameter as a function of the wheel speed and feed rate in cylindrical plunge grinding. The material removal parameter values determined using a subset of the data are validated by predicting their values for the rest of the measured data. Specifically, the material removal parameter values for robot feed rates of 10 and 30 μm/s and wheel rotation speeds of 1000 to 2600 rpm for wheel grades G and I are known from the fitted displacement curves. This data is used to derive an empirical model of the material removal parameter as a function of the process parameters for both the wheel grades as follows.

$$\lambda_w = p_{00} + p_{01} f + p_{02} \Omega \tag{17}$$

where f is the feed rate in μm/s and Ω is wheel rotation speed in RPM. The values of the model coefficients determined from data fitting are listed in Table 3 below for the two different wheel grades.

Table 3: Material removal parameter model coefficients.

Wheel Grade	$p_{00} * 10^{-11}$	$p_{01} * 10^{-12}$	$p_{02} * 10^{-13}$
G	1.729	0.279	1.799
I	-2.901	4.657	1.218

Using these equations, the corresponding values for the material removal parameter at feed rate of 20 μm/s and wheel rotation speeds ranging from 1000 to 2600 rpm were predicted

for both the wheel grades. The predicted and fitted numbers (see Figure 35and Figure 36) are compared to get R^2 values of 0.93 and 0.94 for the two wheel grades.

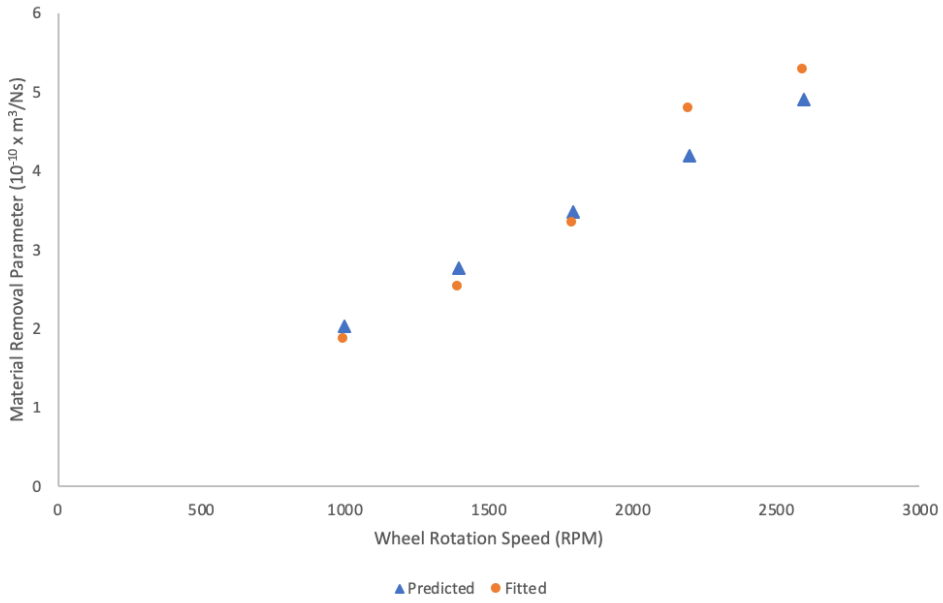

Figure 35: Comparison of fitted and predicted material removal parameter values for feed rate = 20 μm/s, wheel grade = G.

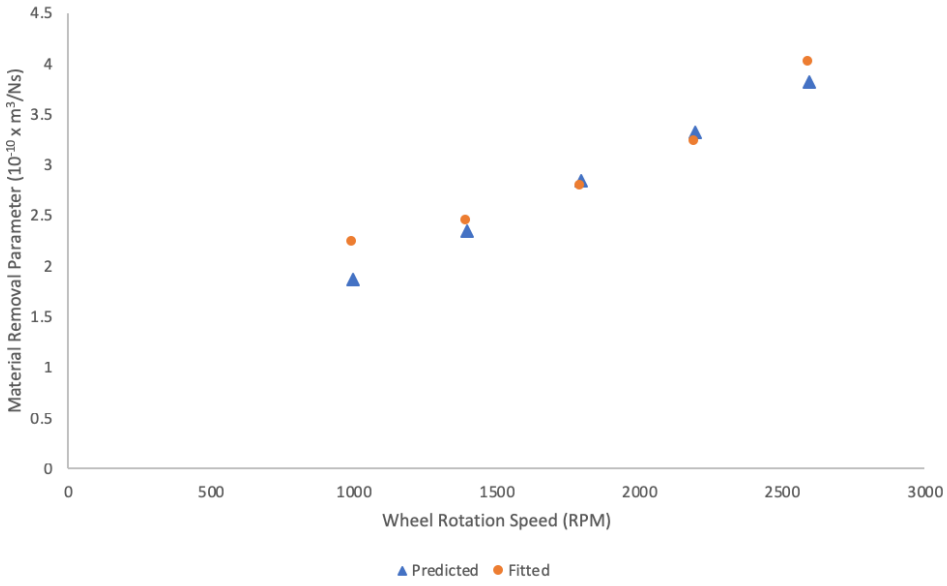

Figure 36: Comparison of fitted and predicted material removal parameter values for feed rate = 20 μm/s, wheel grade = I.

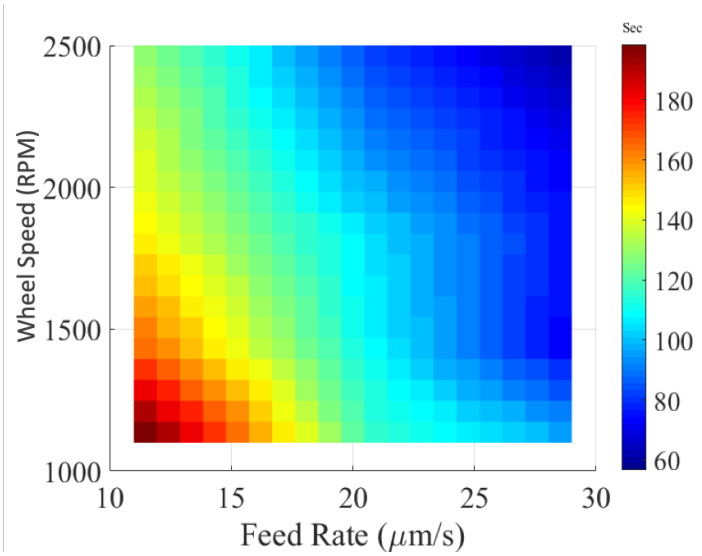

Figure 37: Grinding cycle time for different infeed rates and wheel speeds.

The total cycle time is an important quantity as it determines the productivity of the process. Because of the robot's lower stiffness (compared to a CNC grinding machines),

the total cycle time is expected to be higher compared to CNC grinding machines. Hence, it is critical to study how the system behaves when the process conditions are varied. The total grinding cycle time was calculated using Equation 16. It can be clearly seen in Figure 37 that as the wheel speed is increased at a fixed infeed rate, the total cycle time decreases. This is because the higher wheel speed corresponds to an increase in the material removal parameter, which lowers the system time constant. Referring back to Figure 29, the actual robot trajectory lags behind the commanded trajectory by a factor that is dependent on the system time constant. Consequently, the reduction in the time constant lowers the overall cycle time for the process.

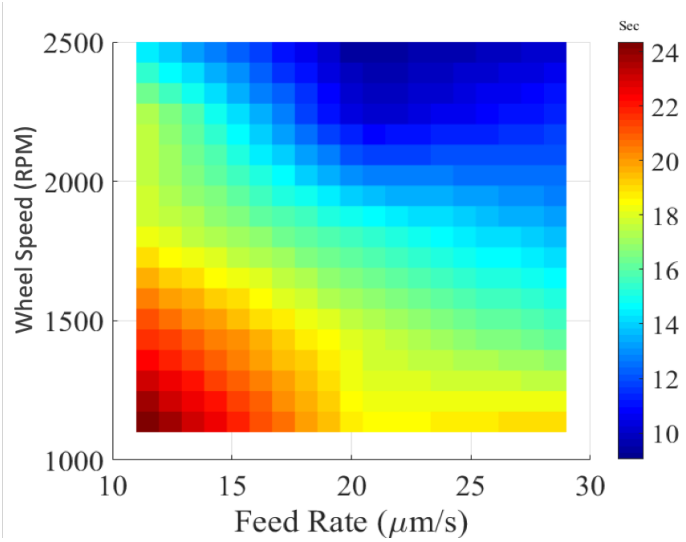

Figure 38: System time constant for different infeed rates and wheel speeds.

First order systems are characterized by their time constants. The time constant characterizes the system's time domain responses to step, impulse, or periodic inputs. It represents the time required for the system to respond to a change, typically equal to the

time taken for a specific parameter to vary by 63%. Since we are dealing with a ramp input response, it is important to know the time required for the system to reach steady state. The time constant of the robotic grinding system affects the total cycle time that includes both initial infeed phase and the spark-out phase. As expected from the theoretical analysis presented in this chapter, the time constant is inversely proportional to material removal parameter (Equation 12). The material removal parameter that in turn has a proportional relation to wheel speed, hence giving an inverse relation between time constant and wheel speed.

It is obvious that in order to grind a fixed amount of material in minimum time, the infeed rate must be maximum. But practically, higher the infeed rate, greater the maximum normal force and larger the elastic deformation of the system, causes a larger overall grinding cycle time. Since the experimental setup in the present work is limited by the maximum load the chuck motor can withstand (70 N), the maximum permissible force is limited. An experiment at an infeed rate of 40 μm/s was conducted but it resulted in a normal force greater than 70 N. Using a higher torque motor would mean an increase in the size and weight of the motor, which is again limited by the maximum payload capacity of the robot. Thus, a higher payload robot is required to face grind at higher infeed rates.

The theoretical analysis showed that the time constant must be reduced to lower the total cycle time. Looking at the experimental data and the theoretical model (Equations 11 and 15) it can be concluded that to minimize the face grinding process cycle time the Cartesian stiffness in the direction normal to the grinding wheel surface must be maximized and a practically achievable maximum wheel speed must be used. Considering the robot Cartesian stiffness, it can be maximized by choosing an optimal configuration of the robot.

In the present study, the position and orientation of the grinding spindle could not be easily modified to enable an experimental investigation of the effect of robot configuration on the Cartesian stiffness. This aspect has been investigated in Chapter 6 through simulation. The grinding wheel spindle in the experimental setup had no safety enclosure and thus it couldn't be operated at higher speeds. However, this is a solvable problem from an industrial application perspective. Finally, operating at higher infeed rates, and hence higher forces, also requires that the G_r must be higher. Since a small misalignment between the part and wheel surfaces is unavoidable in robotic face grinding, it can lead to uneven wheel wear, which in turn can cause undesirable vibrations. Hence, it is best to utilize a grinding wheel with higher hardness.

4.7 Summary

The results of this chapter shed new light on the effects of the following robotic face grinding process variables and quantities on the overall system performance:

1. Robotic Cartesian stiffness
2. Grinding wheel speed
3. Material removal parameter
4. Wheel hardness
5. Robot infeed rate

It was found that the material removal parameter increases with wheel speed, similar to the findings of Hahn and Lindsay [34] for cylindrical plunge grinding. The time constant of the robotic grinding system affects the total cycle time that includes both initial infeed

phase and the spark-out phase. The system time constant is found to decrease with increase in the wheel speed and robot infeed rate. With the knowledge derived from this study, it is possible to determine the robot specifications (e.g. payload and Cartesian stiffness), the face grinding process parameters, and the grinding wheel specifications required to achieve the desired grinding process cycle time. For instance, the robot's payload capacity can be determined from the theoretical process model, which can be used to estimate the maximum normal force expected during the face grinding operation. Similarly, the required Cartesian stiffness of the robot can be determined since the material removal parameter is dependent on the robot's Cartesian stiffness, which in turn is pose dependent. Thus it is possible to determine the material removal parameter from the desired grinding cycle time, and then estimate the Cartesian stiffness through its dependence on material removal parameter and select the robot configuration (pose) accordingly.

CHAPTER 5. PART QUALITY IN ROBOTIC FACE GRINDING

5.1 Introduction

This chapter investigates the vibration characteristics and its effect on the resulting part quality in robotic face grinding. The last chapter dealt with understanding the relationship between the normal force acting on the robot during the face grinding operation and the material removal rate, and the effects of different grinding process conditions on the system time constant and grinding cycle time. In the present chapter, the dynamic components of the measured normal force and displacements are investigated by analyzing the frequency contents of the external forcing function (grinding force) and the resultant displacements of the robot end-effector. Chapter 3 discussed the robot's natural vibration modes using impact hammer tests in the three orthogonal directions. In this chapter, it is of interest to determine if the dynamic component of the grinding force excites the natural frequencies of the robot by looking for their presence in the frequency spectrum of the measured displacement signal. The misalignment of the ring face with respect to the wheel results in uneven material removal from the face of the bearing ring that produces errors in the flatness of the ring face and a rougher surface finish.

Grinding the two parallel faces of the ring is an important step in bearing manufacture. Since the two ring faces act as datums for the rest of the bearing manufacturing process, it is important to achieve the required flatness, parallelism, and surface roughness of these faces.

Face grinding is generally carried out via double disk grinding which involves two rotating wheels contacting the ring on the two opposite faces. In the robotic face grinding process investigated in this thesis, a bearing inner ring is held in a rotating chuck, which is fixed to the robot's end effector. Accurate alignment of the ring's face parallel to the grinding wheel's surface is critical because even small angular alignment errors can produce uneven contact between the ring face and the wheel, resulting in poor surface flatness and surface finish. Alignment challenges arise from the fact that it is difficult to find easy and inexpensive techniques to accurately measure (on the order of microns) the alignment of the bearing ring face relative to the wheel surface. This chapter deals with analysis of the frequency content of the robot end-of-arm displacement using accelerometer and the normal force using 6-axis force dynamometer. The chapter also evaluates the ground surface properties like flatness, parallelism, and surface roughness of the ring face. Finally, to overcome the challenges associated with vibration and part angular misalignment, a novel flexible insert gripper is designed, fabricated, and experimentally evaluated.

5.2 Analysis of Force and Vibration Signals

A study of the robotic face grinding process vibration characteristics is conducted through analysis of the frequency contents of the normal force and acceleration of the robot's end-effector using the Fast Fourier Transform (FFT). As explained in Chapter 4, the forces generated by the grinding action at part-wheel interface are measured using a force/torque sensor (ATI Omega 85) while the vibration is measured using a tri-axial accelerometer (PCB SN 163555) mounted on the robot end-effector, as shown in Figure 39. The normal force and acceleration data analyzed here were obtained under

experimental conditions listed in Table 2 of Chapter 4. The analysis considers the force components measured in all three directions (X_G, Y_G and Z_G) since the resultant grinding force is a three-dimensional vector.

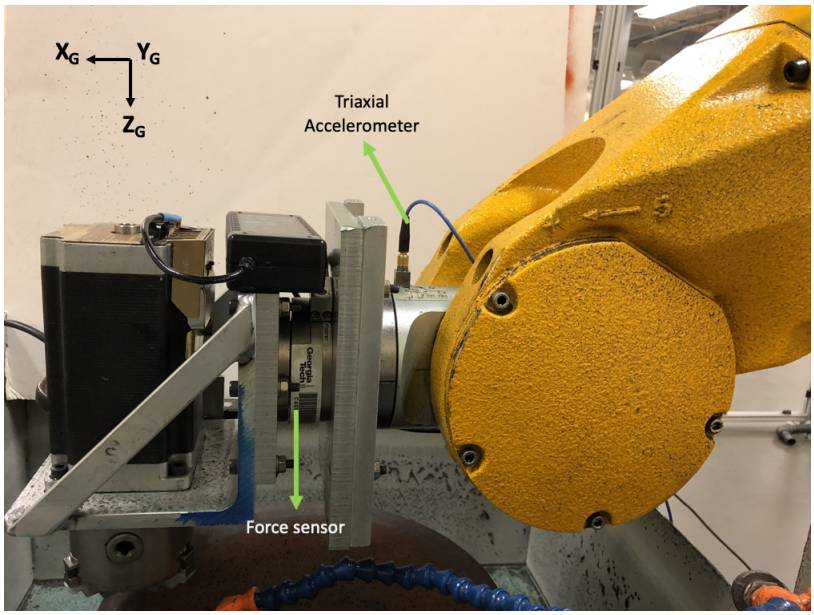

Figure 39: Robotic grinding end-effector.

For the force and acceleration FFT's, the magnitudes of the frequency peaks are normalized with respect to the maximum peak in the corresponding spectrum. For analysis purposes, the frequency range considered is limited to 0-100 Hz because it is observed that no major peaks are present in the acceleration and force signal beyond 100 Hz. The FFTs of the force and acceleration signals for wheel speeds of 1000 and 2600 RPM in the three orthogonal directions of the robot's frame of reference have been plotted in Figure 40-Figure 45. The peaks in force and acceleration FFT in each case can be categorized as either arising due to chuck motor's rotation or grinding wheel rotation. The part rotation

speed is fixed at 360 rpm. Note that the part rotation speed has a nominal value of 360 rpm with a tolerance of ±5% (See Table 2). The 6.2 Hz that appears in the FFT is thus attributed to the part rotation speed. The peaks in force FFT appear to be due to the part rotation (6.2 Hz) and its harmonics (12.2 Hz and 18.4 Hz), and due to the wheel rotation at 16.6, 33 and 50 Hz for 1000 rpm case (see Figure 40-Figure 42) and at 42 and 84 Hz for 2600 rpm case (see Figure 43-Figure 45). The acceleration FFT shows a similar trend with peaks appearing at the harmonics of the wheel and part rotation speeds. Apart from the frequencies corresponding to the wheel and part rotation speeds and their harmonics, no other peaks are observed in any of the experiments except for the 1800 rpm case (see appendix), where a peak at 9 Hz, which is near the natural resonant mode of the robot (see Figure 22), is present. Table 4 lists the dominant frequencies in the spectra and their sources.

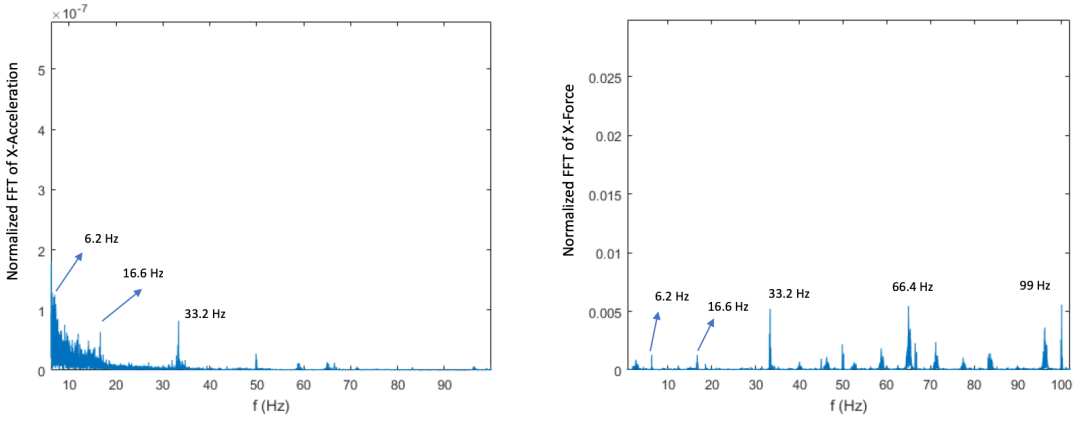

Figure 40: FFTs of acceleration signal (left) and force signal (right) in the X_G direction; feed = 20 µm/s, wheel speed = 1000 rpm, wheel hardness grade = I.

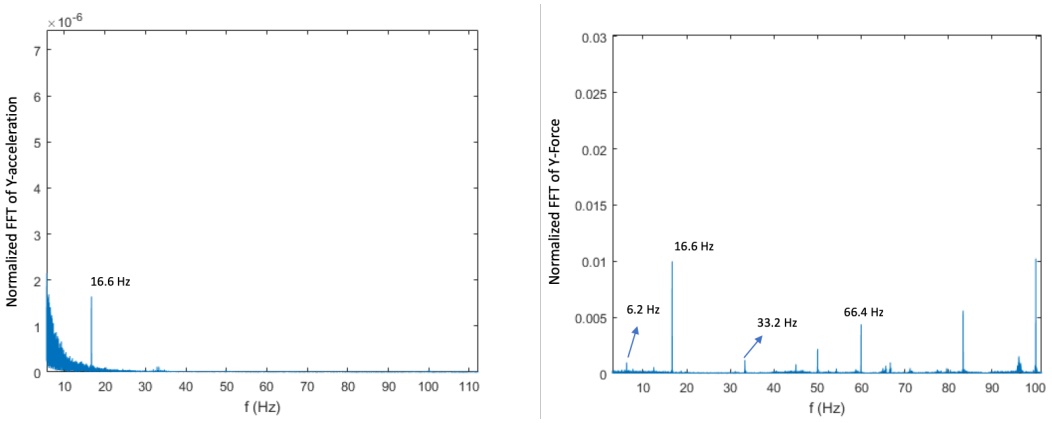

Figure 41: FFTs of acceleration signal (left) and force signal (right) in the Y_G direction; feed = 20 µm/s, wheel speed = 1000 rpm, wheel hardness grade = I.

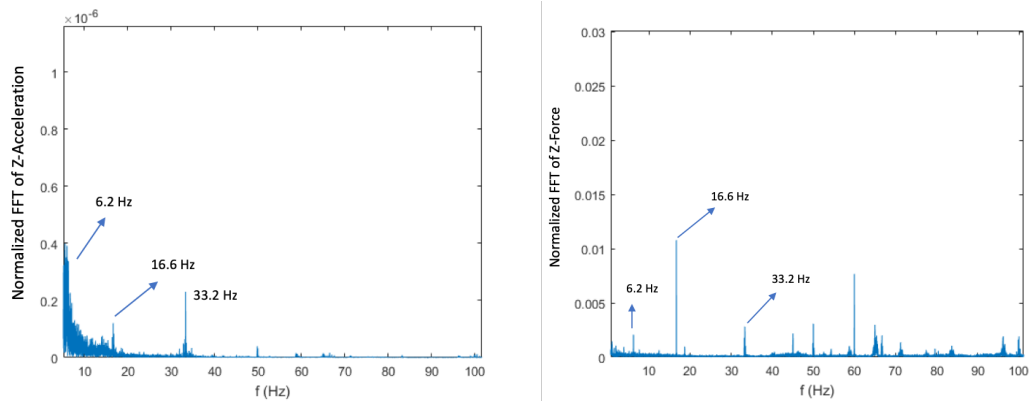

Figure 42: FFTs of acceleration signal (left) and force signal (right) in the Z_G direction; feed = 20 µm/s, wheel speed = 1000 rpm, wheel hardness grade = I.

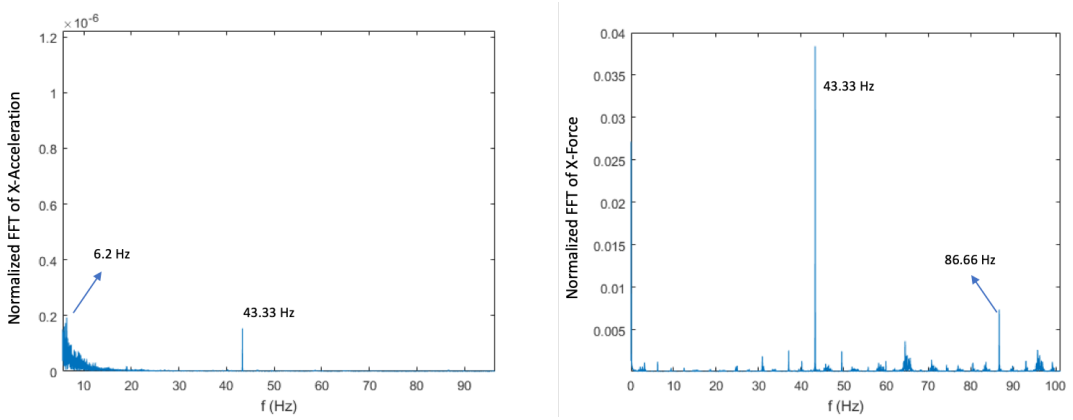

Figure 43: FFTs of acceleration signal (left) and force signal (right) in the X_G direction; feed = 20 µm/s, wheel speed = 2600 rpm, wheel hardness grade = I.

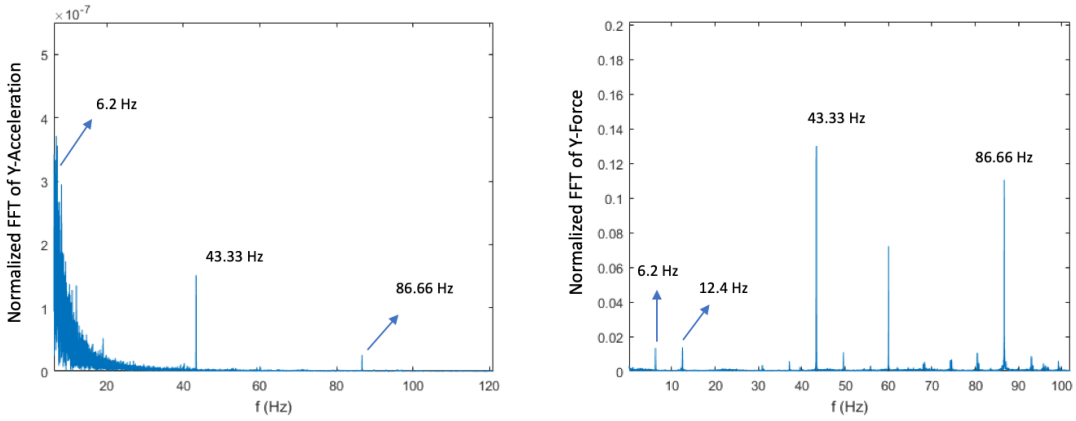

Figure 44: FFTs of acceleration signal (left) and force signal (right) in the Y_G direction; feed = 20 µm/s, wheel speed = 2600 rpm, wheel hardness grade = I.

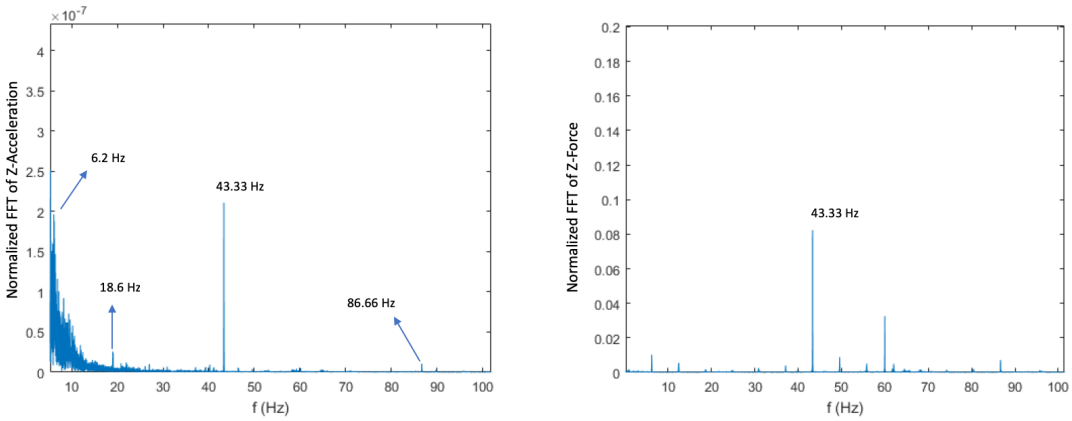

Figure 45: FFTs of acceleration signal (left) and force signal (right) in the Z_G direction; feed = 20 µm/s, wheel speed = 2600 rpm, wheel hardness grade = I.

Table 4: Dominant peaks in the force and acceleration FFTs.

Wheel Speed (rpm)	Major Peaks (Hz)	Source
1000	6.2, 12.4, 18.4	Part rotation
	16.6, 33, 50	Wheel rotation
1400	6.2, 12.4, 18.4	Part rotation
	23.3, 46.6	Wheel rotation
1800	6.2, 12.4, 18.4	Part rotation
	30, 60	Wheel rotation
2200	6.2, 12.4, 18.4	Part rotation
	36.66, 73.2	Wheel rotation
2600	6.2, 12.4, 18.4	Part rotation
	42, 84	Wheel rotation

It can be seen from Figure 40-Figure 45 that the dominant peaks occur at the fundamental frequencies and harmonics of the wheel and part rotation frequencies. We can see that the natural vibration frequencies of the robot reported in Chapter 3 are not present in any of the cases discussed except in the case of 1800 RPM, where a peak at 9 Hz is observed in the acceleration FFT, the reason for which is not conclusively understood.

5.3 Part Accuracy

The surface flatness, parallelism, and surface roughness of the ground faces are important outputs of the robotic face grinding process. These three measures of part quality are defined as follows:

1. **Flatness**: The flatness tolerance refers to the width of the zone between two parallel planes between which the reference surface lies. This definition follows from ISO 12781-1:2011 [101].

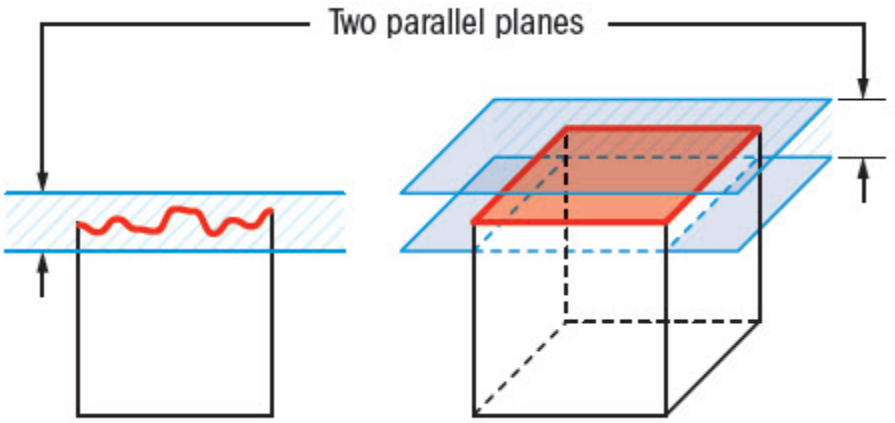

Figure 46: Flatness definition [102].

2. **Parallelism**: Per ISO 1101:2017 [103], the surface parallelism is a form tolerance that is controlled by a tolerance zone defined by two parallel planes, which are oriented parallel to the datum feature or surface, as shown in Figure 47.

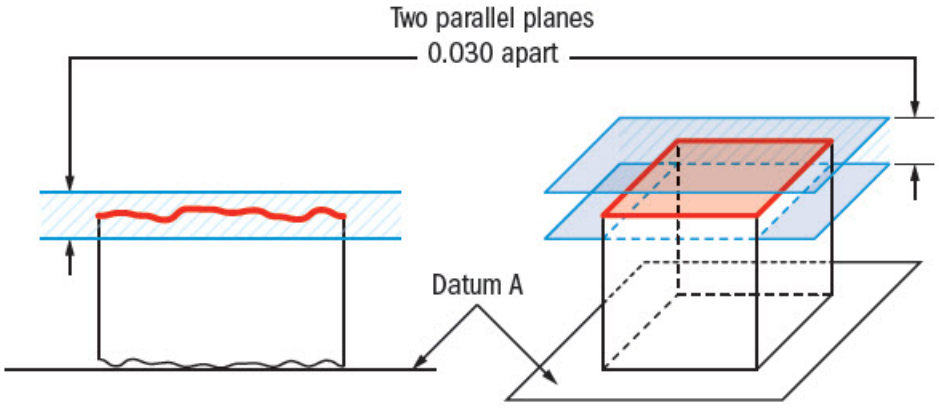

Figure 47: Parallelism definition [104].

3. **Surface roughness**: This is quantified by the deviations in the direction of the normal vector of a real surface from its ideal form. There are many different roughness parameters in use, but the areal arithmetic average surface roughness, S_a, is the most common and is used here.

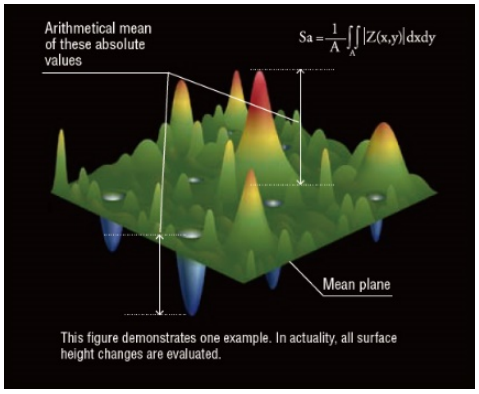

Figure 48: Surface roughness S_a definition [105].

The flatness and parallelism were measured with a Zeiss Coordinate Measuring Machine (CMM) (Zeiss Micura). Figure 49 shows the fixture used to hold the part during measurement.

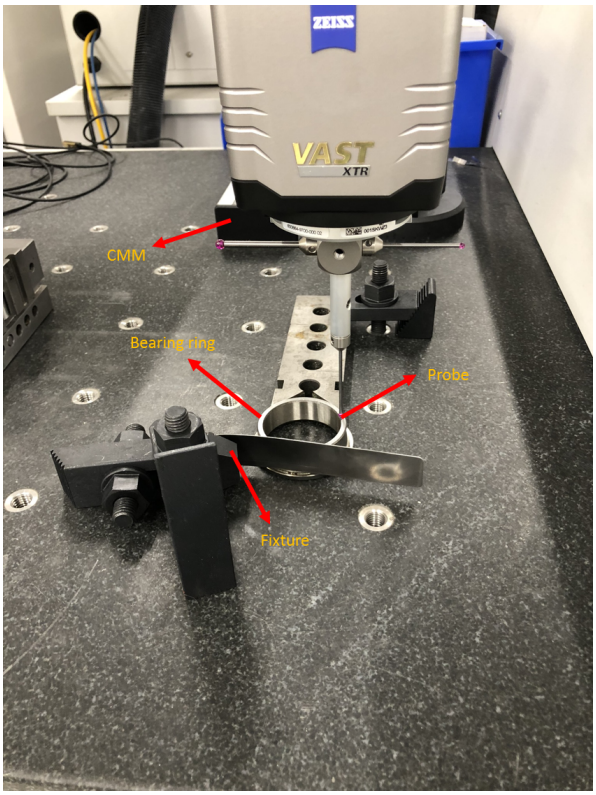

Figure 49: CMM fixture for measuring surface flatness and parallelism.

The surface roughness was measured using a white light scanning interferometer-based instrument (Zygo Zegage). The software scans the surface and measures the roughness parameters such as S_a, S_q and S_z.

Table 5 lists the measured flatness, parallelism, and surface roughness parameter values obtained in the face grinding experiments.

Table 5: Face grinding part quality measurements.

Wheel Speed (rpm)	Feed Rate (μm/s)	Flatness (μm)	Parallelism (μm)	Surface Roughness S_a (μm)
1000	10	11.3	55.99	0.481
1800	10	10.3	86.44	0.393
2600	10	12.2	67.55	0.508
1000	20	10.2	72.8	0.442
1800	20	9.6	85.31	0.480
2600	20	12.5	44.82	0.554

Examination of the part quality results presented in Table 5 shows that there is no clear trend in the flatness, parallelism, and surface finish measurements as a function of the face grinding process conditions. In addition, the measured values are generally higher than the desired values for high precision bearing rings (< 10 μm for flatness, < 15 μm for parallelism, and < 0.1 μm for surface roughness). This fact motivates the investigation of the novel flexible gripper inserts discussed next.

5.4 Flexible Gripper Inserts

As pointed out earlier, a challenge in robotic face grinding is the potential angular misalignment of the part face relative to the grinding wheel surface at the start of the grinding cycle, as illustrated in Figure 50. This misalignment causes a variation in the contact force at the part-wheel interface that leads to vibration and poor quality. Thus, a

method to minimize or eliminate the misalignment is required. Hence, the idea of a flexible part gripper is proposed to minimize the part misalignment error.

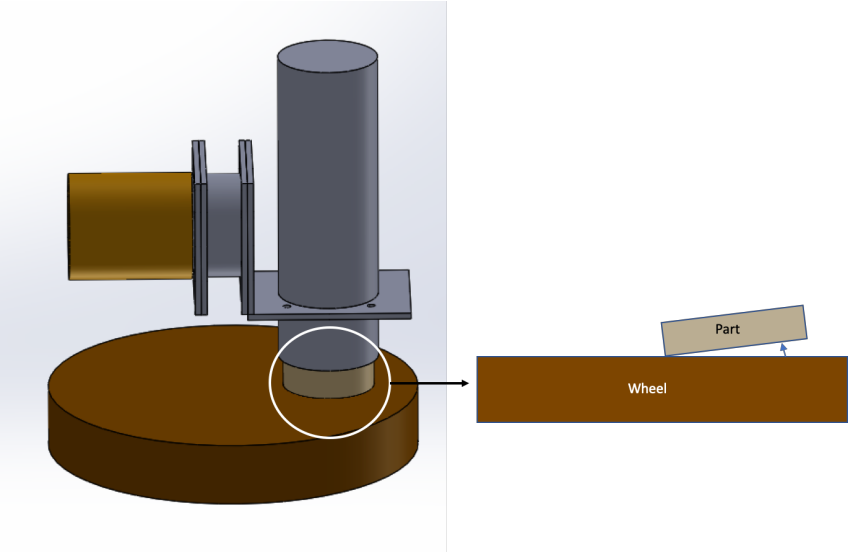

Figure 50: Illustration of the part-wheel angular misalignment.

The flexible gripper insert design and its optimization is discussed first, followed by a description of the modified experimental setup for workpiece fixturing. The resulting improvements in the part quality rare then evaluated through robotic face grinding experiments utilizing the optimized flexible gripper inserts.

The flexible part gripper consists of compliant inserts (see Figure 51) that can be inserted onto the chuck jaws, as shown in Figure 52. Note that the ring-shaped part is held in the chuck jaws and is fed into the wheel along the Z_G-axis. Figure 53 shows a bearing ring held in the chuck jaws with flexible gripper inserts and in contact with the grinding wheel.

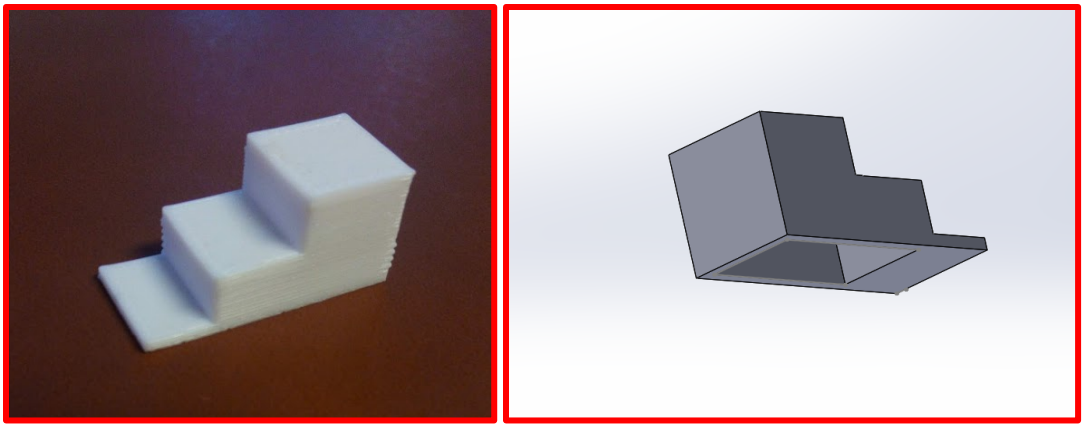

Figure 51: Flexible gripper insert.

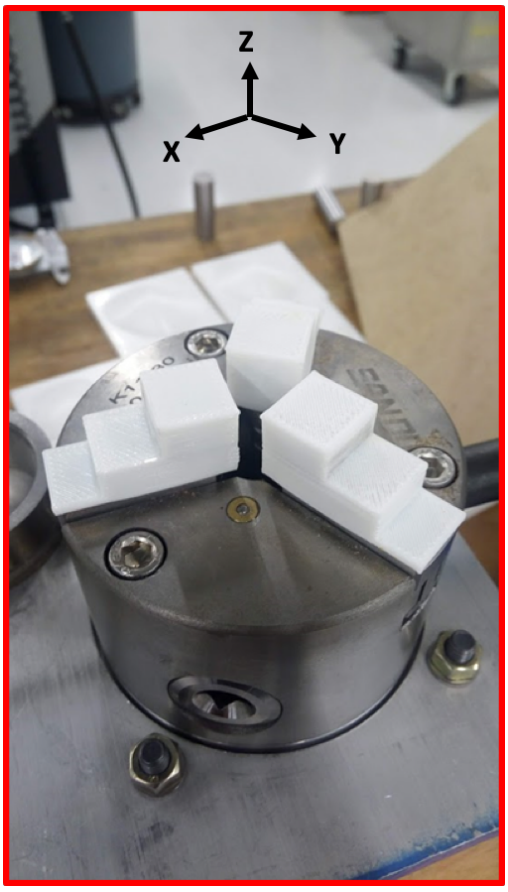

Figure 52: Flexible gripper inserts mounted on rotary chuck jaws (robot end-effector frame X, Y, Z).

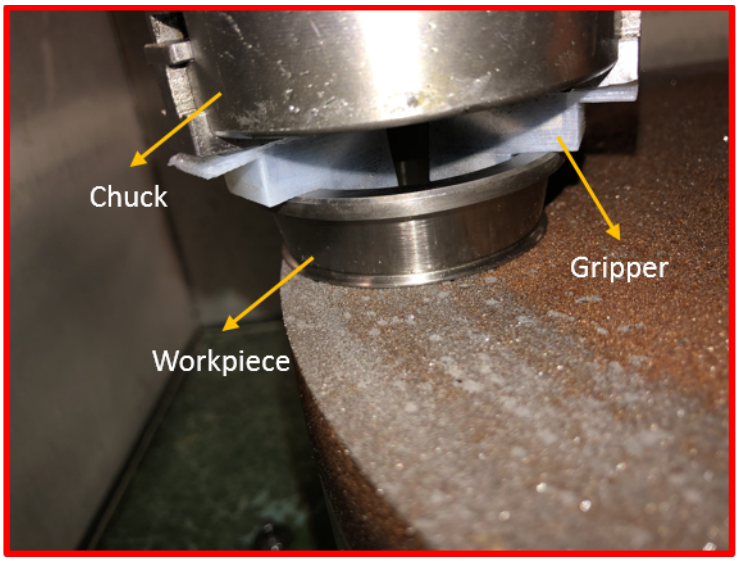

Figure 53: Flexible gripper with bearing ring face in contact with the grinding wheel.

5.5 Flexible Gripper Insert Design and Optimization

This section discusses the design and optimization of the flexible gripper insert. As shown in Figure 54, the thicknesses of the insert faces where the inner race and the bottom face of the bearing ring make contact with the flexible gripper insert, are denoted by h_1 and h_2, respectively. Note that the gripper coordinate frame (X_g, Y_g, Z_g) differs from the robot base reference frame (X_G, Y_G, Z_G) and the robot end-of-arm tooling frame (X, Y, Z) because the gripper and the chuck jaws are rotating while the robot frame is stationary. The X_g-direction in Figure 54 always points in the direction of robot's Z-axis (end-of-arm tooling frame), which is also the direction of part infeed. The following analysis considers the coordinate frame attached to the gripper (X_g, Y_g, Z_g).

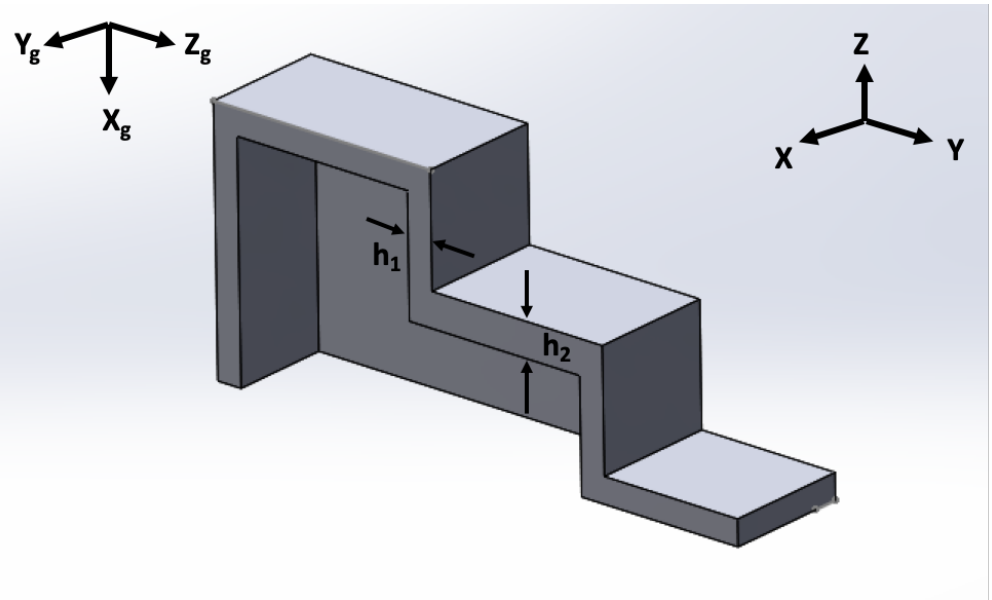

Figure 54: Cross-sectional view of the flexible gripper showing key design dimensions h_1 and h_2.

The dimensions h_1 and h_2 need to be optimized to meet the following design objectives:

1. The stiffness of the flexible gripper in the X_g-direction must be minimum.
2. The stiffness of the flexible gripper in the Y_g-direction must be maximum.

Looking at Figure 52 and Figure 53, the stiffness of the gripper in the robot's Z direction (which corresponds to the flexible gripper insert X_g direction) must be minimized in order to compensate for the wheel-part angular misalignment and the instantaneous displacements of the part due to vibrations during grinding. To understand the effect of the gripper stiffness on the combined (or equivalent) stiffness of the robot and gripper stiffness in the infeed direction, consider the case of two springs in series. Let K_1 and K_2 denote the gripper and robot stiffnesses, respectively, in series. The equivalent series stiffness is given by,

$$K_{eq} = \frac{K_1 K_2}{K_1 + K_2} \tag{18}$$

If we assume $K_1 \sim 0.1 * K_2$, then,

$$K_{eq} = \frac{10K_1^2}{11K_1} = 0.9K_1 \tag{19}$$

which is nearly equal to the gripper stiffness. Thus, the design requirement is that the gripper stiffness be less than or equal to nearly ten times the robot Cartesian stiffness in the robot's Z-direction.

In addition, the flexible gripper insert must support the grinding torque without undergoing excessive twist (or shear). The only geometric constraint in the Z_g-direction of the gripper frame is that the dimension h_1 should be sufficiently large to absorb the maximum elastic deformation of the gripper insert wall caused by the clamping force. This point is considered later in the optimization phase.

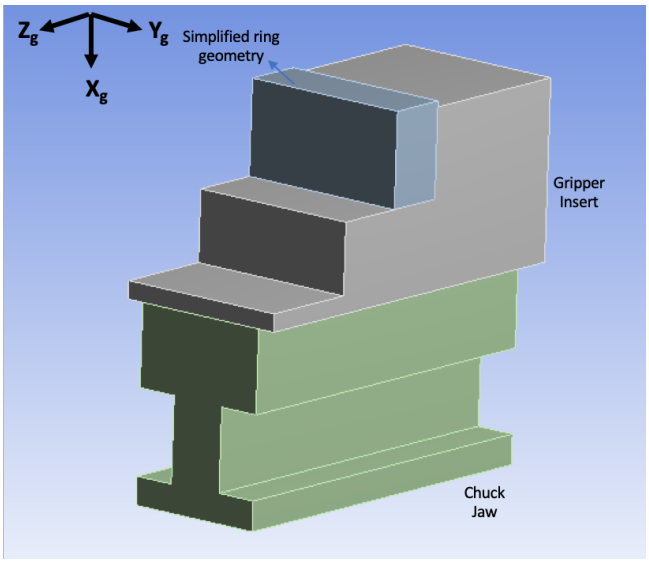

Figure 55: Flexible gripper and chuck geometry utilized in finite element analysis.

The model setup for finite element analysis of the flexible gripper design and its optimization is shown in Figure 55. Since the bearing ring diameter is large compared to the width of the chuck jaws, the curvature of the outer diameter of the ring is neglected and the contact area between the flexible gripper insert and the ring is assumed to be rectangular.

Since the jaw is rigidly fixed to the chuck, analysis of the gripper stiffness is done using a fixed support at the bottom of the jaw. Gripper stiffness is estimated as the ratio of reaction force at the fixed support divided by the input displacement provided at the ring. Fixed support is necessary to determine the reaction forces produced by the displacement of the part due to the grinding force.

The details of the finite element model including the element type, mesh size, step size, and other analysis settings are given in Table 6.

Table 6: Mesh properties in FEM simulation.

Property	Value
Flexible gripper volume	1.91E-6 m^3
Total mesh nodes	51004
Total elements	25392
Mesh size function	Adaptive
Mesh span angle center	Fine
Mesh relevance center	Fine
Transition ratio	0.272
Growth rate	1.2
Maximum layers	5

The gripper material data used for the analysis is listed in Table 7. The gripper material used for prototyping is Smooth-On Ecoflex 00-30 Super Soft Platinum Silicone (See section 5.6 for details).

Table 7: Flexible gripper material properties.

Material property	Value
Young's Modulus	0.337 MPa
Poisson's ratio	0.44
Specific gravity	1070 N/m^3
Tensile strength	3.79 MPa

In order to evaluate the stiffness of the gripper in each orthogonal direction (of the gripper frame of reference), the reaction force is calculated at the bottom face of the jaw, which is fully constrained. The model is shown in Figure 56 and explained in the following paragraph.

Displacement inputs of 1 mm (in 20 steps) are given to the workpiece in each orthogonal direction and the resultant force at the fixed support is simulated. Note that only static analyses are carried out. The stiffness evaluation is done by considering the ratio of the reaction forces that are generated at the fixed support and the input displacement provided on the ring (See d_x, d_y and d_z in Figure 56). These simulations are repeated for multiple sets of gripper insert design dimensions h_1 and h_2 in order to analyze the stiffness of the gripper as a function of the dimensions. Table 8 lists the sets of gripper design dimensions investigated in the simulation study.

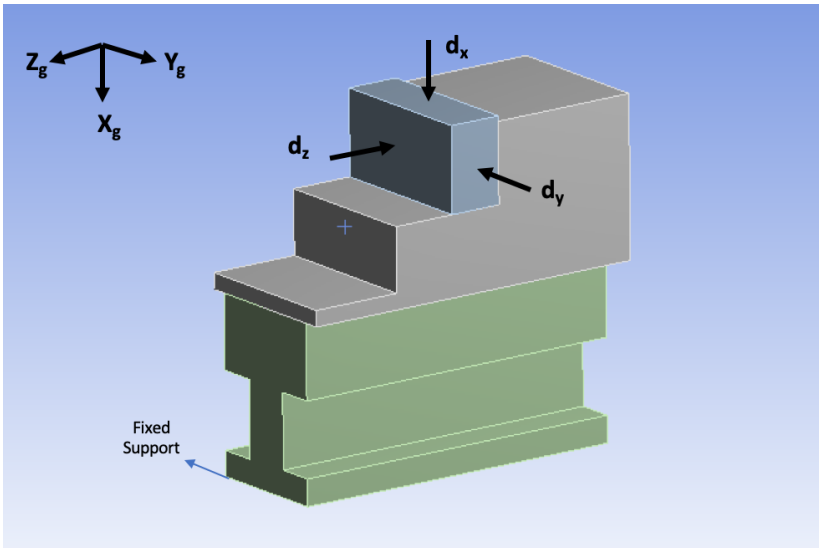

Figure 56: Displacement inputs to the ring/part in the X_g, Y_g and Z_g directions.

Figure 57-Figure 59 show representative simulation results for a particular case.

Table 8: Simulated gripper stiffnesses in the X_g and Y_g directions.

h_1 (mm)	h_2 (mm)	Stiffness in X_g Direction (x 10^4 N/m)	Stiffness in Y_g Direction (x 10^3 N/m)
1	1	4.98	1.08
1	3	2.17	7.55
1.5	3	1.99	5.95
2	2	2.58	6.40
2	3	1.85	5.00
2.5	3	1.76	4.56
3	3	1.59	4.23
4	4	1.42	3.50
3	1.5	2.62	5.30
3	1	4.51	8.75
1	4	1.82	6.34
2	4	1.45	4.17
3	4	1.31	3.44
2	1	4.73	9.60
1.5	2	2.65	7.36

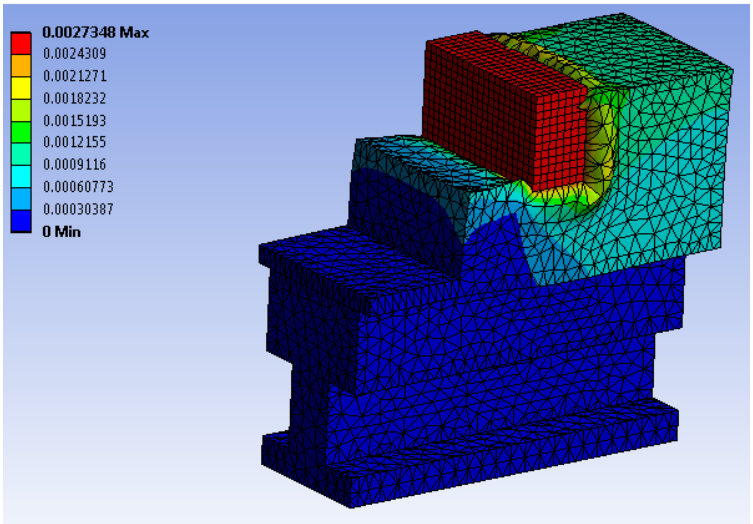

Figure 57: Resultant elastic deformation of the flexible gripper for $(h_1, h_2) = (2,2)$.

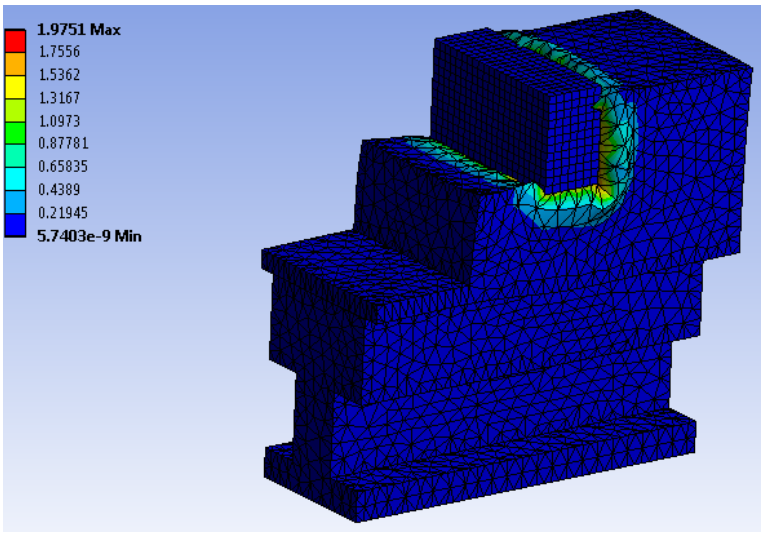

Figure 58: Elastic strain distribution in the flexible gripper for *(h_1, h_2) = (2,2)*.

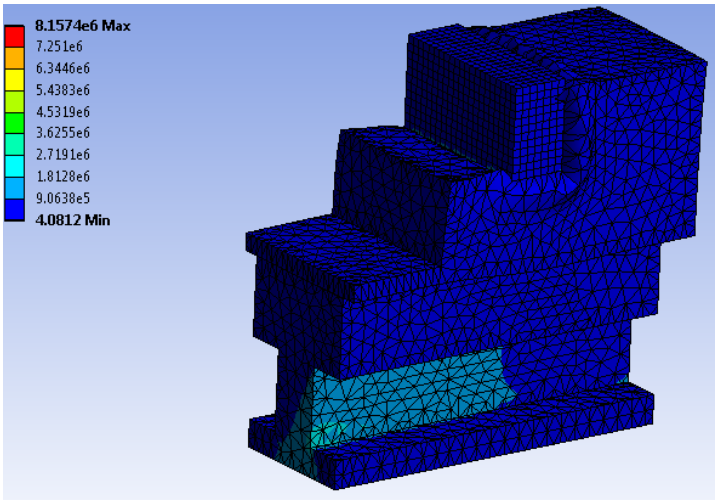

Figure 59: von Mises stress distribution in the flexible gripper for *(h_1, h_2) = (2,2)*.

The simulated stiffness values of the flexible gripper in the X_g and Y_g directions are plotted in Figure 60 and Figure 61 as a function of the gripper design dimensions. The optimal design dimensions are obtained by identifying the regions where the stiffness in the Y_g-direction is large and the stiffness in the X_g-direction is small.

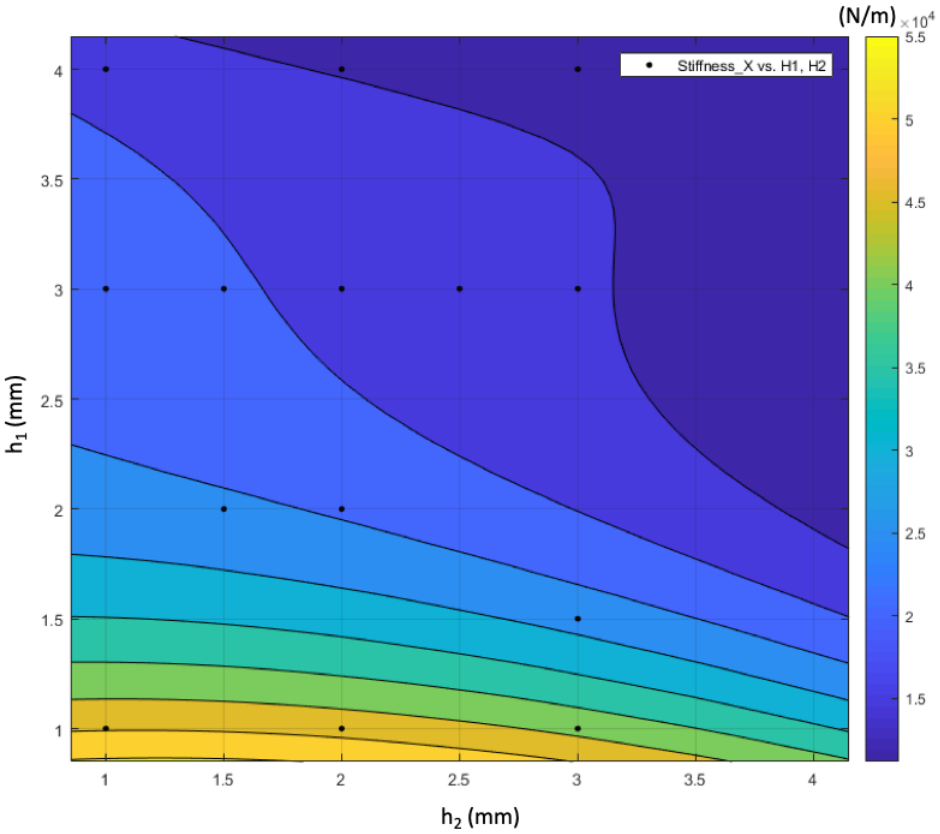

Figure 60: X_g direction stiffness variation with design dimensions h_1 and h_2.

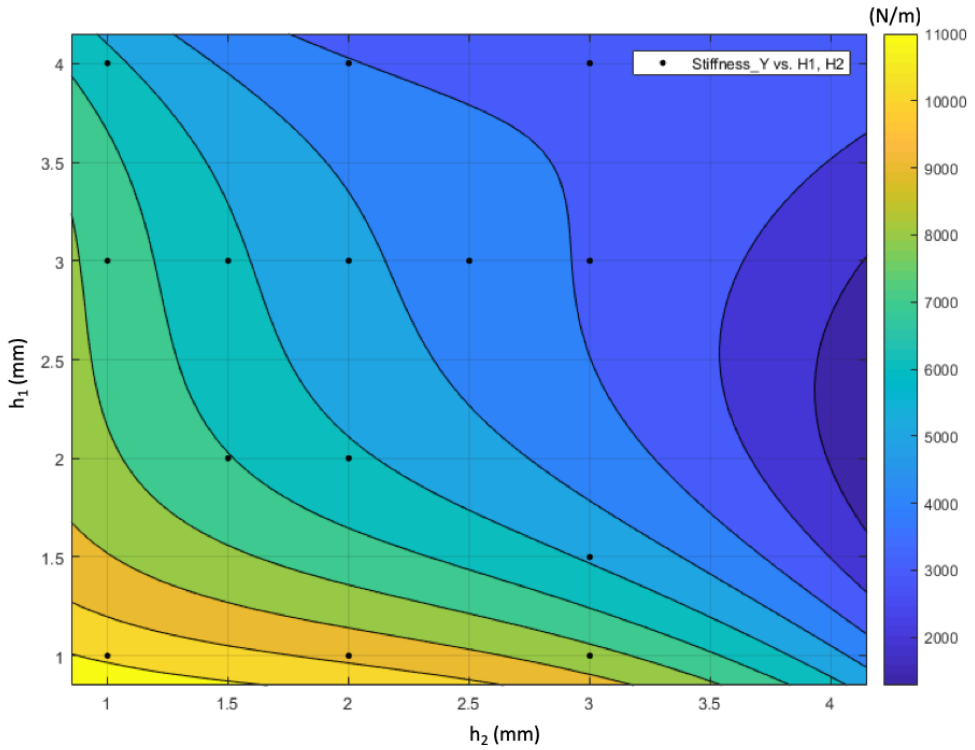

Figure 61: Y_g direction stiffness variation with design dimensions h_1 and h_2.

It is observed from the figures that a larger h_1 yields lower stiffness values in both the X_g and Y_g directions. The same trend is observed for h_2. It should be noted that a large value of h_2 is not desirable because the available height for clamping the part against the jaw face is limited by the jaw face dimensions, which are 5 mm x 10 mm in the current study. Hence, if h_2 is large, the available area of contact between the ring inner race and the gripper insert decreases, which limits the clamping force. This why h_1 and h_2 are limited to a maximum of 4 mm in the simulations. Thus, looking at the two stiffness plots, it is clear that in order to satisfy both design goals (minimizing the X_g-stiffness and maximizing the Y_g-stiffness), the optimal dimensions range from 2 mm to 3 mm for both h_1 and h_2.

Based on the simulation results presented in Figure 60 and Figure 61, and the physical constraint of the jaw face dimension, the values for the flexible gripper dimensions listed in Table 9 are selected for physical prototyping and experimentation.

Table 9: Design dimensions selected for physical prototyping.

h_1 (mm)	h_2 (mm)
2	2
2	3
2.5	3
3	3

5.6 Flexible Gripper Prototyping

This section describes the physical prototyping of the optimal flexible gripper designs identified in Table 9. To achieve the desired flexibility in the gripper inserts, silicone (Shore hardness 20), which is an elastomer, is used as the prototyping material for the gripper inserts. Although it is possible to use low grade rubbers, it is difficult to shape them as desired. Silicone parts are easy to manufacture because liquid phase silicone can be molded into any shape. Also, the molds for shaping silicone can be 3D printed, making it less expensive than CNC machined metal molds. Therefore, the flexible grippers were fabricated by molding silicone (Smooth-On Ecoflex 00-30 Super Soft Platinum Silicone)

in 3D printed molds depicted in Figure 62-Figure 64. The material properties of the silicone material used are listed in Table 10.

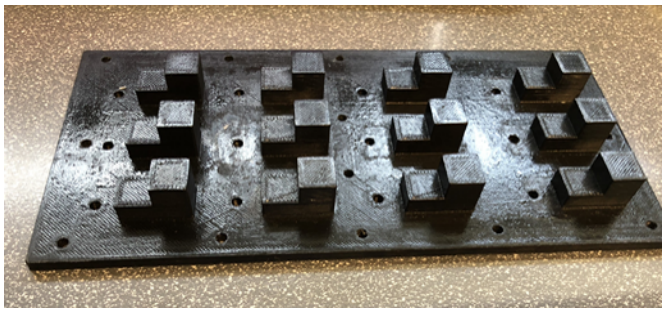

Figure 62: 3D printed male mold.

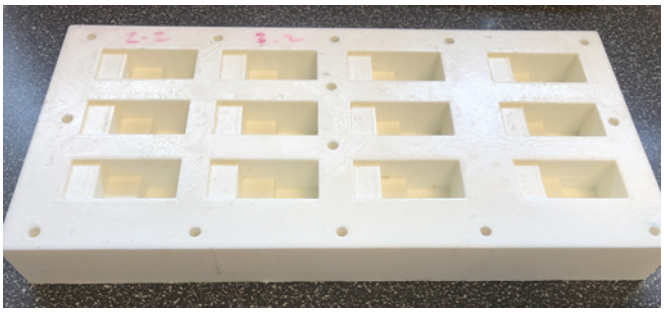

Figure 63: 3D printed female mold.

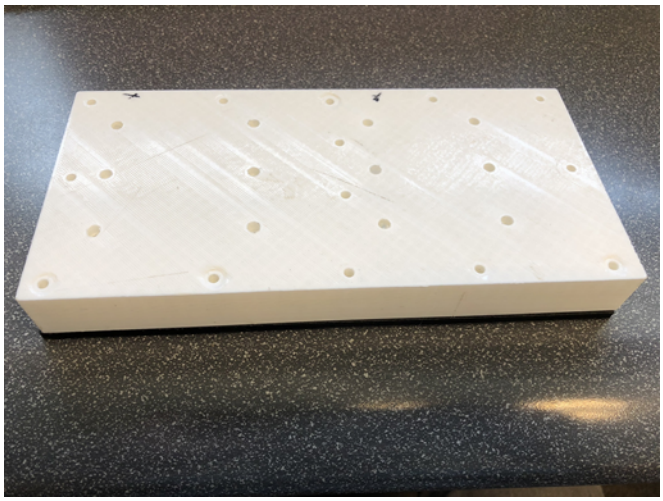

Figure 64: Assembled 3D printed mold.

Table 10: Ecoflex silicone material properties [1].

Properties	Values
Shore hardness	20
Tensile strength	3.79 MPa
Young's modulus	0.337 MPa
Elongation at break	620%
Die B tear strength	21 KN/m

The liquid silicone is poured into the assembled 3D printed mold shown in Figure 64 and allowed to cure for 4 hours before extracting the solidified parts. A representative molded silicone flexible gripper is shown in Figure 51.

5.7 Experimental Results

The experimental setup and face grinding procedure used to evaluate the performance of the flexible gripper inserts are identical to those used in Chapter 4. The only difference is that in the current tests the part is first manually placed between the flexible gripper inserts mounted on the chuck jaws, clamped and then slowly fed into the wheel surface till the ring face firmly and uniformly contacts the grinding wheel surface. This step ensures that the part is gripped properly by silicone inserts on the chuck jaws.

For each combination of flexible gripper design parameters listed in Table 2, the experimental conditions listed in Table 11 were used. The part rotation speed is fixed at 360 rpm. Trim Sol cutting fluid was used as the coolant.

Table 11: Experimental conditions for grinding with flexible gripper inserts.

Test No.	Wheel Speed (rpm)	Infeed Rate (µm/s)	Wheel Hardness Grade
1	1000	20	I
2	1800	20	I
3	2600	20	I

Representative results for the normal force and displacement profiles obtained with a particular flexible gripper design are shown in Figure 65 and Figure 66.

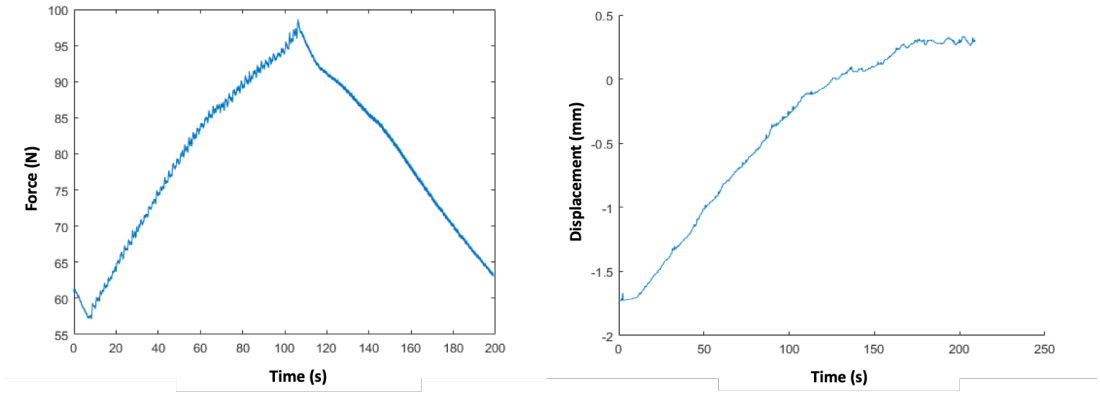

Figure 65: Normal force (left) and displacement (right) profiles for infeed rate = 20 µm/s, wheel speed = 1800 rpm, wheel grade = I; flexible gripper insert dimensions *(h_1, h_2) = (2,2)*.

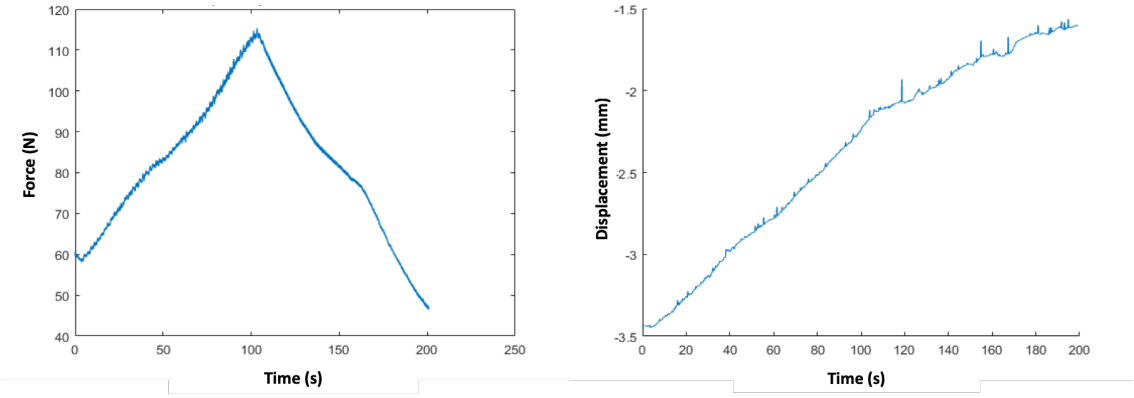

Figure 66: Normal force (left) and displacement (right) plots for feed rate = 20 µm/s, wheel speed = 2600 rpm, wheel grade = I; flexible gripper insert dimensions *(h_1, h_2) = (2,2)*.

As can be seen in the above figures, at $t = 0$ the force starts from a non-zero value, which corresponds to the initial pre-compression of the gripper caused by feeding the part into the grinding wheel till uniform part-wheel surface contact is established. The infeed

rate of the robot is 20 μm/s and because the total thickness of material to be removed is 2 mm, the infeed is stopped after t = 100 s. In the infeed phase (t < 100 s), the measured displacement profile shows nearly linear variation with time, which not only means the actual infeed rate is lower than the commanded infeed rate but also that it is constant over t < 100 s. For t > 100 s, the displacement profile is nearly linear but with a smaller slope than for the initial infeed phase (t < 100 s). This is verified by the fact that the force profile also displays a linearly decreasing trend.

To quantify the force variation amplitude in the grinding force data, the following procedure was used. First, a running window average of the raw force data was computed as described in Chapter 4. The absolute deviation of the force signal from the running window average is calculated at each instant. The average of all such values obtained over the entire time scale is recorded as the 'average amplitude of force variation', which causes vibration of the robot.

Table 12: Force variation amplitude comparison: without and with flexible gripper (design dimension *(h1,h2) = (2 mm,2 mm)*).

Infeed Rate (μm/s)	**Wheel Speed (rpm)**	**Average Amplitude of Force Variation (N)**	
		Without gripper	**With gripper**
20	1000	50	20
20	1800	30	20
20	2600	60	30

Table 12 suggests that the magnitude of force variation during face grinding is significantly reduced by utilizing the flexible gripper inserts. The force variation acts as a forcing function on the robot, whose vibration results in poor surface quality of the part. Thus, reducing the force variation can improve the part quality. Larger reduction in the force variation was obtained by using flexible gripper inserts with optimized dimensions of *(h1,h2) = (3,3)*.

Table 13 lists the surface flatness, parallelism, and surface roughness values of the rings obtained by face grinding with the flexible gripper inserts.

Table 13: Part quality obtained with flexible gripper inserts.

Wheel Speed (rpm)	**Infeed Rate (µm/s)**	**h_1 (mm)**	**h_2 (mm)**	**Flatness (µm)**	**Parallelism (µm)**	**Surface Roughness, S_a (µm)**
1000	20	2	2	3.8	12.1	0.245
1000	20	2	3	3.1	15.8	0.321
1000	20	2.5	3	4.2	14.7	0.347
1000	20	3	3	4.6	12.5	0.378

It can be seen from the table that significant improvement in all three part quality metrics was achieved when face grinding with flexible gripper inserts compared to

without them. The flatness, parallelism and surface roughness in all the cases is well within the typical flatness tolerance (5 μm) for such parts. Again, no discernible trend was observed as a function of the process parameters (infeed rate and wheel speed) and the design dimensions. The use of flexible gripper inserts improved the surface finish due to reduction in the misalignment between the part and wheel and thus decreasing the effect of vibration on the part quality.

5.8 Summary

This chapter analyzed the robot's vibration characteristics (assessed by means of the accelerometer and force/torque sensor measurements) and the resulting part quality. In light of the results and knowledge of the natural resonance modes of the robot determined in Chapter 3, it is evident that the dominant frequencies in the measured force and accelerometer signals are primarily due to rotation of the chuck and the grinding wheel. No robot natural frequencies were found to be excited by the face grinding process for the conditions investigated. The resulting part quality, particularly the surface flatness, parallelism, and surface roughness of the face ground parts were measured and reported. The part-wheel misalignment is the main reason behind the poor surface finish obtained compared to the desired values targeted by bearing manufacturers. The chapter also presented a novel flexible gripper insert design to mitigate the influence of part-wheel angular misalignment (which results in robot vibration) on the face ground part flatness, parallelism, and surface roughness. Robotic face grinding with the flexible gripper inserts yielded significant improvements in the ring part quality metrics. Specifically, an average

part surface flatness improvement of 63%, an improvement in parallelism of 65%, and an improvement of 60% in the surface finish were obtained with the flexible gripper inserts compared to the part quality obtained without the inserts. The main advantage of the flexible gripper inserts is that they ensure that the part and wheel are always aligned irrespective of robot positioning and part fixturing related errors at the start of the grinding cycle, which reduces the force variation at the interface leading to better part quality.

CHAPTER 6. ROBOT POSE OPTIMIZATION

Chapter 3 discussed the grinding cycle time and system time constant by relating the grinding force with the material removal rate via the robot stiffness in the direction normal to the grinding wheel. The robot stiffness was found to be inversely proportional to the system time constant. One of the stated objectives of this thesis is to determine the robot and process parameters that can minimize the system time constant, and consequently the grinding cycle time. Since the robot joints can be modeled as torsional linear springs, the effective Cartesian stiffness at the end-effector depends on the configuration (pose) of all six joints, assuming infinitely stiff links. Hence, it is possible to change the robot pose and thereby achieve the desired Cartesian stiffness at the end-effector.

This chapter first discusses the dependence of the system time constant and grinding cycle time on the robot's Cartesian stiffness. Then, the dependence of robot pose on the Cartesian stiffness is analyzed based on the robot joint kinematics. This is followed by selection of the best robot configuration with respect to the Cartesian stiffness and with regard to practical viability of the chosen robot configuration.

6.1 System Time Constant and Cycle Time

As described in Chapter 4, the time constant of the robot system is given by,

$$\tau = \frac{A}{\lambda_w K_R} \tag{20}$$

As can be seen from the equation, the system time constant is inversely proportional to the robot Cartesian stiffness normal to the grinding wheel. The optimization condition necessary to realize the minimum system constant is to select a robot pose that maximizes its Cartesian stiffness at the end-effector.

6.2 Robot Cartesian Stiffness

The Cartesian stiffness at the robot end-effector is primarily a function of the flexibility in the joints, which causes the robot to act effectively as a torsional spring at the end-effector. The joint stiffnesses are represented as torsional springs. A typical pose of the robot is shown schematically in Figure 67. The base of the robot is at (0, 0, 0). The links are represented by blue bars and the joints are numbered and modeled as red cylinders.

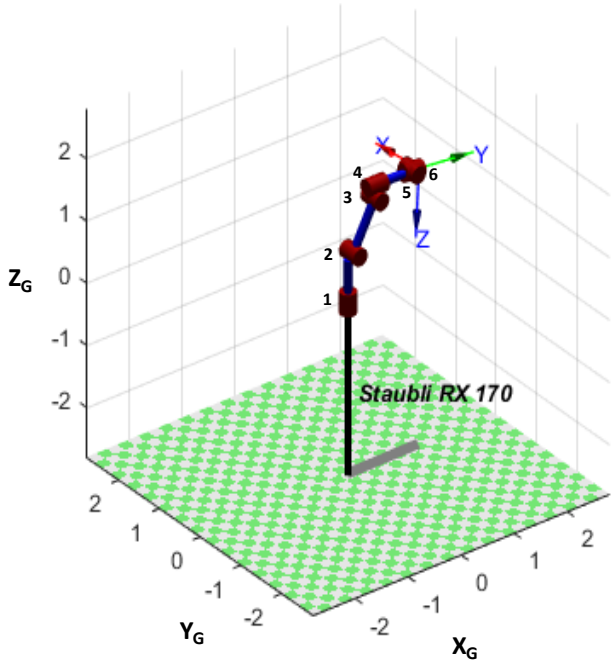

Figure 67: Robot configuration with end-effector reference frame.

The frame of reference attached to the robot's end-effector is of interest here because the feed direction and the normal vector to the face grinding wheel surface are oriented along the Z-axis of the robot frame. This is important to know since the optimization domain consists of robot poses for which the Z-axis of robot's frame is not always aligned with the global coordinate system Z_G.

Per the model derived by Salisbury [89], the robot Cartesian stiffness at the end-effector is given by,

$$K = (J^{-1})^T K_\theta J^{-1} \tag{21}$$

This involves computing the inverse of the Jacobian matrix, which can introduce errors, especially when it is close to a singularity [91].

To avoid singularities, the compliance matrix is used to relate the force and displacement at the end-effector as,

$$\Delta X = C\ F \tag{22}$$

where,

$$C = J^T\ K_\theta^{-1}\ J \tag{23}$$

and where ΔX is the vector of displacements measured the end-effector, F is the force vector acting on the end-effector, C is the compliance matrix, and J is the Jacobian matrix of the robot estimated from the kinematic model as described by Whitney [106]. K_θ is the diagonal joint stiffness matrix that is given by,

$$K_\theta = \begin{bmatrix} K_1 & 0 & 0 & 0 & 0 & 0 \\ 0 & K_2 & 0 & 0 & 0 & 0 \\ 0 & 0 & K_3 & 0 & 0 & 0 \\ 0 & 0 & 0 & K_4 & 0 & 0 \\ 0 & 0 & 0 & 0 & K_5 & 0 \\ 0 & 0 & 0 & 0 & 0 & K_6 \end{bmatrix}$$

where K_i are the joint stiffness values adopted from the work of Olabi [107], who determined the stiffness of each joint of a 6-dof Staubli RX 170 industrial robot by measuring the angular displacement of the joint due to an external torque applied to the joint. The joint stiffness values used in this study are listed in Table 14.

Table 14: Staubli RX 170 robot joint stiffness values [107].

Joint Number	1	2	3	4	5	6
K_θ (x 10^6 N.m/rad)	0.204	0.85	0.57	0.49	0.12	0.005

The Jacobian matrix is normally determined from the Denavit-Hartenberg (DH) parameters, which were defined by Hartenberg [108]. The Modified DH (DHm) parameters [109], shown in Figure 68, for the Staubli RX 170 robot, measured from the base to the end-effector, are listed in Table 15.

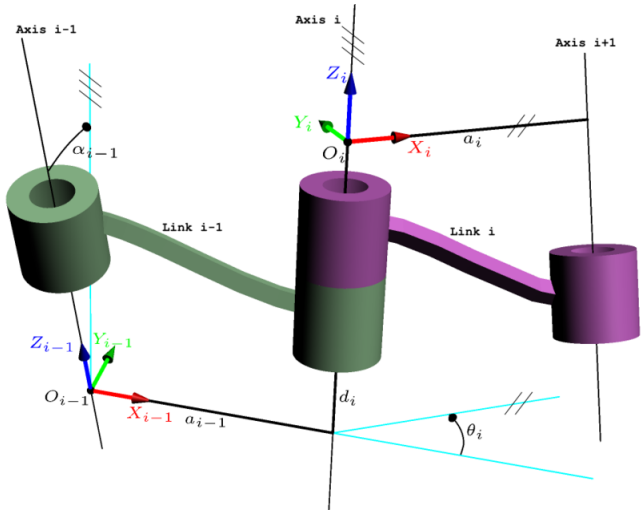

Figure 68: DHm parameters [109].

Table 15: DHm parameters for the Staubli RX 170.

Joints	α_i	d_i (m)	a_i (m)
1	-π/2	0.75	0.1
2	0	0	0.850
3	π/2	0	-0.2
4	- π /2	0.7	0
5	π/2	0	0
6	π/2	0.135	0

6.3 Stiffness Optimization

This section presents the results of simulations aimed at optimizing the robot's Cartesian stiffness in the Z-direction (robot end-effector frame). Robot poses are varied in the Cartesian space and the corresponding stiffness in the Z-direction (robot end-effector frame) is computed for each pose. Due to the inability of arbitrarily orienting the grinding wheel spindle axis relative to the robot end-effector, the workpiece infeed direction is constrained to be either in the global $-Z_G$ (vertical feed) or $+X_G$ (horizontal feed) directions, as illustrated in Figure 69 and Figure 70, respectively.

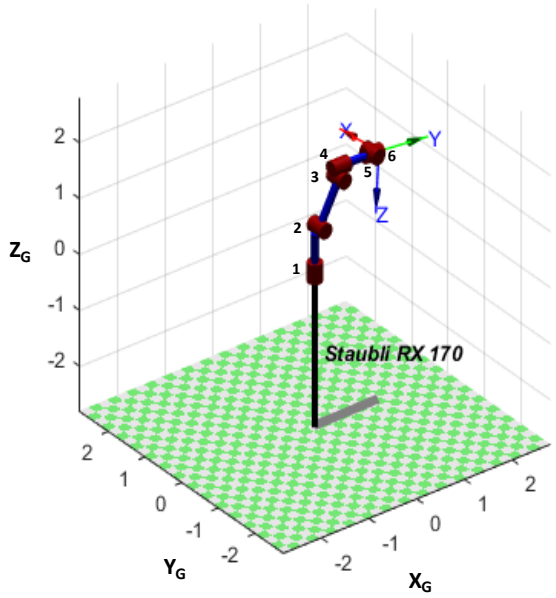

Figure 69: Vertical infeed configuration.

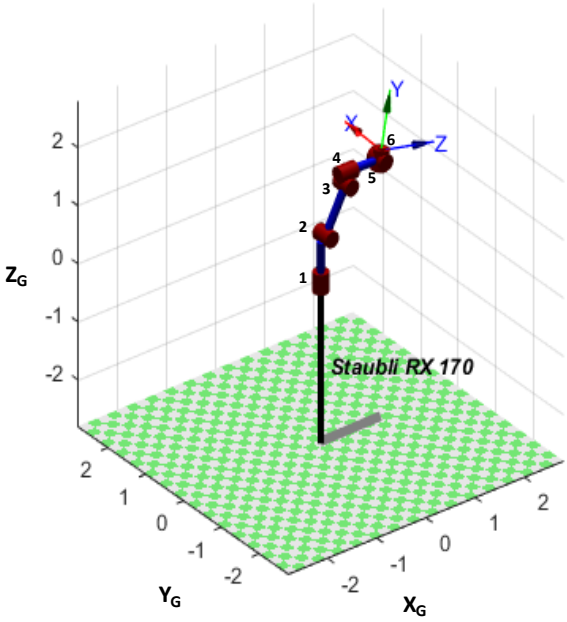

Figure 70: Horizontal infeed configuration.

Variations in Joint 1 and 6 of the robot are not considered in this analysis because they are redundant since the end-effector feed is constrained to be along $+X_G$ or $-Z_G$. Joint 4 has a rotational axis along the length of link 4 and hence varying this joint angle changes the orientation of the end-effector out of the global X_G-Z_G plane. Such poses are not considered in this study in order to ensure that the workpiece infeed direction is constrained to be in either the $+X_G$ or $-Z_G$ directions. Joint angles 2, 3 and 5 are varied over their entire range ($(-\pi,0)$ for joint 2, $(0,3\pi/2$ for joint 3, $(\pi,-\pi/2)$ for joint 5) to generate different robot poses and the corresponding end-of-arm Cartesian stiffness values are computed accordingly. The calculated results are shown in Figure 71 and Figure 72 for the two workpiece feed orientations considered in the analysis. Note that the robot base is located at (0, 0) and the Cartesian stiffness values along the global $+Z_G$ direction are plotted as a function of the end-effector Cartesian position.

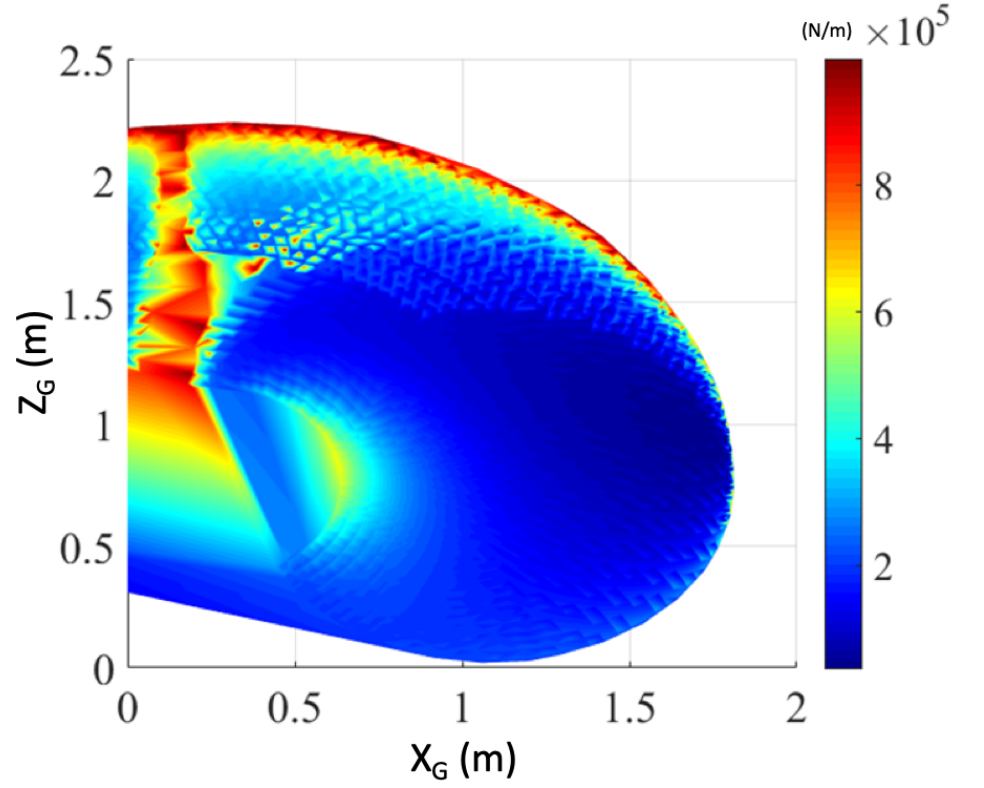

Figure 71: Variation of Cartesian stiffness in the $+Z_G$ direction for vertical infeed configurations of the robot.

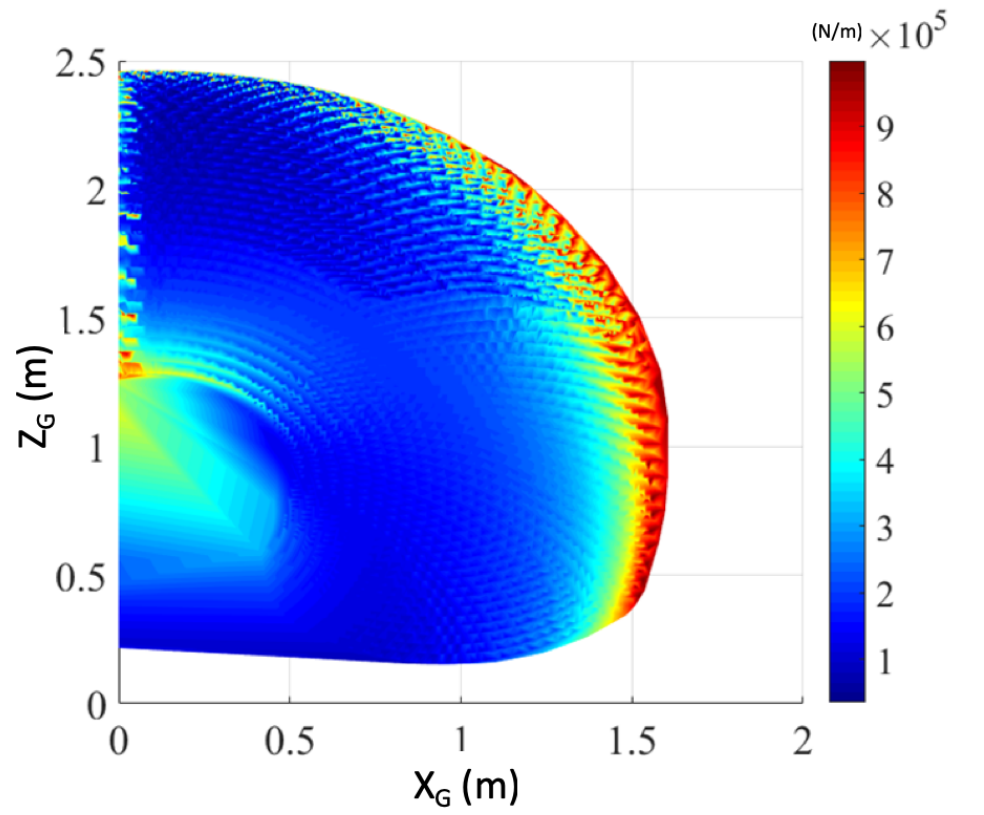

Figure 72: Variation of Cartesian stiffness in the -X_G direction for horizontal infeed configurations of the robot.

It is evident from the two plots that the best robot poses lie along contours that have the highest Cartesian stiffness. Choosing robot poses with maximum stiffness along the robot end-effector's Z-axis (robot end-effector frame) will guarantee the lowest system time constant and hence a lower total grinding cycle time, as seen from Equation 20. The following specific conclusions can be drawn from the above figures for the two workpiece infeed configurations.

For the vertical infeed configurations:

1. Higher stiffness configurations of the robot are achievable with the end-effector position located furthest away from the $X_G = 0$ plane for Z_G values greater than 1.5 meters.
2. End-effector positions with stiffer robot configurations also appear near $X_G = 0$. This is true for configurations with end-effector's position Z_G (in robot base frame) less than 1.5 m. The reason for this is that further the end-effector is away from the $X_G = 0$ plane, the longer the arm length, which lowers the Cartesian stiffness of the corresponding pose.
3. From the view of practical application, operating with robot configurations where the robot end-effector is close to the $X_G = 0$ plane is difficult since the grinding wheel, the wheel spindle, and/or the coolant collection tank can interfere with the robot joints.

For the horizontal infeed configurations:

1. High stiffness configurations of the robot are achievable at end-effector positions located furthest away from the robot base in the $+X_G$ direction for $Z_G < 1.5$ m. These configurations have links 2 and 3 oriented horizontally such that the end-effector is stretched out and away from the origin of robot's base frame (global). The reason for this is that the more stretched out the robot is, the more difficult it is to displace it with a horizontal force.
2. Hence, for horizontal infeed configurations, it is best to operate with the robot stretched out the most and with $Z_G < 1.5$ m.

It must be noted that the critical values of the end-effector's Z_G position (global frame) mentioned in the results and discussion are specific to the robot used in this research work (Staubli RX 170) since they are a function of the robot's link lengths. However, the the methodology used here can be used for any other robot specification.

6.4 Summary

This chapter discussed pose optimization of the robot to achieve the maximum Cartesian stiffness at the end-effector in the robot's global Z-axis. The Cartesian stiffness of the robot along the Z-direction (robot end-effector frame) was evaluated for end-effector positions in the robot's entire workspace for two workpiece infeed configurations: 1) Along $-Z_G$ (global frame) and 2) Along $+X_G$ (global frame).

It was found that for workpiece infeed along vertical direction ($-Z_G$ in global frame), the stiffest robot poses are realized along the periphery of the robot's workspace, and near the $X_G = 0$ plane and $Z_G > 1.5$ m. Since the normal grinding force for the vertical infeed configuration acts along $+Z_G$, the Cartesian stiffness is higher when the end-effector is close to the $X_G = 0$ plane. However, it is difficult to operate near the $X_G = 0$ plane because the grinding wheel and coolant tank can interfere with the robot's joints.

Similarly, for workpiece infeed along the horizontal direction (X_G in global frame), the stiffest robot configurations are found to be along the periphery of the robot's workspace for $Z_G < 1.5$ m. Since the normal grinding force for this configuration acts in the $-X_G$ direction, the stiffness is higher as the robot arm is stretched out and away from the $X_G = 0$ plane. The only difficulty with utilizing such configurations is that the grinding

wheel and spindle axes have to be oriented along $-X_G$, which is challenging because the entire spindle and wheel assembly has to be mounted horizontally.

CHAPTER 7. CONCLUSIONS AND RECOMMENDATIONS

This chapter summarizes the main scientific contributions, the main conclusions of this thesis, and suggests possible areas for future studies.

7.1 Main Contributions

1. This is the first reported scientific study of a robotic face grinding process.
2. The thesis presents a quantitative model-based understanding of the influence of robot compliance on the face grinding cycle time and part quality.
3. A novel flexible gripper is proposed to mitigate the effects of part-wheel misalignment and resulting vibration on the part quality in robotic face grinding.
4. An understanding of influence of robot pose on its Cartesian stiffness at the end-effector is presented with the goal of minimizing the system time constant and the overall grinding cycle time.
5. Knowledge acquired in this thesis can be utilized by industry practitioners to design a practical robotic face grinding system and determine the necessary operating parameters like the wheel speed, infeed rate, and robot pose required to achieve the desired production rate, which is governed by the overall cycle time, and the desired part quality.

7.2 Main Conclusions

The main conclusions drawn from each major task in this research are summarized below.

Robotic Face Grinding Cycle Behavior

- The system time constant and the grinding process cycle time were observed to be directly proportional to the robot infeed rate and inversely proportional to the robot Cartesian stiffness and grinding wheel speed.
- The material removal parameter (λ_w) was found to be directly proportional to the grinding wheel speed.
- Minimizing the grinding process cycle time requires the robotic face grinding process to be operated at the highest achievable wheel speed, using a robot with the highest possible Cartesian stiffness at the end-effector, and at the highest possible infeed rate, which is constrained by vibration.

Modal Characterization of Robotic Face Grinding System

- Modal impact hammer tests on the robotic face grinding setup showed that the compliance of the system per unit force is highest in the directions normal to and tangential to the grinding wheel surface.
- The robotic face grinding setup developed and evaluated in this thesis has the highest compliance in the Y_G direction when excited at its natural frequency in that direction relative to excitation in the other directions.
- The vibration responses of the robotic face grinding system evaluated in this thesis are cross-coupled in the X_G and Z_G directions. This implies that the system can be excited in both directions provided the grinding force contains

frequencies close to or equal to the natural frequency of the system in the two excitation directions.

- The frequency contents of the force and acceleration signals showed that the peaks in the corresponding FFT responses occur at the harmonics of the wheel and workpiece rotation frequencies in all cases, except at a wheel speed of 1800 rpm where the system's natural frequency was also present. This confirms that the robotic face grinding system's natural vibration frequencies are not excited under most of the process conditions evaluated.

Part Quality in Robotic Face Grinding

- The primary causes for the poor part quality in robotic face grinding is the angular misalignment between the part and the wheel surface which also results in robot vibrations.
- A flexible gripper jaw insert was design optimized, prototyped, and tested to minimize the effects of the forced vibrations and part-wheel misalignment errors. A significant improvement in part quality was obtained when face grinding with the flexible gripper inserts. Specifically, an average part surface flatness improvement of 63%, an improvement in parallelism of 65%, and an improvement of 60% in the surface finish were obtained with the flexible gripper inserts compared to the part quality obtained without the inserts.

Robot Configuration (Pose) Optimization

- Since the grinding cycle time is inversely proportional to the robot's Cartesian stiffness in the infeed direction, the optimum robot pose is one that has the Cartesian stiffness at the end-effector.
- For configurations in which the workpiece infeed is constrained in the global + X_G-direction, the stiffest poses are ones where the end of arm tooling is located along the periphery of the robot's workspace with $Z_G < 1.5$ m.
- For configurations in which the workpiece infeed is constrained in the global – Z_G-direction, the stiffest poses are those that are located along the periphery of the robot's workspace and close to the $X_G = 0$ plane and for $Z_G > 1.5$ m.

7.3 Recommendations for Future Work

This thesis implemented the robotic face grinding process on a Staubli RX 170 industrial robot, which has a limited payload of 35 Kg. In addition, the chuck motor used to rotate the workpiece has an axial load limit of 70 N. Both of these limitations restrict the commanded infeed rate and therefore the material removal rate. This in turn has a negative impact on the grinding cycle time. However, the background theory and results presented in this thesis can be utilized by practitioners to design a robotic face grinding system that overcomes these limitations to meet their specific material removal rate and grinding cycle time needs. Design of the system includes selecting a higher payload robot, configuring the robot posture to yield higher Cartesian stiffness at the end-effector, and utilizing a higher torque/force rated chuck motor. Based on the understanding of the robotic face

grinding system vibration characteristics presented in the thesis, further design optimization can be carried out to adapt the novel flexible gripper insert idea to a specific robot system and grinding process conditions. The entire study presented in this work can be further extended to standard industrial applications that usually involve simultaneous face grinding of multiple parts, like in a Diskus face grinding machine [30].

An interesting potential application of robotic face grinding includes finishing of complex shaped (e.g. sculptured) parts. A key advantage of using a six-axis robot is that complex part geometries can be finished by continuously reconfiguring the robot to present different surfaces of the complex workpiece geometry to the grinding wheel. The process model for the robotic face grinding cycle time presented in this thesis can be modified for complex part geometries by utilizing the Cartesian stiffness model presented in Chapter 6 to estimate the robot stiffness for different robot poses required to grind various surfaces of a geometrically complex part. Examples of industrial applications where such a study would be useful are polishing and grinding of large aspherical mirrors and knee implants [110, 111, 112].

Another interesting idea that could be investigated in future work is to isolate the robot entirely from the grinding process forces. To accomplish this, the system design would require an actuation system (e.g. hydraulic actuator) at the robot end-effector capable of holding the workpiece via a flexible diaphragm that is actuated by the hydraulic fluid. The instantaneous elastic deformations of the flexible diaphragm due to the grinding forces can be dynamically counteracted by varying the pressure exerted on the diaphragm by the hydraulic fluid via a high frequency valve and pump, thus isolating the robot from the grinding forces. In such a system, the power to grind the part would be provided by the

hydraulic pump and the robot would be used to simply position the part at the precise position and orientation over the grinding wheel. A challenge in implementing this idea is that the workpiece holding diaphragm enclosing the hydraulic fluid also needs to be rotating continuously.

APPENDIX

Table 16: Material Removal Parameter (λ_w) for various experimental conditions.

Test No.	Wheel Speed (RPM)	Feed (µm/s)	Wheel Grade	Material Removal Parameter, λ_w x 10^{-10} (m^3/N s)
1	1000	10	G	2.22
2	1400	10	G	2.5
3	1800	10	G	3.125
4	2200	10	G	4.34
5	2600	10	G	5
6	1000	20	G	1.85
7	1400	20	G	2.5
8	1800	20	G	3.33
9	2200	20	G	4.76
10	2600	20	G	5.26
11	1000	30	G	2.22
12	1400	30	G	2.43
13	1800	30	G	3.70

Table 16: Material Removal Parameter (λ_w) for various experimental conditions (Continued).

14	2200	30	G	4.34
15	2600	30	G	4.76
16	1000	10	I	1.66
17	1400	10	I	1.96
18	1800	10	I	2.38
19	2200	10	I	2.90
20	2600	10	I	2.44
21	1000	20	I	2.22
22	1400	20	I	2.43
23	1800	20	I	2.77
24	2200	20	I	3.22
25	2600	20	I	4
26	1000	30	I	2.12
27	1400	30	I	2.77
28	1800	30	I	3.33
29	2200	30	I	3.70
30	2600	30	I	4.54

REFERENCES

[1] "Dragon Skin-20, Silicone material properties," [Online]. Available: https://www.smooth-on.com/products/dragon-skin-20/. [Accessed 6 May 2019].

[2] [Online]. Available: https://www.kmtgrinding.com/machine/dg-500/.

[3] J. K. J. F. J. E. G. Agapakis, "Vision-Aided Robotic Welding: An Approach and a Flexible Implementation," *The International Journal of Robotics Research,* vol. 9, no. 5, pp. 17-34, October 1990.

[4] M. a. K. H. Her, "Automated Robotic Deburring of Parts Using Compliance Control," *Journal of Dynamic Systems, Measurement, and Control,* vol. 113, no. 1, pp. 60-66, 1991.

[5] [Online]. Available: https://www.motoman.com/robotic-painting.

[6] [Online]. Available: https://www.kuka.com/en-in/technologies/process-technologies/2016/07/deburring.

[7] M. S. J. A. I. Iglesias, "Overview of the state of robotic machining: Current and future potential," *Procedia Engineering,* vol. 132, pp. 911-917, 2015.

[8] K. S. N. Y. Y. O. S.-i. Matsuoka, "High-speed end milling of an articulated robot and its characteristics," *Journal of materials processing technology,* vol. 95, pp. 83-89, 1999.

[9] "A Rapid coordinate transformation method applied in industrial robot calibration based on characteristic line coincidence," *Sensors,* vol. 16, p. 239, 2016.

[10] "Cutting tools research: report of subcommittee on carbide tools: the mechanism of tool vibration in the cutting of steel," *Proceedings of the Institution of,* vol. 154, pp. 261-284, 1946.

[11] S. &. G. C. Malkin, Grinding technology: theory and application of machining with abrasives, Industrial Press Inc., 2008.

[12] G. &. C. J. Quintana, "Chatter in machining processes: A review," *International Journal of Machine Tools and Manufacture,* vol. 51, no. 5, pp. 363 - 376, 2011.

[13] Z. Z. H. Z. Z. &. W. J. Pan, "Chatter analysis of robotic machining process," *Journal of materials processing technology,* vol. 173, no. 3, pp. 301-309, 2006.

[14] Z. &. Z. H. Pan, "Robotic machining from programming to process control: a complete solution by force control," *Industrial Robot: An International Journal,* vol. 35, no. 5, pp. 400-409, 2008.

[15] Z. &. Z. H. Pan, "Analysis and suppression of chatter in robotic machining process," *International Conference on Control, Automation and Systems,* pp. 595 - 600, 2007.

[16] H. Merritt, "Theory of Self-Excited Machine-Tool Chatter: Contribution to Machine- Tool Chatter Research," *Journal of engineering for industry,* vol. 87, pp. 447-454, 1965.

[17] H. D. Y. G. Y. K. G. Wang, "Chatter mechanism and stability analysis of robotic boring," *The International Journal of Advanced Manufacturing Technology,* pp. 1 - 11, 2016.

[18] T. T. Company, "Timken Bearing Design Guide," The Timken Company, [Online]. Available: https://www.timken.com/resources/timken-engineering-manual/. [Accessed 5 July 2019].

[19] D. S. L.T. Tunc, "Tool path pattern and feed direction selection in robotic milling for increased chatter-free material removal rate," *The International Journal of Advanced Manufacturing Technology,* pp. 1-12, 2017.

[20] Z. Z. H. T. Z. X. &. D. H. Chen, "Adaptive active chatter control in milling processes," *Journal of Dynamic Systems, Measurement, and Control,* vol. 136, no. 2, p. 021007, 2014.

[21] J. L. L. J. P. H. T. D. S. N. R. M. K. C. M. .. &. B. K. Dohner, "Mitigation of Chatter Instabilities in Milling by Active Structural Control," *Journal of sound and vibration,* vol. 269, no. 1-2, pp. 197-211, 2004.

[22] R. L. K. C. C. &. S. L. S. Fittro, "μ synthesis applied to the compliance minimization of an active magnetic bearing HSM spindle's thrust axis," *Machining science and technology,* vol. 7, no. 1, pp. 19-51, 2003.

[23] Y. &. S. N. D. Zhang, "Milling workpiece chatter avoidance using piezoelectric active damping: a feasibility study," *Smart materials and structures,* vol. 14, no. 6, p. N65, 2005.

[24] A. B. H. I. J. I. T. D. A. &. P. A. Ganguli, "Regenerative chatter reduction by active damping control," *Journal of sound and vibration,* vol. 300, no. 3-5, pp. 847-862, 2007.

[25] H. X. &. G. X. L. Deng, "Adaptive tuned vibration absorber based on magnetorheological elastomer," *Journal of intelligent material systems and structures,* vol. 18, pp. 1205-1210, 207.

[26] H. X. G. X. L. &. W. L. H. Deng, "Development of an adaptive tuned vibration absorber with magnetorheological elastomer," *Smart materials and structures,* vol. 15, no. 5, p. N111, 2006.

[27] "Passive, adaptive and active tuned vibration absorbers—a survey," *Journal of Vibration and Acoustics,* vol. 117, pp. 234-242, 1995.

[28] K. &. K. S. Serope, Manufacturing engineering and technology., 1992.

[29] I. D. H. M. P. U. E. R. W. B. &. I. I. Marinescu, Handbook of machining with grinding wheels, Boca Raton, FL, USA: CRC Press, 2016.

[30] "Diskus face grinding machine," [Online]. Available: http://diskus-werke.dvs-gruppe.com/uploads/tx_xpctypedownloadssimple/DISKUS-WERKE-Schleiftechnik-Uebersicht-Planseiten-Schleifmaschinen-EN.pdf. [Accessed 18 May 2019].

[31] G. S. Reichenbach, "The role of chip thickness in grinding," *Trans. Asme,* vol. 78, no. 5, p. 23, 1956.

[32] M. J. Hillier, "On a three-dimensional model of the surface grinding process," *International Journal of Machine Tool Design and Research,* vol. 6, no. 3, pp. 109-113, 1966.

[33] R. P. J. &. D. A. Snoeys, "The significance of chip thickness in grinding," *Annals of the CIRP,* vol. 23, no. 2, pp. 227-237, 1974.

[34] R. S. &. L. R. P. Hahn, "PRINCIPLES OF GRINDING. 1. BASIC RELATIONSHIPS IN PRECISION GRINDING," *Machinery,* vol. 77, no. 7, p. 55, 1971.

[35] R. S. &. L. R. P. Hahn, "PRINCIPLES OF GRINDING. 2. METAL REMOVAL PARAMETER," *Machinery,* vol. 77, no. 8, p. 33, 1971.

[36] R. P. Lindsay, "The effect of parameter variations in precision grinding," *Journal of Engineering for Industry,* pp. 92(3), 683-693, 1970.

[37] R. S. &. L. R. P. Hahn, "The influence of process variables on material removal, surface integrity, surface finish and vibration in grinding," *Advances in Machine Tool Design and Research,* pp. 95-117, 1969.

[38] S. &. K. S. Malkin, "Effects of grain size and operating parameters on the mechanics of grinding," *J. Eng. Ind. Trans ASME Ser. B,* vol. 94, pp. 833-842, 1972.

[39] R. L. L. S. Y. W. X. J. X. P. &. J. D. G. W. Hecker, "Grinding force and power modeling based on chip thickness analysis," *The International Journal of Advanced Manufacturing Technology,* vol. 33, no. 5-6, pp. 449-459, 2007.

[40] P. K. S. B. &. L. G. K. Basuray, "Surface generated in fine grinding. Part 1 Probabilistic model.," *The International Journal of Production Research,* vol. 19, no. 6, pp. 677-688, 1981.

[41] X. &. R. W. B. Chen, "Analysis and simulation of the grinding process. Part II: Mechanics of grinding," *International Journal of Machine Tools and Manufacture,* vol. 36, no. 8, pp. 883-896, 1996.

[42] Z. B. &. K. R. Hou, "On the mechanics of the grinding process–Part I. Stochastic nature of the grinding process," *International journal of machine tools and manufacture,* vol. 43, no. 15, pp. 1579-1593, 2003.

[43] G. K. Lal, "Forces in vertical surface grinding," *International Journal of Machine Tool Design and Research,* vol. 8, no. 1, pp. 33-43, 1968.

[44] G. &. L. G. K. Srihari, " Mechanics of vertical surface grinding," *Journal of materials processing technology,* vol. 44, no. 1-2, pp. 14-28, 1994.

[45] S. &. K. Y. Malkin, "Optimal infeed control for accelerated spark-out in plunge grinding," *Journal of engineering for industry,* vol. 106, no. 1, pp. 70-74, 1984.

[46] I. K. B. A. &. L. H. S. Inasaki, "Grinding chatter–origin and suppression," *CIRP Annals,* vol. 50, pp. 515-534, 2001.

[47] R. &. B. D. Snoeys, "Dominating parameters in grinding wheel—and workpiece regenerative chatter," *Advances in Machine Tool Design and Research,* pp. 325-348, 1970.

[48] J. &. V. P. Peters, "The unbalance of electromotors and their influence on the surface geometry in surface grinding," *CIRP Annals-Manufacturing Technology,* pp. 585-589, 1971.

[49] J. F. G. F. T. V. &. W. J. P. Oliveira, "Experimental analysis of wheel/workpiece dynamic interactions in grinding," *CIRP annals,* vol. 57, no. 1, pp. 329-332, 2008.

[50] R. S. Hahn, "On the theory of regenerative chatter in precision-grinding operations," *Trans. ASME,* pp. 593-597, 1954.

[51] B. &. L. G. G. Bartalucci, "Grinding process instability," *Journal of Engineering for Industry,* vol. 91, no. 3, pp. 597-606, 1969.

[52] Y. M. M. &. S. S. Furukawa, "Vibration analysis and work-rounding mechanism in centerless grinding," *International Journal of Machine Tool Design and Research,* vol. 11, no. 2, pp. 145-175, 1971.

[53] M. H. N. &. S. A. Weck, "Dynamic behaviour of cylindrical traverse grinding processes," *CIRP Annals,* vol. 50, no. 1, pp. 213-216, 2001.

[54] R. A. Thompson, "On the doubly regenerative stability of a grinder: the theory of chatter growth," *Journal of Engineering for Industry,* vol. 108, no. 2, pp. 75-82, 1986.

[55] T. M. S. M. S. H. O. &. K. Hoshi, "Suppression of wheel regenerative grinding vibration by alternating wheel speed," *CIRP Annals,* vol. 35, no. 1, pp. 231-234, 1986.

[56] Colding, "How Stiffness Affecting Grinding Performance," *Machinery (NY),* p. 57, 1970.

[57] Inoue, "Chattering phenomenon in grinding," *Bull. of the Japan Soc. of Prec. Engg,* p. 67, 1969.

[58] T. H. L. J. R. Leist, "Practical Methods to Obtain Imporved Grinding Machine Stability," *Industrial Diamond Review,* vol. 30, no. 353, p. 129, 1970.

[59] G. Cegrell, "Variable Wheel Speed - A way to increase the metal removal rate," *Proceedings of the Fourteenth International Machine Tool Design anf Research Conference,* p. 653, 1973.

[60] Z. M. S. G. H. T. D. &. G. R. E. Bzymek, "Design of flexible grinding wheel with variable hub thickness," *Journal of engineering for industry,* vol. 116, pp. 260-262, 1994.

[61] H. W. J. Z. G. G. Z. P. Z. C. H. Zhang, "Machining with flexible manipulator: toward improving robotic machining performance," *Proceedings, 2005 IEEE/ASME International Conference on Advanced Intelligent Mechatronics,* pp. 1127-1132, 2005.

[62] S. G. V. B. B. C. &. R. P. Mousavi, "Dynamic modeling and stability prediction in robotic machining," *The International Journal of Advanced Manufacturing Technology,* vol. 88, no. 9-12, pp. 3053-3065, 2017.

[63] F. Z. H. L. D. C. L. T. C. &. D. H. Chen, "Robotic grinding of a blisk with two degrees of freedom contact force control," *The International Journal of Advanced Manufacturing Technology,* vol. 101, no. 1-4, pp. 461-474, 2019.

[64] W. L. X. H. Z. G. Y. S. J. &. Y. Z. P. Li, "3-D shape matching of a blade surface in robotic grinding applications," *IEEE/ASME Transactions on Mechatronics,* vol. 21, no. 5, pp. 2294-2306, 2016.

[65] W. L. F. L. Z. &. Y. C. Wang, "Prediction of depth of cut for robotic belt grinding," *The International Journal of Advanced Manufacturing Technology,* vol. 91, no. 1-4, pp. 699-708, 2017.

[66] D. L. S. Y. L. C. W. Y. S. &. D. H. Zhu, "On energetic assessment of cutting mechanisms in robot-assisted belt grinding of titanium alloys," *Tribology International,* vol. 90, pp. 55-59, 2015.

[67] X. C. M. Z. X. &. K. B. Ren, "A local process model for simulation of robotic belt grinding," *International Journal of Machine Tools and Manufacture,* vol. 47, no. 6, pp. 962-970, 2007.

[68] S. H. L. &. Z. Y. Yixu, " An adaptive modeling method for a robot belt grinding process," *IEEE/ASME Transactions on Mechatronics,* vol. 17, no. 2, pp. 309-317, 2011.

[69] X. &. S. L. Xie, "Force control based robotic grinding system and application," *2016 12th World Congress on Intelligent Control and Automation,* pp. 2552-2555, 2016.

[70] Y. G. D. J. &. K. K. Sun, "Accurate robotic belt grinding of workpieces with complex geometries using relative calibration techniques," *Robotics and Computer-Integrated Manufacturing,* vol. 25, no. 1, pp. 204-210, 2009.

[71] H. G. Z. M. C. X. Q. &. Z. L. Huang, "Robotic grinding and polishing for turbine-vane overhaul," *Journal of materials processing technology,* vol. 127, no. 2, pp. 140-145, 2002.

[72] T. L. T. K. &. S. P. K. Thomessen, "Robot control system for grinding of large hydro power turbines," *Industrial Robot: An International Journal,* vol. 28, no. 4, pp. 328-334, 2001.

[73] H. Y. K. M. &. E. M. A. Dai, "Parametric modelling and control of the robotic grinding process," *The International Journal of Advanced Manufacturing Technology,* vol. 8, no. 3, pp. 182-192, 1993.

[74] Y. &. D. F. Chen, "Robot machining: recent development and future research issues," *The International Journal of Advanced Manufacturing Technology,* vol. 66, no. 9-12, pp. 1489-1497, 2013.

[75] J. D. C. S. P. &. C. G. Pandremenos, "Machining with robots: a critical review," *Proceedings of DET2011,* pp. 1-9, 2011.

[76] J. &. P. M. Tlusty, "The stability of machine tools against self-excited vibrations in machining," *Proceedings of the ASME International,* 1963.

[77] G. D. H. G. Y. &. K. Y. Wang, "Chatter mechanism and stability analysis of robotic boring," *The International Journal of Advanced Manufacturing Technology,* vol. 91, no. 1-4, pp. 411-421, 2017.

[78] M. H. R. L. L. J. A. &. F.-S. J. Miguelez, "Improvement of chatter stability in boring operations with passive vibration absorbers," *International Journal of Mechanical Sciences,* vol. 52, no. 10, pp. 1376-1384, 2010.

[79] Y. S. K. J. Y. &. L. E. C. Tarng, "Chatter suppression in turning operations with a tuned vibration absorber," *Journal of materials processing technology,* vol. 105, no. 1-2, pp. 55-60, 2000.

[80] M. M. V. G. S. V. P. S. &. C. R. T. da Silva, "Experimental results on chatter reduction in turning through embedded piezoelectric material and passive shunt circuits," *Mechatronics,* vol. 29, pp. 78-85, 2015.

[81] F. H. M. A. Y. &. L. X. Chen, "Active damping of boring bar vibration with a magnetic actuator," *IEEE/ASME Transactions on MechatronicsIEEE/ASME Transactions on Mechatronics,* vol. 20, no. 6, pp. 2783-2794, 2015.

[82] A. K. A. &. C. D. Pashkevich, "Enhanced stiffness modeling of manipulators with passive joints," *Mechanism and machine theory,* vol. 46, no. 5, pp. 662-679, 2011.

[83] C. C. S. C. M. G. S. &. F. B. Dumas, "A methodology for joint stiffness identification of serial robots," *2010 IEEE/RSJ International Conference on Intelligent Robots and Systems,* pp. 464-469, 2010.

[84] X. Y. W. C. X. &. C. Y. Zhang, "Stiffness identification for serial robot manipulator based on uncertainty approach," in *International Conference on Intelligent Robotics and Applications*, Berlin, Heidelberg, 2011.

[85] K. B. T. I. &. H. G. Kaldestad, "Robotic face milling path correction and vibration reduction," *2015 IEEE International Conference on Advanced Intelligent Mechatronics (AIM),* pp. 543-548, 2015.

[86] T. L. S. H. L. L. Z. L. W. &. J. L. Wang, "Force-based control of a compact spinal milling robot," *International Journal of Medical Robotics and Computer Assisted Surgery,* vol. 6, no. 2, pp. 178-185, 2010.

[87] L. S. S. P. Z. D. D. G. O. &. L. W. Yuan, "Mode coupling chatter suppression for robotic machining using semi-active magnetorheological elastomers absorber," *Mechanical Systems and Signal Processing,* vol. 117, pp. 221-237, 2019.

[88] F. Z. H. &. D. H. Chen, "Eddy Current Damper Design for Vibration Suppression in Robotic Milling Process," in *IEEE International Conference on Robotics and Automation (ICRA)*, 2018.

[89] J. K. Salisbury, "Active stiffness control of a manipulator in cartesian coordinates," *1980 19th IEEE conference on decision and control including the symposium on adaptive processes,* pp. 95-100, 1980.

[90] S. F. &. K. I. Chen, "Conservative congruence transformation for joint and Cartesian stiffness matrices of robotic hands and fingers," *The International Journal of Robotics Research,* vol. 19, no. 9, pp. 835-847, 2000.

[91] E. W. M. &. R. S. Abele, "Modeling and identification of an industrial robot for machining applications," *CIRP annals,* vol. 56, pp. 387-390, 2007.

[92] Y. D. H. &. K. Y. Guo, "Stiffness-oriented posture optimization in robotic machining applications," *Robotics and Computer-Integrated Manufacturing,* vol. 35, pp. 69-76, 2015.

[93] Y. Z. H. &. D. H. Lin, "Posture optimization methodology of 6R industrial robots for machining using performance evaluation indexes," *Robotics and Computer-Integrated Manufacturing,* vol. 48, pp. 59-72, 2017.

[94] S. H. H. K. W. &. A. J. Zargarbashi, " Posture optimization in robot-assisted machining operations," *Mechanism and Machine Theory,* vol. 51, pp. 74-86, 2012.

[95] S. G. V. L. T. P. S. L. R. P. &. P. P. Mejri, "Dynamic characterization of machining robot and stability analysis," *The International Journal of Advanced Manufacturing Technology,* Vols. 82(1-4), pp. 351-359, 2016.

[96] C. C. M. G. A. &. K. J. Y. Bisu, "Dynamic behavior analysis for a six axis industrial machining robot," *Advanced Materials Research,* vol. 423, pp. 65-76, 2012.

[97] M. C. E. &. M. P. Rognant, "A systematic procedure for the elastodynamic modeling and identification of robot manipulators," *IEEE Transactions on robotics,* vol. 26, pp. 1085-1093, 2010.

[98] "Grainger," Grainger, [Online]. Available: https://www.grainger.com/category/pumps/machine-tool-and-parts-washer-pumps/machine-tool-pumps. [Accessed 22 May 2019].

[99] B. J. &. R. M. H. Schwarz, "Experimental modal analysis," *CSI Reliability week,* vol. 35, pp. 1-12, 1999.

[100] R. P. Lindsay, "The effect of contact time on forces, wheelwear rate and G-ratio during internal and external grindingThe effect of contact time on forces, wheelwear rate and G-ratio during internal and external grinding," *CIRP Annals,* pp. 33(1), 193-197, 1984.

[101] "Geometrical product specifications (GPS) — Flatness — Part 1: Vocabulary and parameters of flatness," [Online]. Available: https://www.iso.org/obp/ui/#iso:std:iso:12781:-1:ed-1:v1:en. [Accessed 6 May 2019].

[102] "GD&T Basics," [Online]. Available: https://www.gdandtbasics.com/flatness/. [Accessed 6 May 2019].

[103] "Geometrical product specifications (GPS) — Geometrical tolerancing — Tolerances of form, orientation, location and run-out," [Online]. Available: https://www.iso.org/obp/ui/#iso:std:iso:1101:ed-4:v1:en. [Accessed 6 May 2019].

[104] "GD&T basics-Parallelism," [Online]. Available: https://www.gdandtbasics.com/parallelism/. [Accessed 6 May 2019].

[105] Keyence , [Online]. Available: https://www.keyence.com/ss/products/microscope/roughness/surface/parameters.jsp. [Accessed 6 May 2019].

[106] D. E. Whitney, "The mathematics of coordinated control of prosthetic arms and manipulators," *ASME Journal of Dynamic Systems, Measurement and Control,* vol. 20, pp. 303-309, 1972.

[107] A. D. M. B. R. G. O. &. L. S. Olabi, "Improving the accuracy of industrial robots by offline compensation of joints errors," in *2012 IEEE International Conference on Industrial Technology*, 2012.

[108] R. &. D. J. Hartenberg, "Kinematic synthesis of linkages," McGraw-Hill, New York, 1964.

[109] J. J. Craig, Introduction to robotics: mechanics and control, 3/E, Pearson Education India, 2009.

[110] J. Z. M. B. T. &. A. P. Farsky, "Influence of Grinding Conditions on Surface Quality and Accuracy when a Tool Grinder is Used," *Annals of DAAAM & Proceedings,* pp. 0930-937, 2018.

[111] B. d. L. L. T. A. &. B. L. Denkena, "Prediction of contact conditions and theoretical roughness in manufacturing of complex implants by toric grinding tools," *International Journal of Machine Tools and Manufacture,* vol. 50, no. 7, pp. 630-636, 2010.

[112] B. &. v. d. M. M. Denkena, "Diamond tools for the grinding of complex ceramic implant surfaces," *Advanced Materials Research,* vol. 76, pp. 33-37, 2009.

[113] R. S. &. L. R. P. Hahn, "The influence of process variables on material removal, surface integrity, surface finish and vibration in grinding," *Advances in Machine Tool Design and Research,* pp. 95-117, 1970.

[114] R. P. Lindsay, "The effect of parameter variations in precision grinding," *Journal of Engineering for Industry,* vol. 92, no. 3, pp. 683-693, 1970.

[115] H. K. P. J. I. I. &. P. T. Tönshoff, "Modelling and simulation of grinding processes," *CIRP annals,* vol. 41, no. 2, pp. 677-688, 1992.

[116] M. C. X. Z. a. B. K. X. Ren, "A local process model for simulation of robotic belt grinding," *Int. J. Mach. Tools Manuf,* vol. 47, no. 6, p. 962–970, 2017.

[117] H. B. L. a. Z. H. Y. Y. X. Song, "An adaptive modeling method for a robot belt grinding process," *IEEE/ASME Trans. Mechatronics,* vol. 17, no. 2, pp. 309-317, 2012.

[118] D. C. F. Z. H. &. D. H. Li, "Robotic Compliant Grinding for Complex Blisk with an Intelligent End-Effector," *2018 IEEE International Conference on Mechatronics and Automation,* pp. 1469-1474, 2018.

[119] M. A. T. D. L. X. &. H. Y. M. Minami, "Position control and explicit force control of constrained motions of a manipulator for accurate grinding tasks," *Advanced robotics,* vol. 11, no. 3, pp. 285-300, 1996.

[120] N. H. W. D. &. Z. J. C. Kim, "Numerical analysis and parameter study of a mechanical damper for use in long slender endmills," *International Journal of Machine Tools and Manufacture,* vol. 46, no. 5, pp. 500-507, 2006.

[121] M. F. &. R. O. Zaeh, "Improvement of the Static and Dynamic Behavior of a Milling Robot (Mini Special Issue on Virtual Manufacturing)," *International journal of automation technology,* vol. 9, no. 2, pp. 129-133, 2015.

[122] J. K. Salisbury, "Active stiffness control of a manipulator in cartesian coordinates," *1980 19th IEEE conference on decision and control including the symposium on adaptive processes ,* pp. 95-100, 1980.

[123] E. W. M. &. R. S. Abele, "Modeling and identification of an industrial robot for machining applications," *CIRP annals,* vol. 56, no. 1, pp. 387-390, 2007.

[124] J. L. W. Y. H. &. L. Y. Kim, "Real-time monitoring and control system of an industrial robot with 6 degrees of freedom for grinding and polishing of aspherical mirror," *2018 International Conference on Electronics, Information, and Communication (ICEIC) ,* pp. 1-4, 2018.

[125] "Grainger," Dayton, [Online]. Available: https://www.grainger.com/category/pumps/machine-tool-and-parts-washer-pumps/machine-tool-pumps.. [Accessed 22 May 2019].

[126] M. M. V. G. S. V. P. S. &. C. R. T. da Silva, "Experimental results on chatter reduction in turning through embedded piezoelectric material and passive shunt circuits," *Mechatronics,* vol. 29, pp. 78-85, 2015.